Magnetic Anisotropy in Ultrathin Epitaxial Films Grown on Surfaces Vicinal to Cu(001)

by

Donna Sue Chuang

S.B., Materials Science and Engineering
Massachusetts Institute of Technology (1990)

Submitted to the Department of Materials Science and Engineering
in partial fulfillment of the requirements for the degree of

Doctor of Philosophy

at the

MASSACHUSETTS INSTITUTE OF TECHNOLOGY

September 1994

Author ....
Department of Materials Science and Engineering
August 5, 1994

Certified by ....
Robert C. O'Handley
Senior Research Scientist
Thesis Supervisor

Certified by ....
Lionel C. Kimerling
Thomas Lord Professor of Materials Science and Engineering
Thesis Supervisor

Accepted by ....
Carl V. Thompson II
Professor of Electronic Materials
Chair, Departmental Committee on Graduate Students

Magnetic Anisotropy in Ultrathin Epitaxial Films Grown on Surfaces Vicinal to Cu(001)

by

Donna Sue Chuang

Submitted to the Department of Materials Science and Engineering
on August 5, 1994, in partial fulfillment of the
requirements for the degree of
Doctor of Philosophy

Abstract

The in-plane magnetic anisotropy in ultrathin fcc Co and $Ni_{79}Fe_{21}$ films grown on vicinal Cu(11n) has been examined. Vicinal surfaces are characterized by terraces only a few atoms wide separated by atomic steps. The anisotropy was studied as a function of film thickness (t), terrace-width (d), and temperature. Step-edge magnetocrystalline anisotropy, magnetoelastic anisotropy, and magnetostatic anisotropy in vicinal films were modeled.

Co/Cu(1 1 13) and Co/Cu(117) films exhibit uniaxial in-plane anisotropy, favoring **M** parallel to the steps, for thicknesses up to 20 monolayers (ML). The strength of the anisotropy increases with decreasing film thickness and decreasing terrace-width. The anisotropy weakens as temperature increases from $25°C$, vanishing at $T \approx 130°C$, well below T_C. $Ni_{79}Fe_{21}$/Cu(117) films exhibit uniaxial in-plane anisotropy favoring **M** parallel to the steps for thicknesses up to at least 14 ML. The anisotropy in $Ni_{79}Fe_{21}$/Cu(117) is approximately two orders of magnitude weaker than that in Co/Cu(117).

A pair-interaction model, which includes effects of misfit strain in epitaxial films, predicts a magnetic energy density for vicinal films of the form $E_{film} = E_{bulk} - 2\frac{E_{surface}}{t} - 2\frac{E_{step}}{t\,d}$, indicating that anisotropy and magnetoelastic coupling coefficients for vicinal films depend on thickness and terrace-width. Step-edge magnetocrystalline anisotropy favors **M** parallel to the steps in fcc Co/Cu(11n) and $Ni_{79}Fe_{21}$/Cu(11n), but **M** perpendicular to the steps in bcc Fe/W(01n), in agreement with experimental observations. A discrete dipole calculation of magnetostatic anisotropy in vicinal films indicates that it favors **M** parallel to the steps, but is an order of magnitude smaller than step-edge anisotropy in Co/Cu(11n). Magnetoelastic anisotropy due to possible anisotropic strain in Co/Cu(11n) favors **M** perpendicular to the steps.

Our experimental and theoretical findings indicate that the major source of in-plane anisotropy in ultrathin vicinal films is magnetocrystalline anisotropy due to reduced coordination symmetry around atoms at the step-edges. The orientation of the magnetic easy axis and the strength of the anisotropy depend on both the magnetoelastic coupling coefficients B_1 and B_2 and the crystal structure of the film.

Thesis Supervisor: Robert C. O'Handley
Title: Senior Research Scientist

Thesis Supervisor: Lionel C. Kimerling
Title: Thomas Lord Professor of Materials Science and Engineering

Acknowledgements

I thank my thesis supervisor, Dr. Bob O'Handley, for his wonderful support and advice. I am very proud to be one of his graduate students.

I thank Dr. Craig Ballentine for all of his help in the lab. He has made the long-hours enjoyable, and the ever-present problems more manageable with his empathy and sense of humor.

I thank my co-advisor, Professor Kimerling, and the other members of my thesis committee, Professor Allen, and Professor Ceder for their many helpful comments and suggestions throughout my study.

I would also like to thank Professor Oliveria for his initial participation on my thesis committee, and for his support and encouragement during my term as a T.A. for 3.20.

I have greatly appreciated the friendship and support of the other graduate students in the Thin-Film Magnetism group. Thanks to Gabriel Bochi for being there when I needed a coffee-break, and for his many useful discussions regarding surface anisotropy. Thanks to Oh-Sung Song, for his discussions regarding the pair-interaction model, and for always giving a helping hand at the right time. Thanks to Kin Ha for keeping the office full of lively debates and library books.

Thanks to Dr. Hans Peter Oepen of KFA Julich, Germany for getting me interested in magnetic properties of vicinal films, and for already making my young career an international one.

I would also like to acknowledge support from the Office of Naval Research during the first three years of my graduate studies.

For their constant love and support,
this thesis is dedicated to

my parents
Don and Carolyn McCoy,

my grandmother
Loretta McCoy,

and my husband
Tom Chuang.

Contents

List of Figures

List of Tables

Chapter 1

Introduction

1.1 Motivation

Magnetic materials stand apart from most other classes of materials, such as semiconductors and superconductors, in that they have a vector (the magnetization) as their primary defining parameter. In any application of a magnetic material, we are not only interested in the size, or magnitude, of the vector, but also we need to know the direction in which it points. We must understand what its orientation will be without any external influences (i.e. any applied fields); we must know how easy it is to change the orientation of that vector with an applied field; and finally, we must know what orientation the magnetization vector will take after we remove the applied field. All of these issues are intimately related to the magnetic anisotropy of the material, the dependence of its free energy on the orientation of the magnetization.

Recently, the anisotropy in thin films has received a great deal of attention. The number of applications for magnetic materials in thin-film form, either as single films or more often as multilayered stacks of films, is growing rapidly. The largest growth is found in the area of magnetic information storage, as can be seen by referring to any recent issue of I.E.E.E. Transaction on Magnetics. The development of new magneto-optic recording media, and thin-film reading and writing heads both inductive, and most recently magnetoresistive is being pushed by the desire to obtain 10 GB/in^2 recording density by the turn of the century.

An important difference between materials in bulk and in thin-film form is that properties of thin films are often governed by surface or interface effects. This difference is especially evident in magnetic anisotropy. Néel [1] proposed that a surface can create strong anisotropies due only to its reduced symmetry relative to that in the bulk, and that this anisotropy dominates the film's behavior as the thickness of the film decreases. This phenomenon was demonstrated by Gradmann and co-workers when they observed a vertical easy axis of magnetization in an ultrathin film of $Ni_{48}Fe_{52}$/Cu(111) [2]. The easy axis lies in-plane for thicker films, in which surface effects are no longer significant. The technological importance of surface anisotropy was revealed with the development of vertical recording and magneto-optic data storage media. One of the current challenges in the area of thin-film magnetism is determining how to predict surface and interface anisotropies.

A new manifestation of magnetic surface anisotropy has recently been demonstrated. A few research groups have observed that steps on a substrate's surface influence the magnetic properties of an epitaxial film. Vicinal surfaces, cut at an orientation slightly off a high symmetry plane such as (001) in a cubic crystal, are typically used to obtain well ordered stepped surfaces [3, 4]. However, carefully controlled growth conditions can also create steps on flat surfaces [5]. The loss of the four-fold symmetry due to the presence of the steps manifests itself in the macroscopic magnetic properties of the ultrathin films grown on the surface. However, it is not yet clear through what mechanism the surface morphology affects the magnetism in the films. In the case of Fe/W vicinal (001), the films exhibit two-fold magnetic anisotropy and are most easily magnetized perpendicular to the steps, in the plane of the film [4]. However, for fcc Co/Cu vicinal (001), the easy axis is parallel to the steps [6].

The main objective of this thesis is to determine the mechanism through which the presence of surface steps induces the uniaxial anisotropy observed in vicinal films. Because of the film quality and interface sharpness achievable in the Co/Cu system, changes in anisotropy due to surface effects should be able to be isolated from effects due to other defects and surface roughness present in many films. Therefore, we concentrated on fcc Co/Cu vicinal films; however, our study led to a general model of the step-induced uniaxial anisotropy that is successful in explaining that observed in vicinal fcc $Ni_{79}Fe_{21}$/Cu(001) and bcc Fe/W(001) films, as well.

1.2 Thesis Overview

Our approach to determining the mechanism through which surface steps alter the magnetic anisotropy in thin films was to first hypothesize possible mechanisms, and then develop a research plan to test our hypotheses. Initially we hypothesized that the uniaxial anisotropy in vicinal magnetic films is most likely caused by one or more of the following: 1) broken symmetry at the step edges, 2) the magnetostatic energy of the terraced films, and/or 3) anisotropic strain in the films. The first section of chapter 2 gives a review of magnetic anisotropies that will further clarify these proposed mechanisms; however, a brief description of each is given below.

When a surface of a film is created, it leaves dangling bonds; similarly, a step in a film's surface also leaves dangling bonds. The atoms at the surface and the step are missing neighboring atoms; they are in sites of lower symmetry than the atoms in the bulk of the material. This reduction in symmetry leads to magnetic anisotropies not found in bulk materials. If this is the dominant mechanism through which the surface steps induce the uniaxial anisotropy, we expect the anisotropy to strengthen as the film thickness decreases, and/or as the terrace width decreases. When either change occurs, a larger fraction of the overall film volume is occupied by atoms at the step-edge and their effects are more significant. The experimental results concerning the thickness and terrace width dependence of the anisotropy are presented in Sec. 4.1. We have also modeled the magnetic effects of this broken symmetry using a pair-interaction model (Néel's model), as described in Chapter 5.

Magnetostatic considerations dictate that a material is easiest to magnetize in the direction that creates the fewest surface poles. In terms of vicinal films, this consideration implies that having the magnetization oriented parallel to the steps is a lower energy configuration than having **M** perpendicular to the steps. **M** perpendicular to the steps would create surface poles at the step edges. Such an explanation for the uniaxial anisotropy in vicinal films is consistent with the observed easy axis in the Co/Cu system; however, it is inconsistent with the Fe/W vicinal system which prefers **M** to be perpendicular to the steps. To further confirm that the anisotropy was not induced magnetostatically, we studied the temperature dependence of the anisotropy in Co/Cu vicinal to (001), Sec. 4.1, to see if it followed the behavior expected for a magnetostatic anisotropy, which is discussed in Sec.

2.1.

In semiconductor films grown on vicinal surfaces, the presence of the surface steps can help relieve some of the misfit strain in epitaxial films [7]. Although we are unable to experimentally determine if the Co/Cu vicinal to (001) films show similar behavior, we still consider what effect this strain relief would have on the films' magnetic anisotropy. If the presence of the steps causes an anisotropic strain in the film, a resulting magnetic anisotropy will be induced via magnetoelastic coupling. A model of such a magnetoelastic anisotropy in Co/Cu(11n) is given at the end of Sec. 4.1. We also studied the anisotropy in vicinal $Ni_{79}Fe_{21}$/Cu(117) films in order to test the importance of this magnetoelastic effect. The magnetoelastic coupling coefficients of $Ni_{79}Fe_{21}$ are nearly zero; thus we expect that any magnetoelastic anisotropy will be insignificant. The results of this part of the study are presented in Sec 4.2.

The presentation of this research is organized as follows. The necessary background material regarding magnetic anisotropy, the materials systems studied, and vicinal surfaces is presented in chapter 2. Chapter 3 describes the equipment and experimental techniques used in the study. Chapter 4 presents the experimental results and discusses the implications regarding the mechanism through which the presence of the steps induces a uniaxial magnetic anisotropy in the films. Chapter 5 presents a theoretical model which we have developed and successfully used to interpret the anisotropy in vicinal films. In chapter 6 we discuss the results of our study and how they relate to other work in the field of thin film magnetism. We offer suggestions for future work in chapter 7, and list the main conclusions of this thesis in chapter 8.

Chapter 2

Review

In the previous chapter, we presented the motivation for this study, and outlined our plan for discovering the mechanism through which surface steps induce uniaxial magnetic anisotropy in vicinal films. To insure that the reader has the necessary background to appreciate the conclusions of the research and how it relates to previously published work, in this chapter we review relevant topics. The first section reviews the sources of magnetic anisotropy, with special attention in Sec. 2.2 given to anisotropy in thin films and at surfaces. Section 2.3 gives an overview of the growth, structural, and magnetic characteristics of Co/Cu(001), as found in the literature. Similarly, in Sec. 2.4 the properties of $Ni_{79}Fe_{21}$/Cu(001) are reviewed. Section 2.5 describes the morphology of vicinal surfaces, and reviews the previously published evidence of magnetic behavior in vicinal films.

2.1 Magnetic Anisotropy

A material possesses magnetic anisotropy, if its free energy depends upon the direction of the local magnetization (**M**). The overall anisotropy has contributions from intrinsic materials properties, the shape of the material, and the state of strain in the material. The easy axis denotes the direction of magnetization which minimizes the magnetic energy in the material. The hard axis is the direction of magnetization for which the magnetic energy is a maximum. The anisotropy energy is actually an energy difference: the difference in energy that it takes to saturate a material along the hard axis, as opposed to along the easy axis.

Magnetostatic Anisotropy

Magnetostatic anisotropy is also referred to as shape anisotropy, and arises from the dipole interaction between magnetic poles at surfaces. Considering only the magnetostatic energy, a material will prefer to be magnetized in whatever way creates the fewest poles; a non-spherical piece of material will be easier to magnetize along a long axis than along a short one. For a thin film, magnetostatic energy favors magnetization in the plane of the film as opposed to **M** perpendicular to the film.

The form of magnetostatic energy is expressed in S.I. units as

$$E_{Magnetostatic} = \frac{\mu_0}{2} N \left[\frac{M(T)}{M(0)}\right]^2 \tag{2.1}$$

where N is a demagnetization factor which is calculated from the overall shape of the material. For a film magnetized parallel or perpendicular to the surface, the demagnetization factor is 0 or 1, respectively. The temperature dependence of this energy will be governed by the temperature dependence of **M**; magnetostatic energy varies with temperature as $[\mathrm{M(T)/M(0)}]^2$. The temperature dependence of the magnetization **M**(T) is shown in Fig. 2-1.

Magnetocrystalline Anisotropy

The free energy of a single crystal depends on the orientation of **M** with respect to the crystallographic axes because of magnetocrystalline anisotropy. This anisotropy is intrinsic to the material, and reflects the symmetry of a material's crystal structure. The physical origin of crystalline anisotropy is spin-orbit coupling, the interaction that tends to align the magnetic moment due to the spin of an atom's electrons with the magnetic moment due to the orbitals of the electrons. [8, 9]

The magnetocrystalline energy can be described in a series expansion of direction cosines of $\mathbf{M_s}$ relative to the crystal axes **x**=[100], **y**=[010], and **z**=[001] [10]. For cubic systems the expression for this energy is as follows.

$$E_{Magnetocrystalline} = K_0 + K_1(\alpha_1^2\alpha_2^2 + \alpha_1^2\alpha_3^2 + \alpha_2^2\alpha_3^2) + K_2\alpha_1^2\alpha_2^2\alpha_3^2 + ... \tag{2.2}$$

The K's in the above equation are crystalline anisotropy constants. They can be either positive or negative depending on the orientation of the easy axis. Often the form of this energy is approximated by the K_1 term. If K_1 is positive, the easy axes are the $< 100 >$ directions (e.g. fcc Fe). If K_1 is negative, the $< 111 >$ axes are easy directions as observed for Ni, and thick films of fcc Co. [11]

These magnetocrystalline constants vary with temperature. Above the Curie temperature, when long-range ferromagnetic order disappears, the anisotropy vanishes, and the constants go to zero. The anisotropy typically decreases more rapidly than magnetic ordering upon an increase in temperature. It has been demonstrated, both experimentally and theoretically, that the temperature behavior of K depends on the magnetic symmetry of the system [12, 13, 14, 15, 16, 10]. When the anisotropy is represented in spherical harmonics, $Y_l^m(\theta, \phi)$, the symmetry may be denoted by the lowest value of l needed to describe the phenomenon. Uniaxial symmetry requires that the expansion begin with terms having an l value of 2, while cubic symmetry requires an $l \geq 4$. The behavior of K_i with temperature is given by

$$\frac{K_i(T)}{K_i(0)} = \left[\frac{M(T)}{M(0)}\right]^{\frac{l(l+1)}{2}} \tag{2.3}$$

The temperature dependence of K_1 (cubic anisotropy, $l = 4$), and K_u (uniaxial anisotropy, $l = 2$) is plotted in Fig. 2-1. This treatment is most applicable to oxides and rare-earth based magnetic materials, in which the magnetic moment is well localized [12]. However, it is also successful in representing the anisotropy behavior in some transition metals and alloys: the anisotropy of symmetries requiring lower l values is expected to fall off more slowly as temperature increases than those of higher l values. Keffer [15] showed that Eq. 2.3 is most applicable to transition metals at low temperatures relative to their Curie temperature; at higher temperatures there is a gentler temperature dependence of magnetic anisotropy, as predicted by Van Vleck [14].

Magnetoelastic Anisotropy

Magnetoelastic anisotropy is due to the connection between strain and magnetic behavior. Its origin can also be traced to the spin-orbit interaction. Strain in a material can alter the local symmetry around atoms, thus altering their magnetic behavior. Magnetoelastic

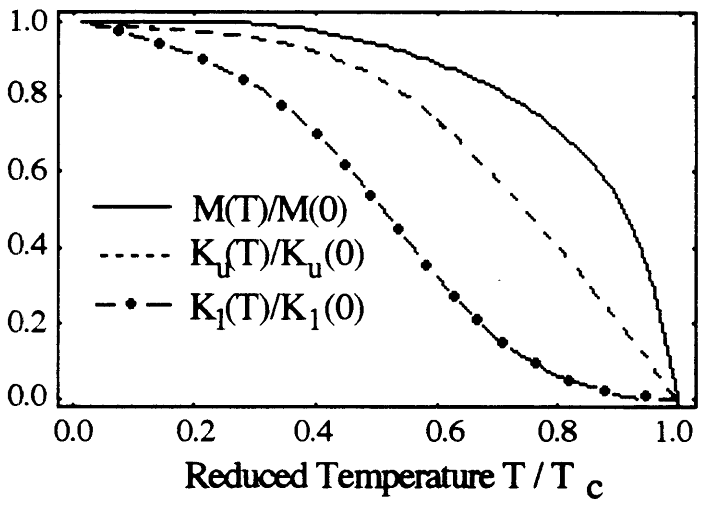

Figure 2-1: Temperature dependence of cubic (K_1) and uniaxial (K_u) anisotropies as given by Eq. 2.4.

anisotropy energy for a cubic material is given by the following expression:

$$E_{Magnetoelastic} = B_1(e_{11}\alpha_1^2+e_{22}\alpha_2^2+e_{33}\alpha_3^2)+2B_2(e_{12}\alpha_1\alpha_2 + e_{23}\alpha_2\alpha_3 + e_{31}\alpha_3\alpha_1) + \ldots \quad (2.4)$$

The B's in Equation 2.4 are the magnetoelastic coupling coefficients, and the e's are components of the strain tensor. In this representation, the shear strains, e_{ij}, are tensor shear strains, as opposed to engineering shear strains. Note that a uniaxial strain in a cubic crystal induces a uniaxial magnetoelastic anisotropy.

Measuring the Anisotropy

We can measure the magnetic anisotropy energy of a material by applying an external field along various directions and observing the rotation of **M** into the direction of the field. This response is typically monitored through the measurement of a hysteresis, or M(H) loop. The hysteresis loops obtained in this study are plots of the component of **M** parallel to the applied field **H** as a function of H.

An externally applied magnetic field will influence the direction of the magnetization in a material by exerting a torque on the magnetization vector. The corresponding energy, termed the Zeeman energy, is

$$E_{Zeeman} = -\mu_o \mathbf{H} \cdot \mathbf{M} \quad (2.5)$$

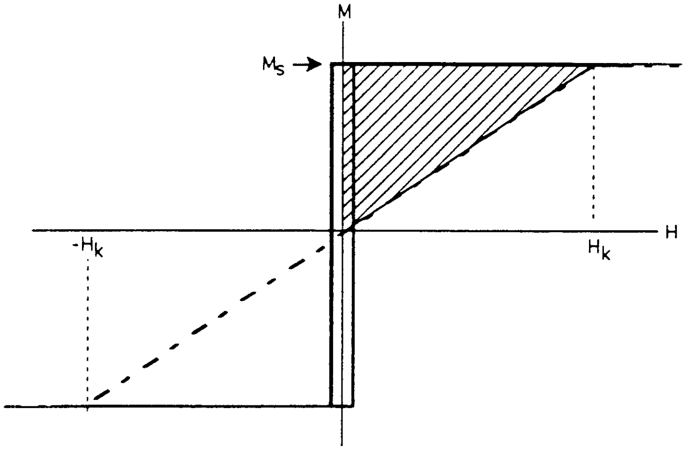

Figure 2-2: Anisotropy energy represented as the area between the hard axis M(H) loop (dashed line) and the easy axis loop (solid line).

which is a minimum if **M** is parallel to **H**. When a strong magnetic field is applied along a direction other than the easy axes, the local magnetization vector will rotate towards, or switch through domain wall motion to a direction aligned with the applied field, lowering the Zeeman energy at the expense of increased magnetic anisotropy energy.

The anisotropy energy is the difference between the energy needed to saturate a material in its hardest direction and the energy needed to saturate in its easiest direction. If the M(H) loop taken for **H** applied along the hard axis has the shape given by the dashed line in Fig. 2-2, and the easy axis loop is given by the solid line, then the shaded region between the two loops represents the anisotropy energy. For a linear response along the hard axis ($H < H_k$), this energy is given by $H_k M_s/2$.

Several magnetic parameters besides anisotropies can also be obtained from hysteresis loops, as indicated on the sample loop in Figure 2-3. The line marked *initial response* is the M-H behavior for an initially demagnetized sample; and the remainder of the curve is the loop obtained after continually sweeping the field so that the film becomes fully saturated in both the positive and negative direction. The height of the curve is governed by the saturation magnetization M_s, and the slope at any point of the curve is the susceptibility, χ. The half-width of the loop at M=0 is the coercive field, H_c, which is a measure of the energy needed to overcome barriers to domain wall motion.

If **M** remains uniform and in the plane of the film, the Stoner-Wohlfarth (SW) model [17] predicts the film's M(H) behavior. This model involves minimizing the magnetic energy

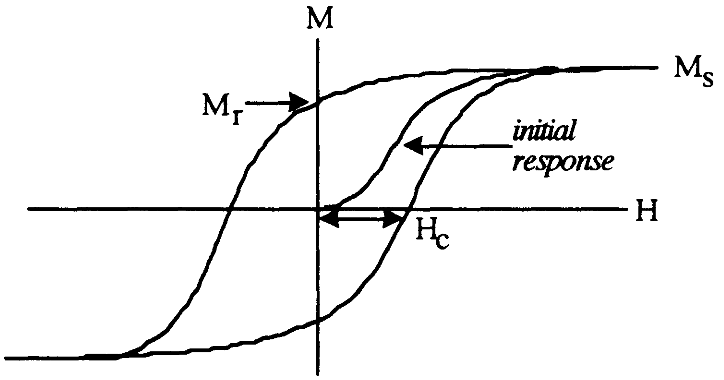

Figure 2-3: A sample magnetic hysteresis loop.

of the film as given by the sum of the anisotropies and the Zeeman energy described above. The SW model neglects domain wall effects and assumes coherent magnetization reversal. We will use this model when we interpret the temperature dependence of the anisotropy in Co/Cu vicinal to (001) films in Chapter 4.

2.2 Anisotropy in Thin Films

When considering thin films, as opposed to bulk materials, there are a few more contributions to magnetic anisotropy that must be considered. These are typically referred to as magnetic surface anisotropies (MSA), and they arise because a significant fraction of a thin film is at either the surface (film/vacuum interface) or the film/substrate interface. Atoms at either of these interfaces are in very different local environments than atoms in the bulk, and thus give rise to additional anisotropies. Other phenomena become important because of the small dimensions in thin films, and the interactions between the film and the substrate.

Many research groups have shown that MSA, including strain effects [18, 19, 20, 21] and effects of substrate morphology [3, 4, 5, 22] is a significant factor governing the anisotropy in films and multilayers. In some systems, the MSA is strong enough to overcome the magnetostatic energy (Sec. 2.1) of the film and produce a perpendicular easy axis (e.g. Ni/Cu [19], Fe/Ag [23, 24, 25], Fe/Cu [26, 27, 28, 29]). Interpretations of surface anisotropy have focussed largely on phenomenological descriptions using the Néel surface anisotropy model [1], and there have been a few first-principle calculations (e.g. Ref. [30]). A difficulty encountered in calculating magnetic anisotropies from first principles is that the spin-orbit interaction is quite small compared to other electronic energies. Recently, however, Victora and MacLaren have brought these two approaches together, demonstrating that the Néel model agrees well with electronic structure calculation results for Co/Pd multilayers [18]. Special anisotropy considerations in thin films are introduced below, in the context of the bulk anisotropies described in the previous section.

Magnetostatic Considerations in Thin Films

At very small thicknesses, the magnetostatic energy of a film can no longer be calculated using a continuum approach, as is used in obtaining Eq. 2.1. As shown by Draaisma and de Jonge [31], for ultrathin films the demagnetization energy found when treating a magnetic film as a collection of discrete dipoles can differ from that calculated based on a continuum approach. Also, as shown by Bruno [32], depending on the degree of surface and interface roughness, magnetostatic anisotropy for an ultrathin film may even favor magnetization perpendicular to the film. In this thesis, in the fcc Co/Cu(11n) films for which we measure anisotropies ($t > 12$ Å), the film thicknesses are beyond the range in which surface magnetostatic effects are significant, as shown in Fig. 3 of Ref. [31]. However, for completeness, we have calculated the magnetostatic energy of both fcc Co/Cu and Fe/W vicinal to (001) films (Sec. 4.1.5).

Magnetocrystalline Considerations at Surfaces

In ultrathin films, a significant fraction of the film is occupied by atoms at the surface, or at the film/substrate interface. The most obvious difference between atoms at a surface and atoms in the bulk is that the surface atoms have no neighboring atoms on one side. Relative to the bulk, they are in a state of lower coordination, symmetry and different electronic charge distribution. This reduction in symmetry manifests itself in magnetic surface anisotropy. Atoms at the the film/substrate interface will similarly experience a changed environment, resulting in interface anisotropy. This type of anisotropy is modeled and discussed in detail in chapter 5.

Magnetoelastic Considerations in Thin Films

Strain is likely to be present in thin films for a variety of reasons, and we must consider the corresponding magnetoelastic anisotropies. Many of the strains in thin films are due to interactions with the substrate. For example, a difference in thermal expansion coefficients between the film and the substrate will cause strain if the film is deposited at one temperature and then heated or cooled. Other strains are caused by deposition conditions; such as the strain around defects induced during deposition. Still another source of strain which becomes important in thin films is surface relaxation. Atoms at the surface move inwards toward the bulk to adjust to the electronic charge distribution at a free surface [33, 34]. If the net strain in a film is anisotropic, magnetoelastic coupling produces a corresponding magnetic anisotropy.

In epitaxial films, an important cause of strain is the difference, or mismatch, in the lattice constants of the film and substrate. The lattice mismatch is defined as $\eta = (a_{substrate} - a_{film})/a_{substrate}$, which for cobalt on copper is 1.9%. Lattice mismatch may be accommodated by a biaxial strain in the film, or by nucleation of misfit dislocations [35]. There is a critical thickness above which nucleation of dislocations to relieve the strain in the volume of the film becomes energetically favorable. This thickness depends on the size of the misfit, elastic constants of the materials, and the Burgers vector of the dislocations. For the Cu and Co system, the critical thickness is expected to be around 12 Å, but has not been experimentally measured [36]. For films thinner than the critical thickness, the misfit strain is isotropic in the film plane and does not alter the in-plane anisotropy. Magnetoelastic energy can dominate over the magnetostatic energy in some thin-film systems and produce an easy axis perpendicular to the film (e.g. Ni/Cu, [37]).

The present treatments of magnetoelastic effects in thin films typically rely upon bulk values of magnetoelastic coupling coefficients. There have been several experimental studies which indicate that the magnetoelastic coefficients at surfaces can be very different from bulk coefficients [37, 38, 39, 40]. Such a difference is also predicted using the pair-interaction model presented in chapter 5, and is discussed in Sec. 5.5. Measurements of surface magnetoelastic coupling coefficients in thin films along with a proper treatment of magnetoelasticity for such systems is required in order to fully understand the origin of surface and thin film anisotropies.

2.3 fcc Co/Cu(001): Growth and Magnetic Properties

Our study involves a derivative of the Co/Cu(001) system. Co/Cu(001) serves as a useful reference because it has been extensively studied and is well characterized with respect to both its growth characteristics and its magnetic behavior. The recent interest in properties of ultrathin Co films arose from the search for materials to be used in magneto-optic data storage applications. Co/Pt and Co/Pd superlattices are attractive systems for a new generation of magnetic recording media due to their easy axis perpendicular to the film, enhanced Kerr rotation at short wavelengths, and corrosion resistance [41, 42, 43]. In an effort to study the magnetic effect in these superlattice structures, some research groups shifted their focus to simpler materials systems such as Co/Cu in which they could eliminate the complexity of induced interfacial moments in the Pd and Pt [44, 45].

Film Growth

The Co/Cu(001) system exhibits epitaxial, layer-by-layer growth, stabilizing the Co in the fcc structure. This growth mode has been confirmed by Auger electron spectroscopy (AES) [46], medium energy electron diffraction (MEED) [45], low energy electron diffraction (LEED) [47], ultra-violet photoelectron spectroscopy (UPS) [48], and TEAS [45]. There is some recent evidence that the first two layers may deviate from the layer-by-layer growth mode, with islands of the second layer forming before the first layer is complete [49, 50, 51]. Co/Cu(001) films show p(1x1) symmetry; there is no surface reconstruction [45]. The films also grow with a high degree of structural perfection, and yield a sharp interface [47, 46, 52, 53]. There is no significant interdiffusion between the Co and Cu for temperatures below 460 K[54], as expected given that Co and Cu are immiscible at these temperatures (Fig. 2-4 [55]). Because of the perfection with which Co/Cu(001) films can be made, they are very suitable for studying magnetic surface effects without the complication of interdiffusion and interfacial defects.

There is a 1.9% mismatch between the fcc Co and Cu which puts the Co film in a state of biaxial tension. Studies of Co/Cu(001) films thicker than 4 ML indicate that the epitaxial films have a constant homogeneous strain [56]. Despite the accumulation of strain energy in the growing overlayer, fcc Co films of more than 15 ML have been made which exhibit reasonable quality as judged by LEED [46]. The critical thickness for Co/Cu at

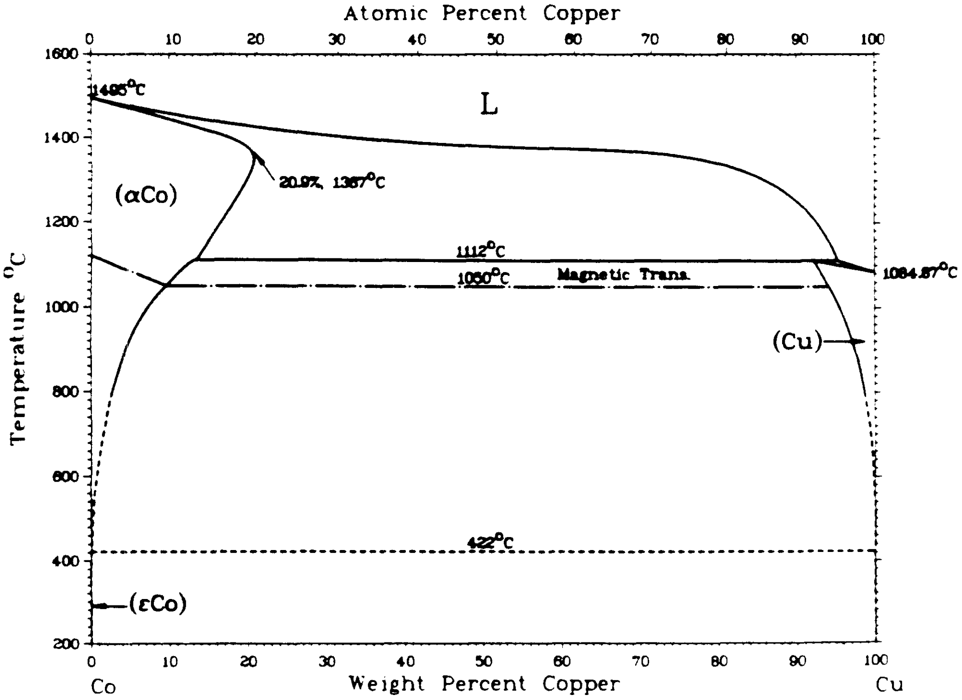

Figure 2-4: Binary phase diagram for Co and Cu.

which misfit dislocations develop to relieve the strain has not been measured experimentally. Accompanying the isotropic extension of the Co in the film plane is a contraction along the surface normal from 1.78 Å to 1.74 Å[54], resulting in a tetragonal distortion of the ultrathin films.

Magnetic Properties

The magnetic properties of Co/Cu(001) are also well characterized in the literature. For thicknesses around 3 ML, the Curie temperature is 600 K, well above room temperature [54], and the room-temperature coercivity is very low (5 Oe).

The magnetic anisotropy of Co/Cu(001) appears to be primarily governed by the magnetostatic energy of a thin film, and the magnetocrystalline energy of fcc Co. For films 3 ML and thicker, the magnetostatic energy creates a strong anisotropy favoring magnetization in the plane of the film. This in-plane magnetization has been shown for Co/Cu(001) films up to 20 ML of coverage using spin resolved photoemission and MOKE [57]. There is also a 4-fold in-plane anisotropy with $< 110 >$ easy directions of magnetization, as predicted by Equation 2.1 for a negative K_1.

The magnetic domain structure in Co/Cu(001) films 3 - 19 ML thick has been studied using spin-polarized secondary electron microscopy (SEMPA) [3]. The domains in the film are several hundred microns in size. In the "as grown state" the films are single domain except for small closure domains at the edges. The large domain size found in these films greatly increases the probability that the laser beam used for MOKE is probing single domain patches. The domain walls do not necessarily coincide with easy directions of magnetization, giving the film a random domain pattern which does not reflect the magnetic symmetry of the film.

2.4 $Ni_{80}Fe_{20}$/Cu(001): Growth and Magnetic Properties

Our reference system for the vicinal Ni-Fe films investigated in this thesis is $Ni_{80}Fe_{20}$/Cu(001). Ni-Fe alloys around this 80-20 composition are widely used because of their excellent soft magnetic properties. They have extremely small magnetocrystalline anisotropies and magnetoelastic coupling coefficients, as indicated in Fig. 2-5 [58]. For a general review of applications and properties of these materials, see Ref. [58] and references therein. Thin

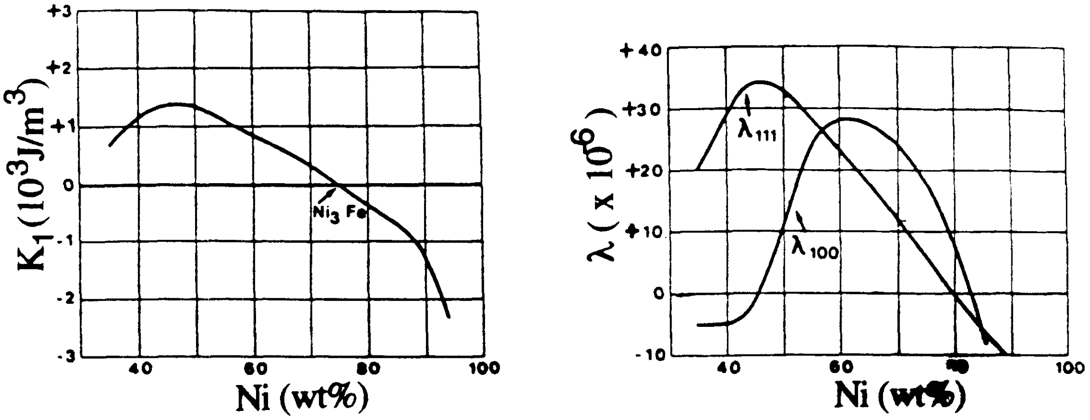

Figure 2-5: Anisotropy constant and magnetostriction constants for Ni-Fe alloys. The magnetoelastic coupling coefficient B_1 is proportional to λ_{100}, and B_2 is proportional to λ_{111}.

films of $Ni_{80}Fe_{20}$ are typically used in polycrystalline form, thus there is not as much information in the literature regarding the growth and properties of single-crystal, epitaxial $Ni_{80}Fe_{20}$/Cu(001) as can be found for Co/Cu(001). However, a recent application of Ni-Fe alloys in a new type of magnetic recording head has spurred some investigations of $Ni_{80}Fe_{20}$/Cu(001). $Ni_{80}Fe_{20}$/Cu heterostructures are being developed for use in magnetoresistive (MR) devices. The performance of these devices depends sensitively on the structure of the Ni-Fe/Cu interface. It was recently demonstrated by Hashim and Atwater that epitaxial $Ni_{80}Fe_{20}$/Cu(001) yields atomically abrupt interfaces, while the interfaces in polycrystalline $Ni_{80}Fe_{20}$/Cu(001) are quite rough [59].

Growth

Epitaxial growth of fcc $Ni_{80}Fe_{20}$ on Cu has been demonstrated at room temperature by ion-beam sputtering [59], evaporation [60], and molecular-beam epitaxy (MBE) [61]. The interface in the sputtered films were atomically abrupt, as demonstrated by cross-sectional TEM. The lattice mismatch betwee Cu and $Ni_{80}Fe_{20}$ is 3%, and the growth is pseudomorphic up to the critical thickness of 2.3 nm [59].

Magnetic Properties

The magnetic properties of $Ni_{80}Fe_{20}$/Cu(001) have been studied by MOKE [59], ferromagnetic resonance (FMR) and an M-H loop tracer [61], and vibrating sample magnetometry

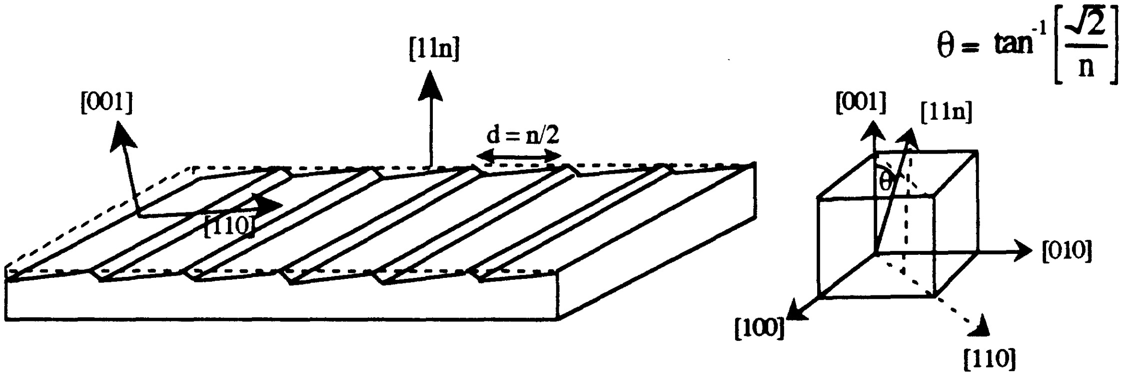

Figure 2-6: An ideal Cu(11n) surface.

(VSM) [60]. The epitaxial films show rather large coercivities ($H_c \approx 35$ Oe) for films thinner than 30 Å[59]. For larger thicknesses, the coercivity decreases monotonically to a few Oersteds. The easy axes are the in-plane $< 110 >$ directions.

2.5 Vicinal Surfaces: Structure and Magnetic Effects

Vicinal surfaces are important in a number of diverse areas: catalysis, crystal growth, crack propagation, tribology [62]; but studies have only recently begun to uncover their influence on magnetism [3, 6, 4, 22]. A vicinal surface is a single crystal surface oriented a small angle away from a low index plane, in a well defined direction. For example, the (11n) surfaces used in this study are vicinal to the (001) low-index surface. The (11n) surface's normal, the [11n] direction, is a small angle away form the [001] direction, rotated toward the [110] direction, as shown in Figure 2-6. The angle between the [11n] and [001] directions is given by $\tan^{-1}(\sqrt{2}/n)$.

Structure

Vicinal surfaces have characteristic surface morphologies. They typically facet into terraces of the low-index plane which are separated by atomic steps. The ideal morphology of a (11n) surface is shown in Figure 2-6. The (001) terraces are an average of n/2 atoms wide, and the atomic steps run parallel to the $[1\bar{1}0]$ direction. The presence of these steps reduces the overall symmetry of the surface from the four-fold symmetry of an (001) plane.

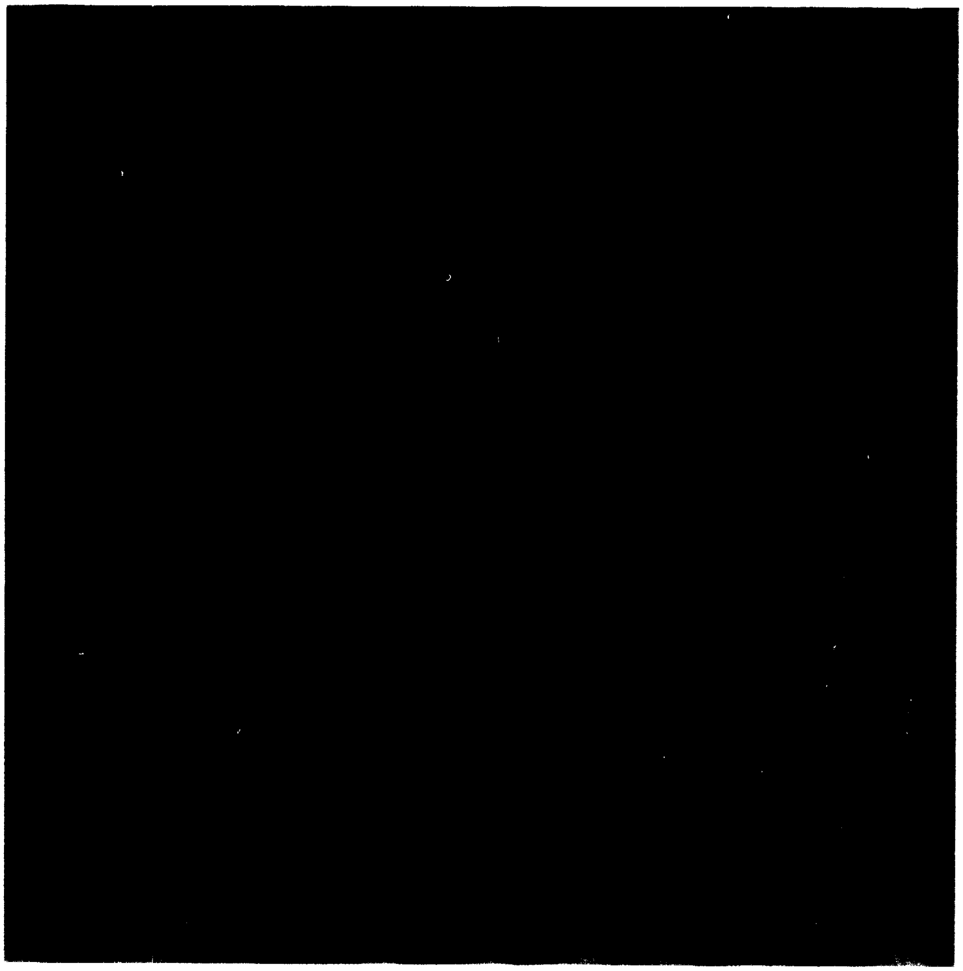

Figure 2-7: STM image of the Cu(1 1 13) surface

Vicinal Cu surfaces from the same source as those used in this study have also been extensively studied via scanning tunneling microscopy (STM) by Frohn and co-workers [63, 64, 65]. These crystals were cut using an electric discharge machine (EDM), and were polished to the desired (11n) orientation to within 0.2°. The surface roughness is less than 60 Å[63]. Two of the STM images of these surfaces are shown in Fig. 2-7 and Fig. 2-8. Fig. 2-7 is an image of the Cu(1 1 13) surface [66]. The mean width of the terraces is the expected 6.5 atoms. However, as can be seen in the figure, there is a distribution of step widths. This average step width was also confirmed in Cu(1 1 13) using LEED [3].

Figure 2-8a is an STM image of the Cu(117) surface. Frohn and co-workers also ob-

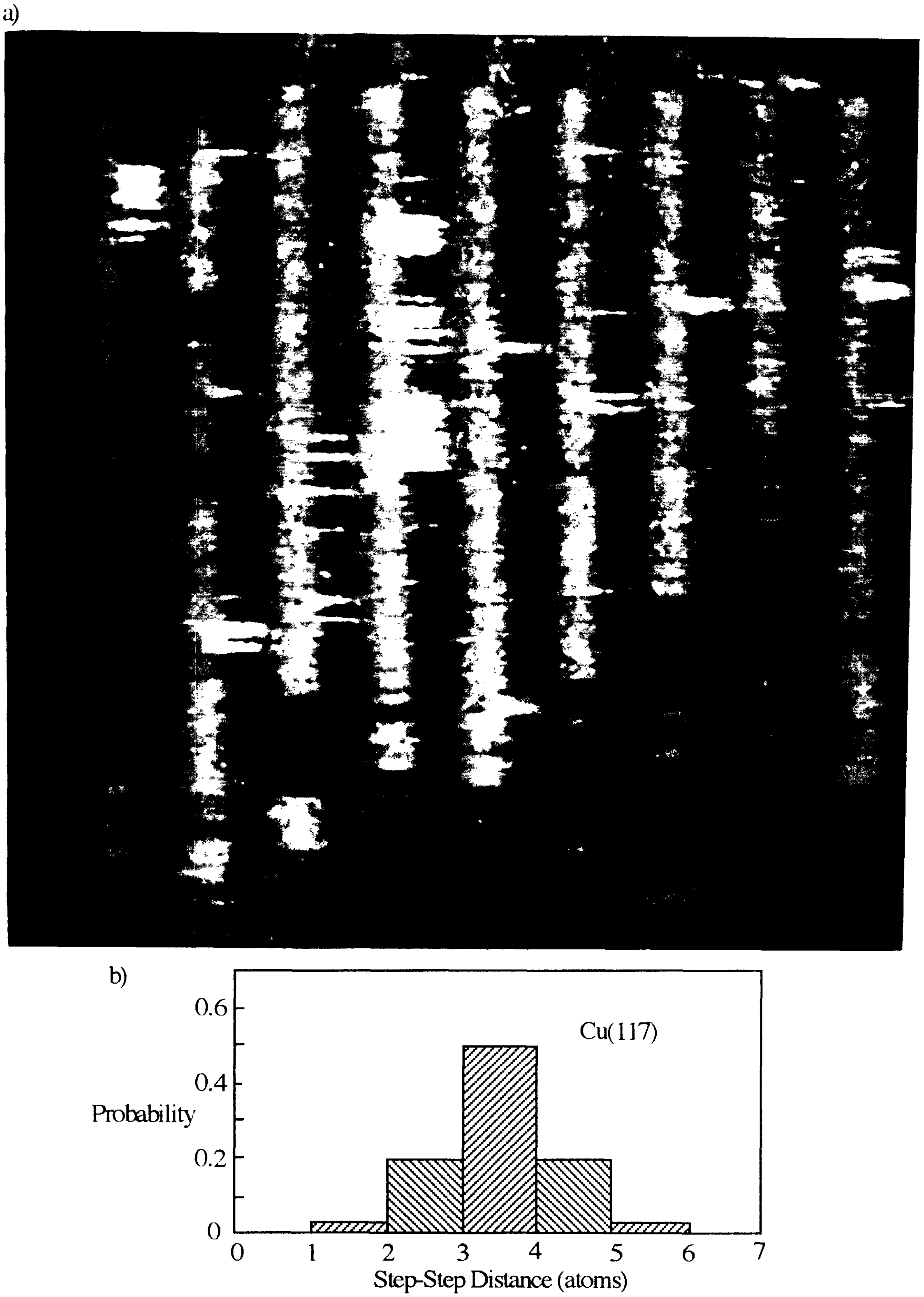

Figure 2-8: a) STM image of the Cu(1 1 7) surface, b) step-step distance distribution on the Cu(117) surface

served the expected mean terrace width of 3.5 atoms in this surface [63]. The terrace width distribution is quite narrow, as indicated in Fig. 2-8b. In a vicinal surface there is an repulsive step-step interaction at small separations which keeps the terrace width uniform in the Cu(117) surface. The step-step interaction becomes attractive for intermediate separations; thus in the Cu(1 1 13) surface which has wider terraces, the distribution broadens [63].

As temperature is varied, vicinal metal surfaces go through a transition between an ordered phase with straight surface steps and a disordered phase in which the steps meander. The temperature of this order-disorder transition is referred to as the roughening temperature, T_R, and occurs well below the bulk melting point [67]. For Cu(11n) surfaces, as n increases, and the step-step distance becomes larger, T_R decreases. For Cu(113), Cu(115), and Cu(117) the roughening temperatures are 620 K, 380 K, and 315 K, respectively [68, 69, 67]. The roughening temperature also scales with the melting temperature of a material. Melting temperatures for Co and Cu are 1455°C and 1083°C, respectively; therefore, it is expected that the T_R for Co/Cu vicinal films will be higher than T_R for bare Cu.

Magnetic Effects

The reduced morphological symmetry in vicinal surfaces manifests itself in the magnetic properties of films grown on such surfaces. Previous to this thesis, these magnetic effects had been observed in two materials systems: fcc Co/Cu(1 1 13) films 3 ML thick [3], and bcc Fe/W vicinal to (001) films between 1 ML and 2.5 ML thick [4]. Since we have begun this investigation [6], our collaborators Oepen and co-workers have also investigated Co/Cu(1 1 17), and Krams *et al.* have examined Cu/Co/Cu(1 1 13). The following sections review the published information on these systems.

fcc Co/Cu(11n)

The growth of Co films on Cu(11n) is very similar to that on Cu(001), being both epitaxial and layer-by-layer [3]. However, their magnetic properties reflect the reduction in surface symmetry due to the presence of the steps. The Co/Cu(11n) film still shows no observable out-of-plane magnetization, but in-plane it exhibits uniaxial anisotropy with the easy direction of magnetization parallel to the steps. Scanning electron microscopy with polarization analysis (SEMPA) studies show that the magnetic domain structures in Co/Cu(1 1 13) films are similar to those for Co/Cu(001) in that they are irregular in shape [3]. The symmetry of the domain structures is not determined by the anisotropy of the film. The domains are approximately 100 μm wide. We discuss the magnetic properties of Co/Cu(1 1 13) further in chapter 5.

Krams *et al.* have recently investigated the anisotropy of Cu/Co/Cu(1 1 13) films between 4 and 14 ML thick [70]. Their Co films are capped by 20 ML of Cu to allow for *ex-situ* room-temperature Brillouin Light Scattering (BLS) experiments, through which they determine the films' magnetic anisotropy. They also find uniaxial anisotropy, with an easy axis parallel to the steps in the Co/Cu(1 1 13) films. The bulk and surface contributions to the uniaxial anisotropy are observed to be of opposite sign, with the bulk favoring alignment of easy axis parallel to the steps, and the surface favoring alignment perpendicular to the steps. Because their films are capped, the surface contribution cited by Krams *et al.* is actually a Co/Cu interface anisotropy. We show in chapters 4 and 5 that our study indicates the Co/vacuum surface contribution favors magnetization parallel to the steps. Krams *et al.* conclude that the origin of the bulk uniaxial anisotropy is magnetoelastic (Eq. 2.4) by defining the strain as a biaxial misfit in the (1 1 13) plane and taking **M** to be in the (1 1 13) plane. They do not attempt to determine the origin of the interfacial contribution to the uniaxial magnetic anisotropy.

Oepen and co-workers have investigated the temperature dependence of the anisotropy in a 2 ML film of Co/Cu(1 1 17) [71]. This surface has (001) terraces 8.5 atoms wide. The anisotropy in the as-grown films, at room temperature, is uniaxial with an easy axis parallel to the steps. At 100°C, the anisotropy becomes nearly biaxial. Upon a further increase in temperature the films again exhibit uniaxial anisotropy favoring magnetization parallel to the steps. Oepen and co-workers attribute these transitions in anisotropy to thermal roughening of the surface and interface steps. The steps at the surface, being easier to disorder, presumably roughen and cause the first transition from uniaxial to biaxial behavior. They propose that at higher temperatures the interface steps roughen as well, returning the films to a uniaxial anisotropy state. Thermal roughening of the steps would similarly explain our observations regarding the temperature dependence of the uniaxial anisotropy in Co/Cu(1 1 13) (Sec. 4.1) [6].

bcc Fe/W(01n)

The magnetic properties of p(1x1) bcc Fe/W vicinal to (001) have been investigated by Chen and Erskine [4]. The W surface on which they deposited Fe was also vicinal to (001); however, instead of having Miller indices (11n), this vicinal surface is an (01n) surface. The normal to an (01n) surface is a small angle from [001] rotated toward the [010] direction. The surface studied by Chen and Erskine was 4° from the (001), or approximately an (0 1 14) surface. The (001) terraces in their films are 25 Åwide, as judged by LEED, and the atomic surface steps are parallel to the [100] direction.

The surface steps in the (01n) vicinal film also induced a uniaxial magnetic anisotropy in the Fe. For thicknesses between 1 and 2.5 ML, the Fe/W films exhibited an in-plane easy axis *perpendicular* to the steps. We further examine the anisotropy in this system in chapter 5.

Chapter 3

Experimental Techniques

In chapter 2, the background material for this study was reviewed. In this chapter, we describe our experimental equipment and techniques. Section 3.1 gives the process for preparation of the substrate and subsequent deposition of the magnetic film. Auger electron spectroscopy, which is used to monitor film and substrate cleanliness, as well as film thickness is reviewed in Sec. 3.2. The magneto-optical technique used for magnetic characterization is described in Section 3.3.

3.1 Sample Preparation and Film Deposition

When studying ultrathin films, the film must be kept free of contaminants during all stages of the experiment. In order to obtain such cleanliness, the growth and characterization of the cobalt and permalloy films were performed in UHV. The vacuum chamber is shown schematically in Figure 3-1. The chamber is equipped with a mechanical roughing pump, and a turbo-pump which provide a base pressure of 1 x 10^{-10} torr.

The sample holder is mounted on a manipulator capable of XYZ motion and 360^o rotation about the Z-axis (See Figure 3-2). It is used to maneuver the sample into position for the various parts of the experiment: sputter cleaning, evaporation, Auger Spectroscopy, and magnetic characterization. The manipulator is also capable of rotating the substrate 180^o about its normal. Such rotation is crucial to our study in order that the magnetic anisotropy in the plane of the film can be characterized. All of the materials on the sample holder are nonmagnetic; therefore, it does not interfere with the magnetic measurements performed on the film.

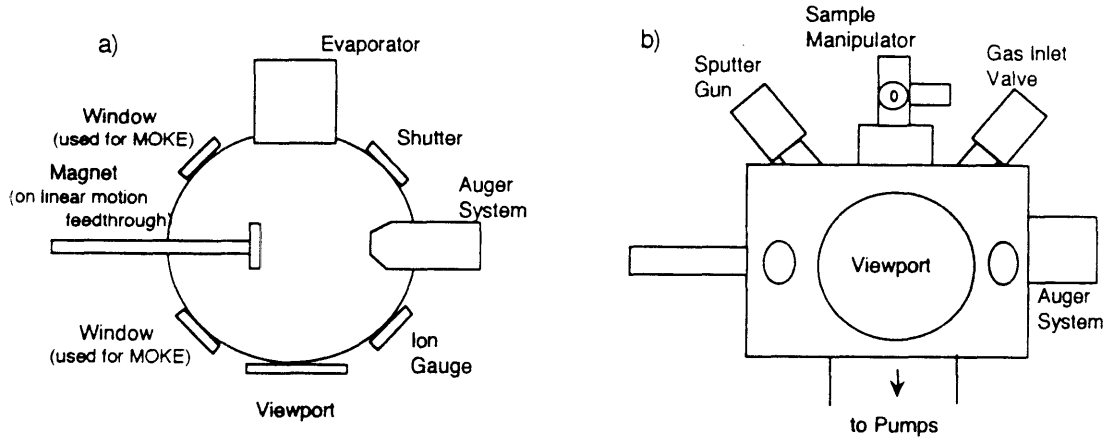

Figure 3-1: Vacuum chamber: a) top view, b) side view.

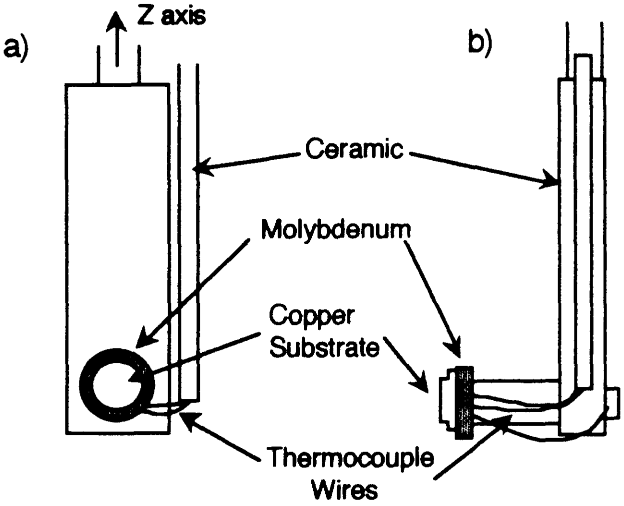

Figure 3-2: Sample holder: a) front view, b) side view.

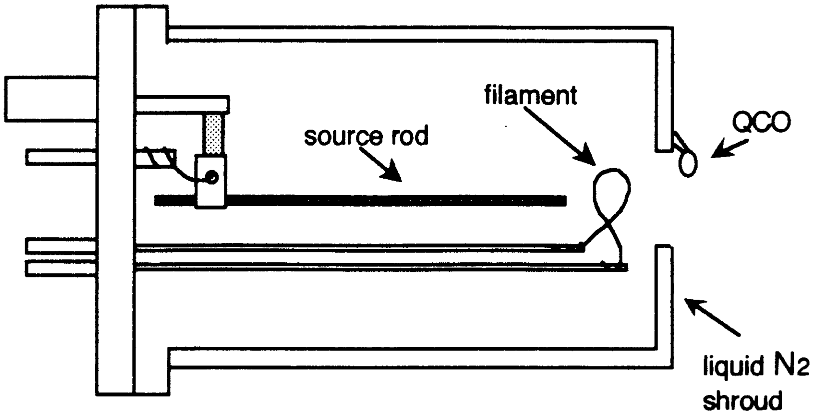

Figure 3-3: e$^-$–beam Evaporator

The single-crystal Cu substrates are cleaned *in-situ* via Ar$^+$ ion sputtering. After sputter cleaning, the substrate is annealed to 700°C to allow the surface to heal and any bulk contaminants to diffuse to the surface. Several cycles of sputtering and annealing are performed until the substrate is clean ($< 1\%$ surface contamination). The cleanliness of the substrate is checked using Auger Electron Spectroscopy, which will be described below. The main contaminants on the copper substrate are oxygen and carbon.

When the substrate is clean, the ultrathin film is deposited using e$^-$-beam evaporation. A schematic of the evaporator designed and built for this study is shown in Figure 3-3. Evaporation of the source is achieved using electron beam heating. A tungsten filament is used to supply electrons, and a positive voltage is applied to a source rod accelerating the electrons to the rod where their energy is transferred to the source, melting and evaporating the tip. The Co and $Ni_{78}Fe_{22}$ sources were 99.99% and 99.9% pure, respectively. They were both extensively outgassed before deposition. e$^-$-beam evaporation is a rather clean deposition technique because only the tip of the source is evaporated. The evaporating material is not in contact with any crucible which might contaminate it.

The amount of material being deposited is monitored by a quartz crystal oscillator (QCO). The deposition rate as given by the QCO is calibrated with film thickness by monitoring the growth of thick films which can be measured *ex situ* using a step profilometer. The thickness is also calibrated using the Auger spectrum as described below. The deposition rate is approximately 0.5 Å/min.

The composition of permalloy films e$^-$-beam deposited using our permalloy source was examined by Auger depth profiling [40]. The films had the same composition as the source rod throughout the film thickness. This indicates that neither the Ni nor the Fe preferentially evaporate from the source.

The chamber used for these experiments is not equipped to characterize the growth mode of the films or the crystalline quality of the film and substrate. While the intent of the proposed experiments is to study magnetic properties and not film growth, the two are interrelated because the magnetic properties depend on the microstructure of the film. The growth mode is affected by such parameters as substrate temperature, deposition rate, substrate orientation, etc. The growth conditions used for this study are those used by our collaborators, as described in Ref. [72], who have extensively studied the growth of Co/Cu(001). Because the quality of the films is an important factor in determining its magnetic properties, further capabilities for characterizing and controlling growth in this chamber must be developed.

3.2 Auger Spectroscopy

In this study, Auger spectroscopy is used both to check the cleanliness of the substrate and film, and to determine film thickness. Auger electron spectroscopy is based on a radiationless electron transition called the Auger effect. In the Auger process, a core level of a surface atom is ionized by an impinging beam of electrons, as shown in Fig. 3-4a. The excited atom can decay to a lower energy state if one of its outer electrons drops into the vacant core level. Depending on the incident beam energy, the energy which is produced by such a valence level–core level transition can be released as radiation, or alternatively, by the radiationless Auger process (Fig. 3-4b). In the latter case, the excess energy from the transition is given to an outer electron of the same atom, which is then ejected from the atom with that characteristic kinetic energy.

Due to the small inelastic mean-free-path of electrons, Auger electrons from atoms within only the first few layers will escape without significant loss of energy. Such electrons will give peaks in the energy distribution of secondary electrons. The energy and shape of these Auger peaks can be used to determine the composition of the surface. Auger spectra can

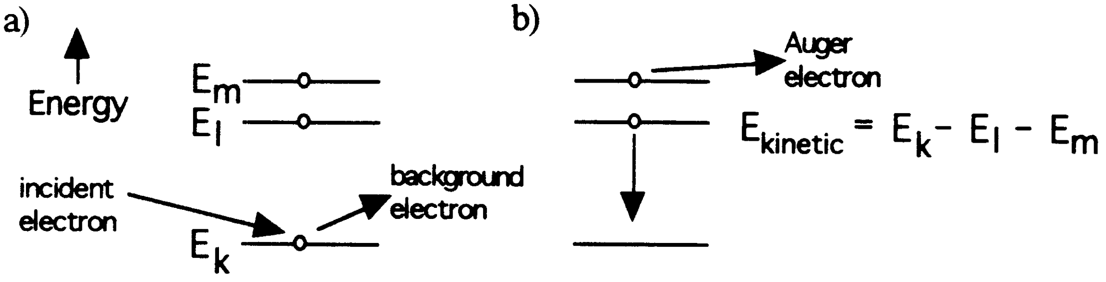

Figure 3-4: The Auger process: a) core level ionization, b) release of Auger electron.

also be used to determine the thickness of ultrathin films. The ratio of the peak intensity of the substrate species and the peak intensity of film species decreases as the film thickness increases as shown in Figure 3-5. [54]

3.3 Magneto-Optic Kerr Effect

The magnetic properties of the films are characterized using a magneto-optic technique. There are two major magneto-optic effects: the Faraday effect, and the Kerr effect. Both of these effects involve rotation of the angle of polarization for linearly polarized light. The Faraday effect occurs when light passes through a transparent medium in the presence of a magnetic field; the Kerr effect occurs when light is reflected from a ferromagnetic material.

Although the microscopic origin of magneto-optic Kerr effect (MOKE) is well established [73, 74, 75, 76], MOKE can most easily be described in terms of the anisotropy induced in the optical parameters of a material by its magnetization. The conductivity tensor for structures with at least cubic symmetry, magnetized in the z direction is of the form below:

$$\sigma = \begin{pmatrix} \sigma_{xx} & \sigma_{xy} & 0 \\ -\sigma_{xy} & \sigma_{xx} & 0 \\ 0 & 0 & \sigma_{zz} \end{pmatrix} \tag{3.1}$$

The elements of this tensor are generally complex: $\sigma_{ij} = \sigma_{ij}^{(1)} + i\sigma_{ij}^{(2)}$. The absorptive part of the conductivity is represented by the real part $(\sigma^{(1)})$ of the diagonal elements, and the imaginary part, $(\sigma^{(2)})$ of the off-diagonal elements. The absorptive component of a diagonal element is related to the sum of the absorption of left-circularly polarized light (LCP) and

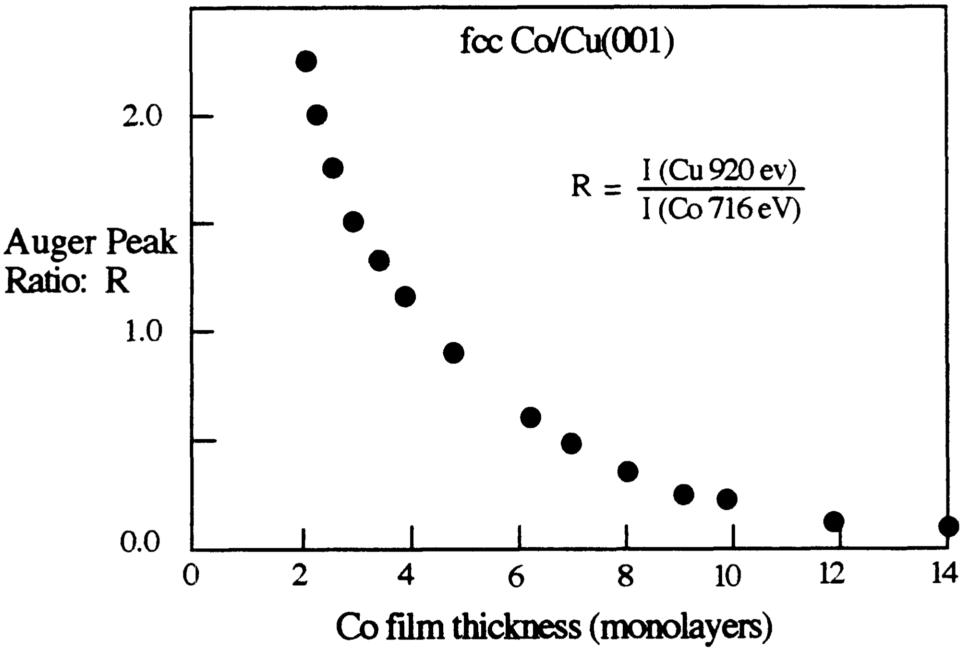

Figure 3-5: Auger-peak ratio as a function of film thickness.

right circularly polarized light (RCP), while the off-diagonal element is related to their difference [74].

$$\sigma_{xx}^{(1)} = P_{LCP} + P_{RCP} \qquad \sigma_{xy}^{(2)} = P_{LCP} - P_{RCP} \tag{3.2}$$

P is the power absorbed by a solid interacting with an electric field. Thus, if $\sigma_{xy}^{(2)}$ is finite, the LCP and RCP components of the light are absorbed by different amounts in the material and the state of the light's polarization changes. Light which was initially linearly polarized becomes elliptically polarized and the plane of polarization is rotated upon reflection from or transmission through a material with a finite $\sigma_{xy}^{(2)}$.

The relation of $\sigma_{xy}^{(2)}$ to the magnetization of the sample was calculated by Argyres using a quantum mechanical approach which included the spin-orbit interaction [73]. He found a direct proportionality between $\sigma_{xy}^{(2)}$ and magnetization. However, it is difficult to use MOKE as an absolute magnetometer because of the importance of spin-orbit interaction strength, scattering geometry, and photon energy dependence, etc. on the signal size. An important point is that the only temperature dependence of the magneto-optical effects is due to the M(T) behavior of the material, thus MOKE can be used to probe M(T).

For magnetic characterization, the sample is maneuvered into the gap of an electromagnet inside the vacuum chamber. The magnet is capable of applying in-plane fields up to

600 Oe. Because the sample manipulator can rotate the sample about its normal, the magnetic field can be applied along any in-plane direction. There is a heating filament mounted inside the magnet's gap which is used to heat the sample in order to study the temperature dependence of the magnetic anisotropy. The temperature of the sample is monitored using a thermocouple on the sample-holder, as shown in Fig. 3-2.

The MOKE set-up is shown in Figure 3-6. Polarized light from a 3mW He-Ne laser is passed through a polarizer. The laser and polarizer are configured to produce s-polarized light, which is light whose electric field vector oscillates perpendicular to the plane of incidence. This plane is defined by the propagation vector of the light and the normal to the sample's surface. The light enters the vacuum chamber through a window and is reflected by the sample. The reflected beam travels out through another window, and through a $\lambda/4$-retarder. The $\lambda/4$-retarder removes any ellipticity in the polarization caused by birefringence in the windows. Finally, the light passes through another polarizer, called the analyzer, and into a photodiode detector. The analyzer is set slightly off extinction with respect to the initial polarizer. The amount of light which is able to pass through the analyzer is proportional to the amount of rotation due to MOKE, and is referred to as the Kerr intensity. In order to improve the signal-to-noise ratio, the laser beam is chopped before it enters the chamber, and a lock-in amplifier is used to read the output of the photodiode. The resulting M(H) loop is an average response over the area of the sample illuminated by the laser beam ($\approx$1mm^2).

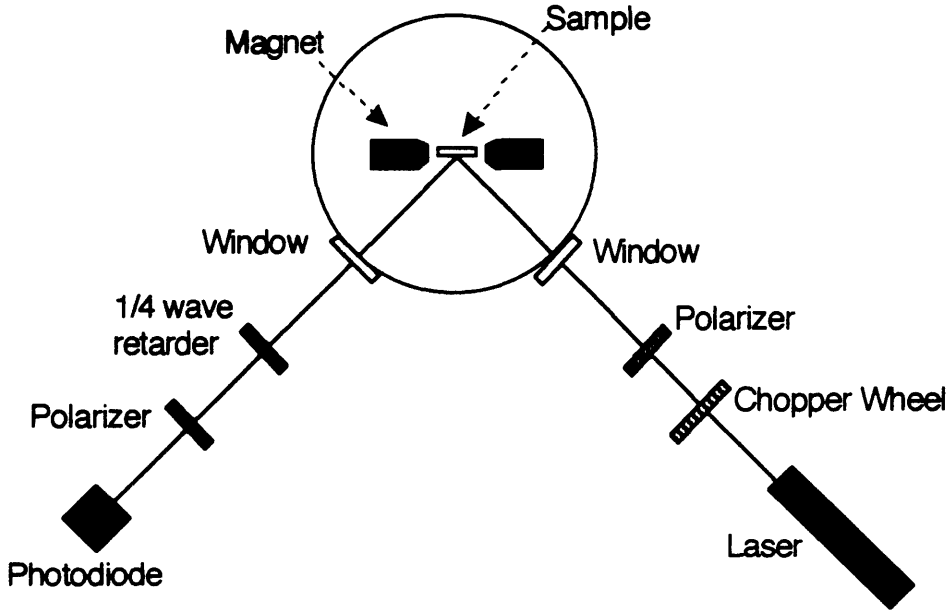

Figure 3-6: Optics and magnet used in measuring the magneto-optic Kerr effect.

Chapter 4

Magnetic Anisotropies

Given the review in chapter 2, and the explanation of experimental techniques in chapter 3, we now present the experimental results and discuss their implications. We have observed that vicinal Co and $Ni_{79}Fe_{21}$ films grown on Cu(11n) surfaces exhibit uniaxial in-plane magnetic anisotropy. As described in section 1.2, we investigated three possible mechanisms through which the presence of surface steps can induce a uniaxial anisotropy in vicinal films. Each part of the study presented below was designed to test one of those mechanisms. The strength of the anisotropy in Co/Cu(11n) films decreases with increasing thickness and increasing terrace width. The anisotropy in Co/Cu(1 1 13) films goes from uniaxial to nearly biaxial as the temperature is increased from 27°C to 127°C. The uniaxial anisotropy in $Ni_{79}Fe_{21}$/Cu(117) films, while still definitely present, is much weaker than that found in cobalt films on the same surface. Our experimental results are all consistent with anisotropy due to broken symmetry around the step-edges; but we cannot totally rule out the other mechanisms (magnetoelastic and magnetostatic anisotropy), as will be discussed here in Ch. 4 and further in Ch. 5 and Ch. 6.

4.1 Co/Cu(11n)

The in-plane anisotropy in Co/Cu(11n) is uniaxial with the magnetic easy axis parallel to the $[1\bar{1}0]$ direction. As discussed in Sec. 2.5, Cu(11n) surfaces are made up of (001) terraces separated by atomic steps which are also parallel to $[1\bar{1}0]$. Recall that the in-plane anisotropy in Co/Cu(001) films has four-fold symmetry. Through some mechanism the presence of the atomic steps on the vicinal surface has induced the uniaxial magnetic

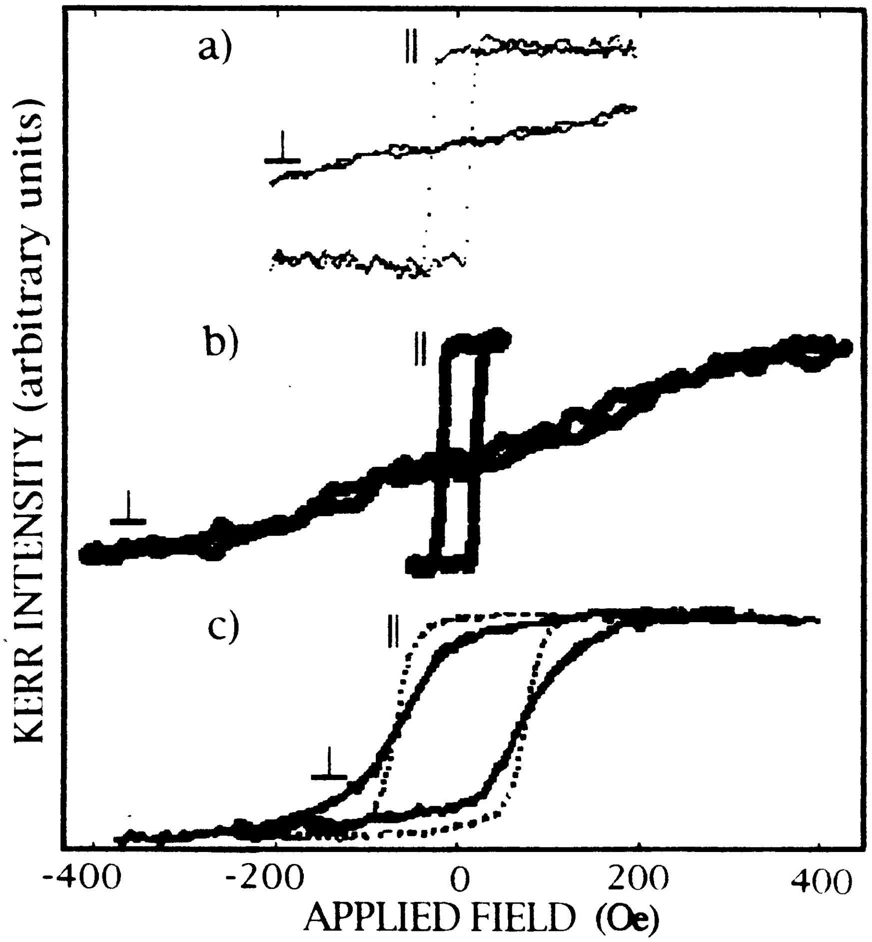

Figure 4-1: Hysteresis loops taken with the field applied parallel and perpendicular to the steps in a) 6 ML, b) 14 ML, and c) 20 ML of Co/Cu(1 1 13).

anisotropy in the Co/Cu(11n) films.

4.1.1 Thickness Dependence

In order to determine that the uniaxial anisotropy in Co/Cu(11n) vicinal films is a surface effect, we measured hysteresis loops as a function of cobalt film thickness. In figure 4-1 are hysteresis loops taken parallel and perpendicular to the steps for a) 6 ML, b) 14 ML, and c) 20 ML of Co/Cu(1 1 13). In figure 4-2 are the results for a) 6ML and b) 14 ML of Co/Cu(117). In all the films, the direction parallel to the steps is magnetically easy and the direction perpendicular to the steps is the hard axis. This is revealed by the fact that it takes a higher field to saturate the films perpendicular to the steps.

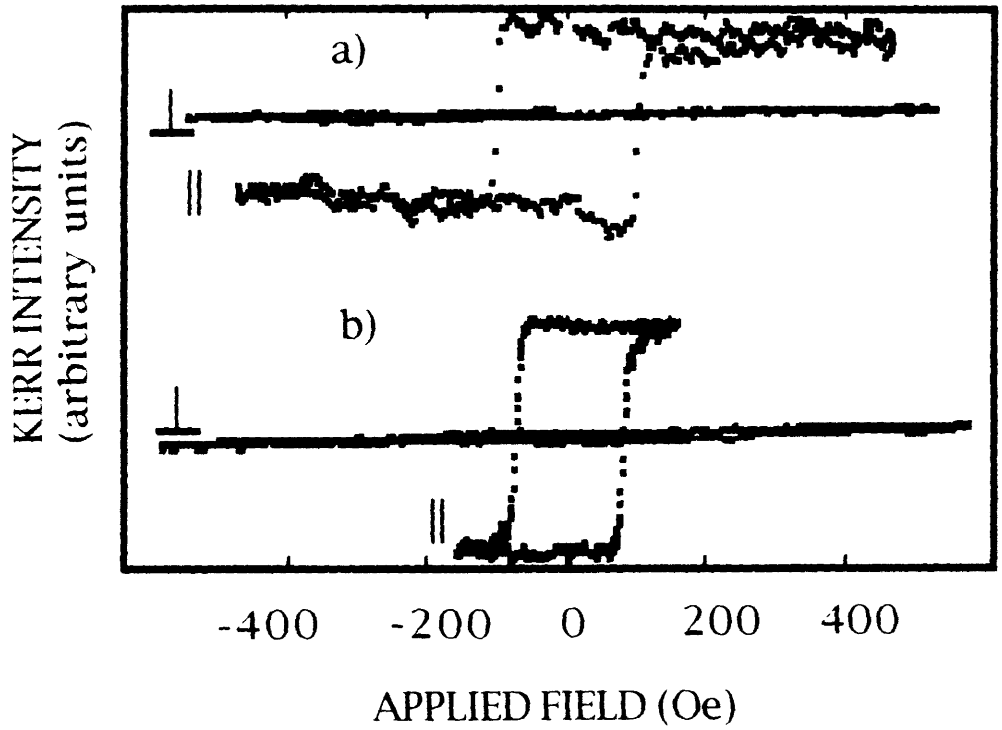

Figure 4-2: Hysteresis loops taken with the field applied parallel and perpendicular to the steps in a) 6 ML and b) 14 ML Co/Cu(117).

The thickness dependence is most clearly seen upon examination of the Co/Cu(1 1 13) results. As demonstrated in Fig. 4-1, the uniaxial anisotropy strengthens as the film thickness decreases. For thinner films, a larger applied field is required to saturate the material in the direction perpendicular to the steps. For the 14 and 20 ML films, we can calculate an anisotropy energy density, $\Delta E_{||-\perp}$, directly from the hysteresis loops, assuming the bulk value for M_s. As illustrated in Fig. 2-2 on page 20, the anisotropy energy density is roughly $(1/2)H_kM_s$, where H_k is the anisotropy field at which the film is saturated in the hard direction. For the 6 ML film, in which the hard axis could not be saturated with the magnetic field available *in-situ*, we cannot directly determine $\Delta E_{||-\perp}$. An extrapolation of the hard axis loop to the saturation magnetization for the film, as determined from the easy axis loop, can be used to get a reasonable estimate of $\Delta E_{||-\perp}$. The anisotropy values obtained for these films are plotted in Fig 4-3. For the Co/Cu(117) films, because the hard axis loops are so far from saturation, it is difficult to extrapolate meaningful quantitative values for the anisotropies.

If the uniaxial anisotropy is caused by the reduced symmetry around atoms at the surface steps, we expect the strength of the anisotropy to decrease as the thickness increases. Néel proposed that such surface anisotropies will have a 1/t dependence, where t is the thickness of the film [1]. We discuss in detail how to model these anisotropies in chapter 5. In order to compare the experimental results presented here to the model, we have fit the anisotropies measured in Co/Cu(1 1 13) films to the form $\Delta E_{||-\perp} = E_{bulk} + E_{surface}/t$. That fit, given in Eq. 4.1, is shown in Fig. 4-3 along with the data, and is given by

$$\Delta E_{||-\perp} = (-0.6 - \frac{25}{t})\,\mathrm{x}\,10^5 \quad \mathrm{erg/cm^3}. \tag{4.1}$$

To summarize, the important facts concerning the thickness dependence of the anisotropy in Co/Cu(11n) films are the following: 1) for all film thickness studied, there is a uniaxial in-plane anisotropy, 2) the easy axis is always parallel to the steps, and 3) the strength of the anisotropy increases consistent with t^{-1} as the film thickness decreases. The final point indicates that the mechanism through which the steps induce the uniaxial anisotropy is a surface effect.

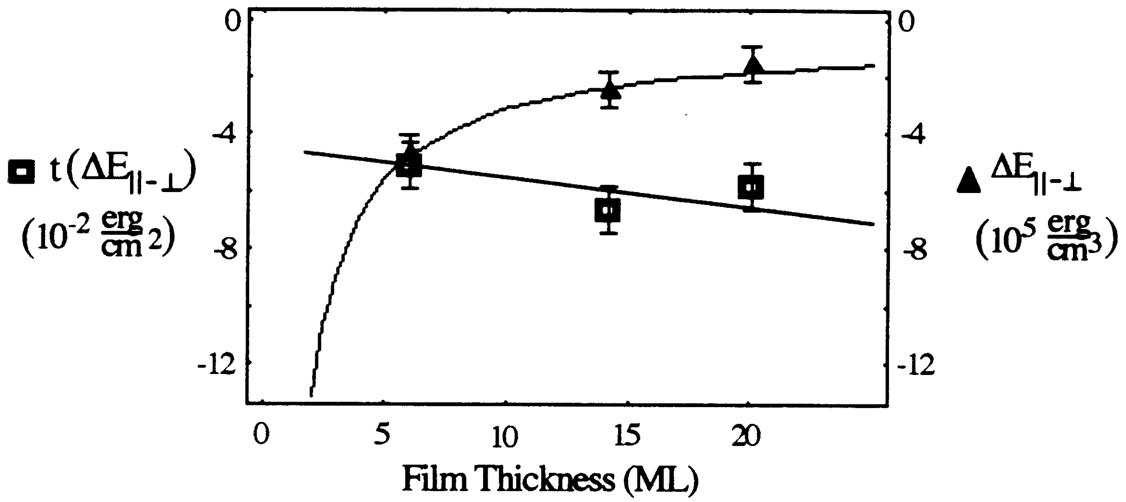

Figure 4-3: Anisotropy as a function of thickness in Co/Cu(1 1 13). The triangles indicate the anisotropy alone, and the squares indicate the anisotropy multiplied by the thickness. The solid curve is the fit to the data given by Eq. 4.1; the solid straight line is Eq. 4.1 multiplied by the film thickness.

4.1.2 Terrace-Width Dependence

While the thickness dependence of the anisotropy indicates that it is a surface effect, we can not yet deduce that it is a surface step-edge effect. In order to do so, we investigated the anisotropy as a function of terrace width, or equivalently as a function of surface step density.

To demonstrate this behavior, we examine the in-plane anisotropy in Co films of the same thickness grown on both a Cu(1 1 13) substrate and a Cu(117) substrate. As shown in Sec. 2.5, the terraces on the substrate are on average 6.5 atoms and 3.5 atoms wide, respectively. The hysteresis loops taken with the external field applied at various in-plane angles are shown for a 14 ML Co/Cu(1 1 13) film in Fig. 4-4 and for a 14 ML Co/Cu(117) film in Fig. 4-5. The angle β indicates the angle between the applied field and the direction parallel to the steps. Along the hard axis ($\beta = 90^o$), the (1 1 13) film saturates at approximately 400 Oe, while at the same field strength, the (117) film is still far from saturating. The uniaxial anisotropy is strongest in the film with the narrowest terraces, or the greatest step density. This trend indicates that the step-edges are important in determining the strength of the uniaxial anisotropy.

4.1.3 Magnetization Reversal

Another piece of information that can be obtained from the **M-H** loops in Fig. 4-5 is the mechanism through which the magnetic moments in the film align with the external field. Figure 4-6 is a plot of the coercive field (H_c) and the remanent Kerr intensity normalized to the intensity at saturation ($I_K(0)/I_K(H_k)$) as functions of the angle between the applied field and the steps in the film (β). The coercive field, shown in circles, is the half-width of the M-H curve at zero magnetization, and the remanent Kerr intensity, shown in stars, is proportional to the component of magnetization parallel to the field direction when $H_{ext}=0$. Superimposed on the coercivity data is a dashed curve representing the easy axis coercivity ($H_{c,\beta=0}$) divided by $\cos\beta$; along with the Kerr intensity data , $\cos\beta$ is plotted as a solid line.

The trends in the H_c and $I_K(0)$ both indicate that the films respond to an external field first by domain wall motion, and then, after a single domain state is achieved, **M** rotates into the direction of the field. This result is readily explained through geometric arguments. Consider Fig. 4-7a, a simple representation of a demagnetized film oriented with the easy axis parallel to the applied field (H_{ext}). Once the field is greater than the coercivity ($H_{c,\beta=0}$), the domains in which **M** is parallel to the field will grow at the expense of the antiparallel domains (Fig. 4-7b). With the barrier to domain wall motion overcome, the film quickly saturates in the direction of the applied field, and the Kerr intensity at our maximum applied field is $I_K(H_k)$ (Fig. 4-7c). The corresponding easy axis M-H loop is shown in Fig. 4-7d. The experimental loops taken for the 14 ML films of Co/Cu(11n) n = 7 and 13 with the field parallel to the steps ($\beta = 0°$) show this type of easy axis behavior (Figs. 4-4 and 4-5).

In Fig. 4-8a, the film is now oriented such that its easy axis is perpendicular to the applied field ($\beta = 90°$). In this case, domain wall motion does not decrease the magnetic energy of the film; none of the domains contain **M** parallel to the field. The applied field will cause **M** to rotate into the direction of the field (Fig. 4-8b). The expected M-H curve for a uniaxial material is shown in Fig. 4-8d, which corresponds reasonably well to the $\beta = 90°$ M-H curve in Fig. 4-4. If the maximum applied field is much less than H_k, the observed M-H loop will represent only a portion of Fig. 4-8d, showing only a shallow straight line.

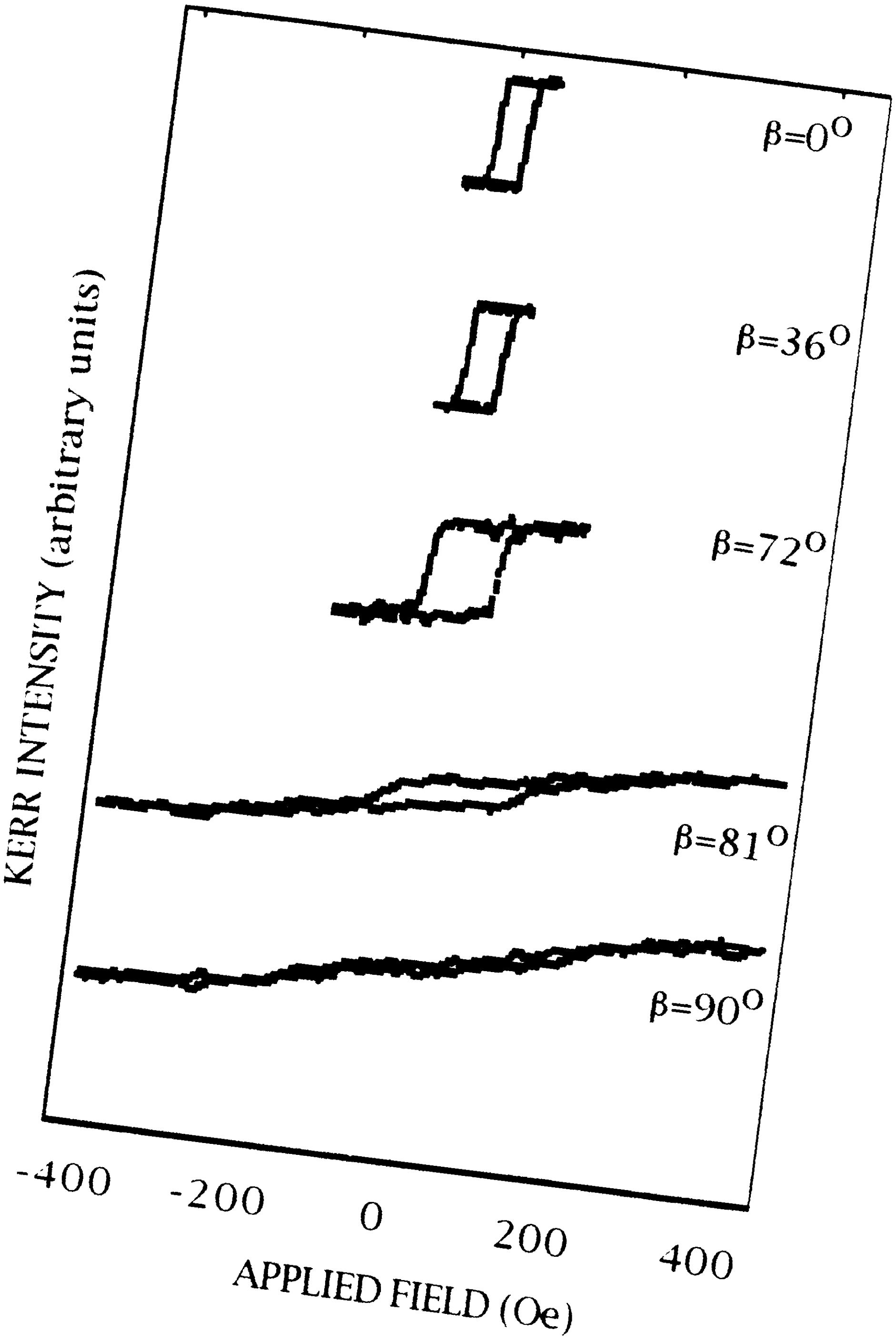

Figure 4-4: Hysteresis loops of a 14 ML Co/Cu(1 1 13) film, taken for various angles β between the applied field and the steps.

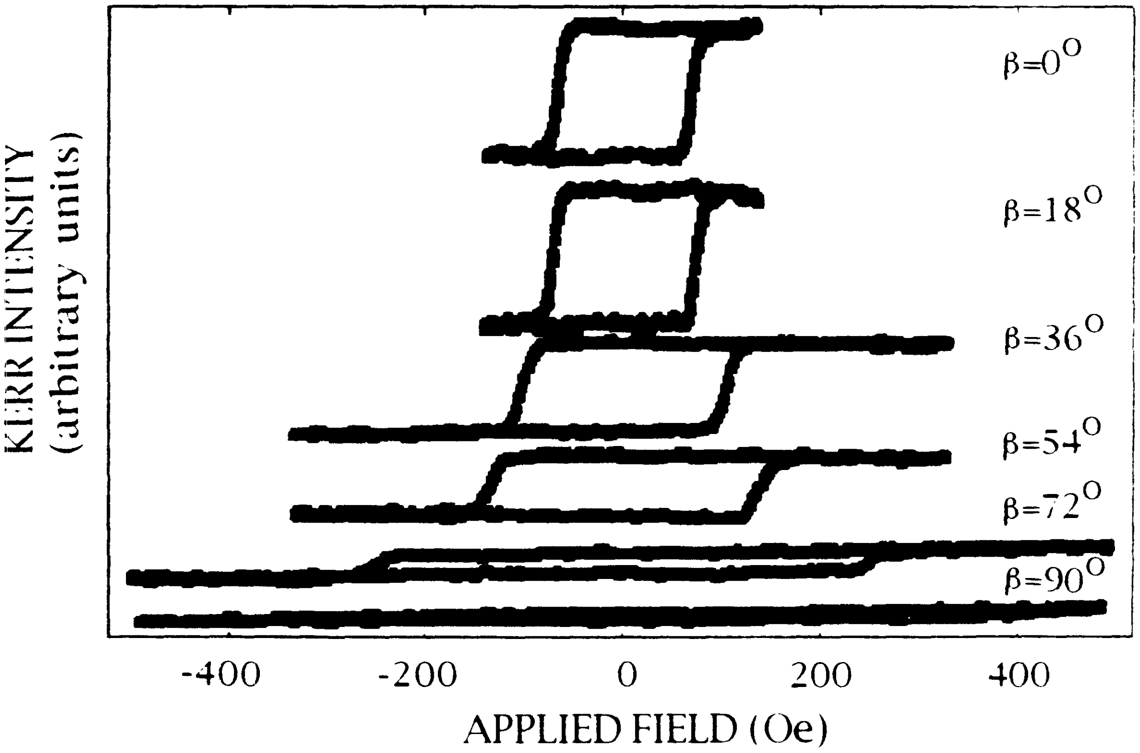

Figure 4-5: **Hysteresis loops of a 14 ML Co/Cu(117) film, taken for various angles β between** the applied field and the steps.

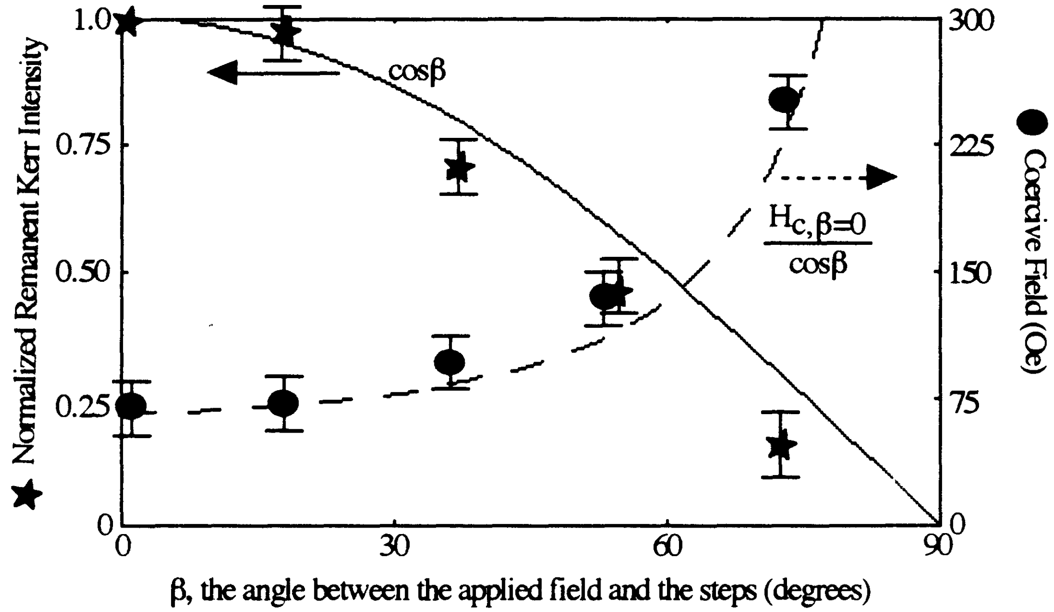

Figure 4-6: The coercive field (circles) and the normalized remanent Kerr intensity (stars) as functions of the angle β between the applied field and the steps in the 14 ML Co/Cu(117) film. The dashed and solid curves represent $(\mathrm{H}_{c,\beta=0}/\cos\beta)$ and $\cos\beta$, respectively

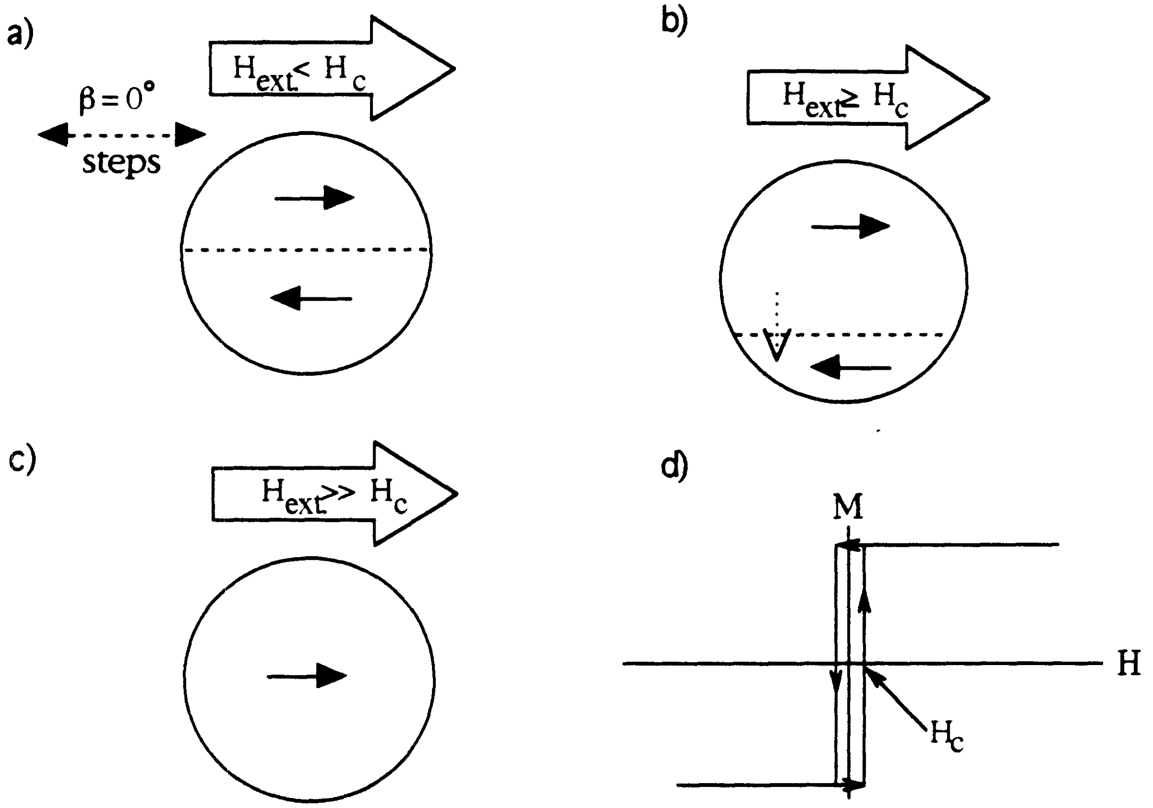

Figure 4-7: Magnetization reversal process for an external field (H_{ext}) applied parallel to the easy axis in a uniaxial material ($\beta = 0^\circ$): a) $H_{ext} < H_{c,\beta=0}$, b) domain wall motion, c) saturation, d) expected hysteresis loop.

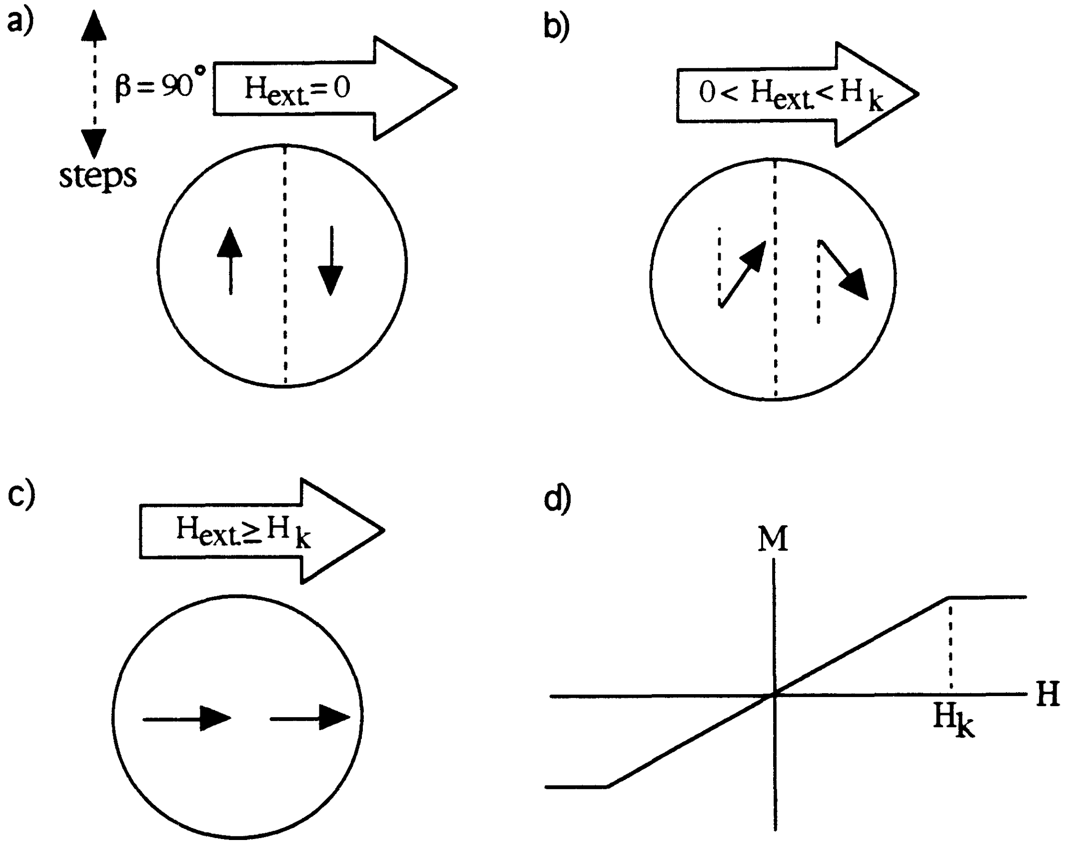

Figure 4-8: Magnetization reversal process for an external field (H_{ext}) applied perpendicular to the easy axis in a uniaxial material ($\beta = 90^o$): a) demagnetized state, b) rotation, c) saturation, d) expected hysteresis loop.

Such behavior is found for $\beta = 90^o$ in the Co/Cu(117) films (Fig. 4-5). We will show in the next section that the portion of the loop between the positive and negative anisotropy fields ($-H_k < H_{ext} < H_k$) is not strictly linear because the Co/Cu(11n) films have a combination of cubic and uniaxial anisotropies.

When the field and easy axis are neither parallel nor perpendicular, the magnetization reversal occurs by a combination of domain wall motion and rotation, as illustrated schematically in Fig. 4-9. Although neither of the domains contains **M** parallel to the field in the demagnetized state, one of them has a larger component parallel to the field than the other, and thus has a lower Zeeman energy (Sec. 2.1). This domain will grow at the expense of the higher energy domain as soon as the applied field is strong enough to overcome any barriers to domain wall motion. Upon the initial increase in field, if the field is not yet strong enough to cause wall motion, the magnetization in both domains rotates slightly toward the direction of the field (Fig. 4-9a). The component of field which works on the

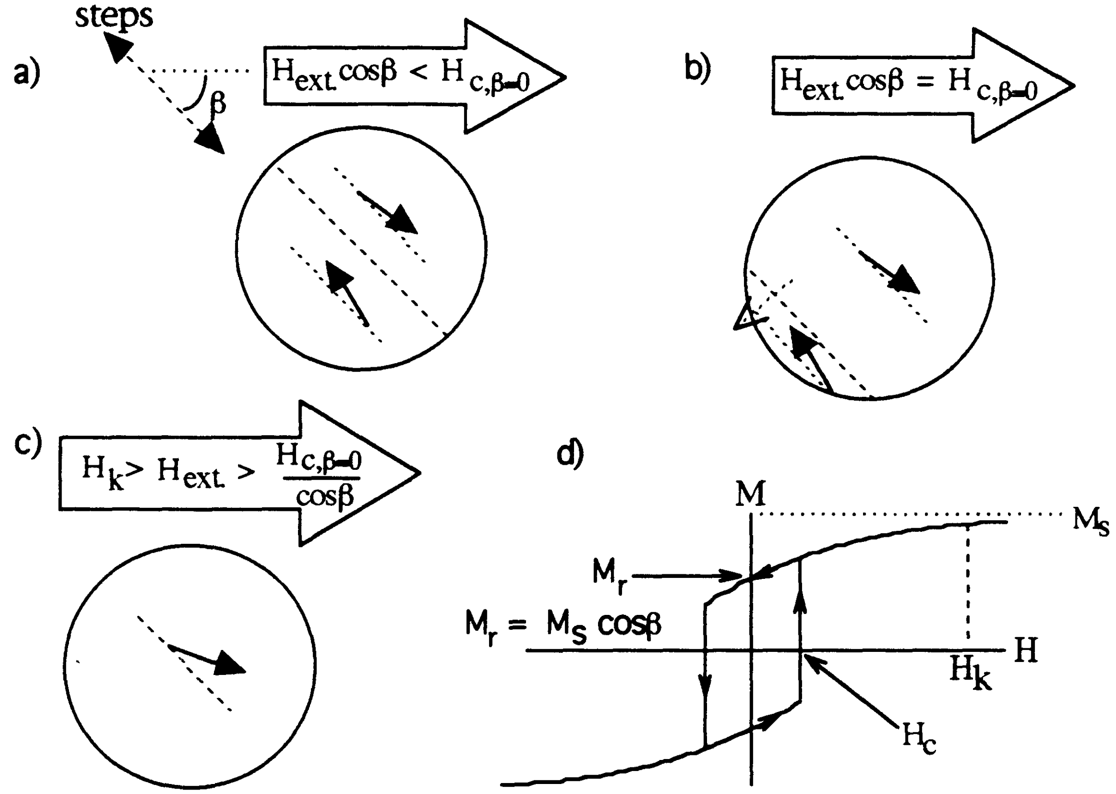

Figure 4-9: Magnetization reversal process for an external field (H_{ext}) applied at an angle β away from the easy axis in a uniaxial material: a) $H_{ext} \cos\beta < H_{c,\beta=0}$, b) domain wall motion, c) rotation, d) expected hysteresis loop.

domain walls is that which is parallel to the easy axis: $H_{ext} \cos\beta$. When this component is greater than the easy axis coercivity ($H_{c,\beta=0}$), the domain walls will move, quickly putting the film in a single domain state. (Fig. 4-9b). Upon a further increase in the applied field, the magnetization continues to rotate toward the direction of the field (Fig. 4-9c).

The expected hysteresis loop for $0^o < \beta < 90^o$ is shown in Fig. 4-9d. The coercivity is given by $H_{c,\beta=0}/\cos\beta$, the field value at which the film becomes a single-domain. As the magnetization rotates into the direction of the field, the M-H response is not linear as it was when β was ninety degrees (Fig. 4-8d). The form of the M-H curve in the region of $H>H_c$ can be obtained using the SW model, described in Sec. 2.1 on page 20, by minimizing the Zeeman and anisotropy energies with respect to the orientation of the magnetization. When the applied field is returned to zero, **M** will rotate back to the nearest easy axis. At $H_{ext}=0$, the component of magnetization in the direction of the applied field, the remanent magnetization, is given by $M_r=M_s \cos\beta$. The expected loop corresponds quite well to the

M-H loop obtained for $\beta = 81^o$ in the 14 ML Co/Cu(1 1 13) film (Fig. 4-4). If the maximum applied field is greater than $H_{c,\beta=0}/\cos\beta$, but still much less than H_k, we expect to see only the hysteresis portion of the loop in Fig. 4-9d. This is the case for the Co/Cu(117) films ($0^o < \beta < 90^o$) in which the step-induced uniaxial anisotropy is very strong (Fig. 4-5).

4.1.4 Temperature Dependence

In order to determine if magnetostatic energy of the terraced films was a major source of the uniaxial anisotropy, we studied the temperature-dependent behavior of the anisotropy. As show in Sec. 2.1 on page 17, the temperature dependence of magnetostatic effects goes as $[M(T)/M(0)]^2$. We expected this behavior to be discernible from the temperature dependence of magnetocrystalline anisotropies, which were described in Sec. 2.1 on page 18 ($K_u \propto [(T)/M(0)]^3$,$K_1 \propto [M(T)/M(0)]^{10}$). As this part of the study progressed, we realized that separation of the magnetostatic anisotropy would not be possible; however, we still gained valuable information regarding anisotropy in vicinal films by studying its temperature dependence.

We have examined the anisotropy in a 3 ML Co/Cu(1 1 13) film as a function of temperature (25°C - 130°C) [6]. The easy axis loops, taken parallel to the steps, are square loops throughout the temperature range studied with a room temperature coercivity of approximately 5 Oe. Both the coercivity and the saturation magnetization decrease as temperature increases, as expected in a ferromagnet. The Kerr intensity at saturation decreases less than 12% as temperature increases from 47°C to 127°C, indicating that M_s decreases less that 12% in this temperature range.

The hard-axis hysteresis loops, taken perpendicular to the steps, show interesting changes in the shape of the M(H) loop as temperature is varied. Three hard-axis loops are shown in Figure 4-10. At 25°C and just above, a loop with a positive curvature is observed, as in Fig. 4-10c for T=47°C. No measurable coercivity is detected on the steep portions of the M(H) loop. For temperatures near 100°C, the positive curvature is no longer observed and a simple hard-axis loop characteristic of that shown in Figure 4-10b is observed. At still higher temperatures, the entire system becomes soft and a nearly square loop is observed (Figure 4-10a). These changes in hard-axis **M-H** behavior are reversible; the strong uniaxial anisotropy returns when the temperature is decreased back to 25°C. This reversibility suggests that the changes are not due to interdiffusion of the Co and Cu.

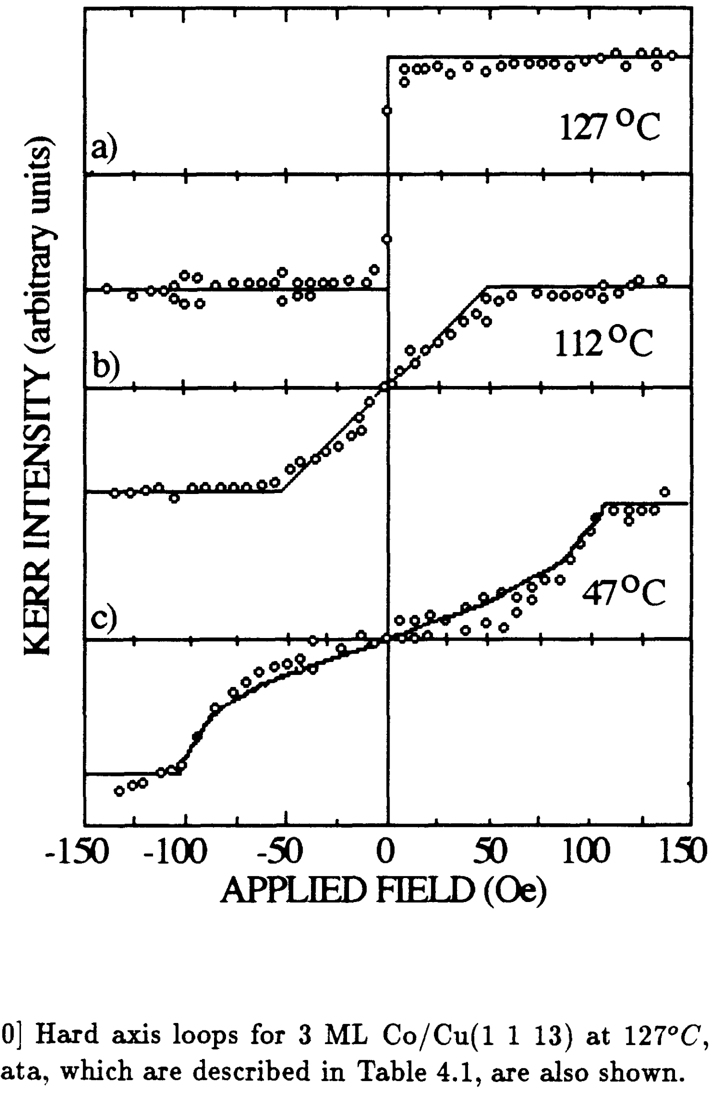

Figure 4-10: [110] Hard axis loops for 3 ML Co/Cu(1 1 13) at 127°*C*, 112°*C*, and 47°*C*. The fits to the data, which are described in Table 4.1, are also shown.

Phenomenological Analysis

The shapes of the hard axis loops can be reproduced from a free energy expression which contains a cubic anisotropy, K_1, and a uniaxial anisotropy, K_u [6]. The cubic term reflects the magnetocrystalline anisotropy in a (001) surface, while the uniaxial term reflects the effects of the steps.

The free energy density may be expressed as shown in Equation 4.2 in a coordinate system in which the x, y, and z axes are colinear with the [100], [010], and [001] directions in the fcc Co, as shown in Fig. 4-11.

$$f = K_1(\alpha_1^2\alpha_2^2 + \alpha_3^2\alpha_2^2 + \alpha_1^2\alpha_3^2) + K_u sin^2(\phi - 45^o) - \mathbf{M}\cdot\mathbf{H} \tag{4.2}$$

The α's in Equation 4.2 are the direction cosines of **M**. For **H** applied along the hard axis (**H**=(H/$\sqrt{2}$)[110]), and for **M** constrained to be in the plane of the film (**M**=$M_s[\alpha_1\ \alpha_2\ 0]$), the free energy expression reduces to

$$f = \frac{K_1}{4}sin^2 2\phi + K_u sin^2(\phi - 45^o) - \frac{M_s H}{\sqrt{2}}(cos\phi + sin\phi). \tag{4.3}$$

We can derive the expected shape of the hysteresis loop using the SW model described in Section 2.1 on page 20. Defining anisotropy fields $H_1=2K_1/M_s$ and $H_u=2K_u/M_s$, the predicted m(H) behavior follows the form:

$$m = -\frac{M_s H_0/2}{K_u + (1-2m^2)K_1} = -\frac{H}{H_u + (1-2m^2)H_1}. \tag{4.4}$$

m is the size of the magnetization component in the direction of the field, normalized to the saturation magnetization. We expect H_1 to be less than zero based on the fact that K_1, the magneto-crystalline constant for Co/Cu(001), is -1.2 x 10^6 erg/cm^3.

The anisotropy fields obtained by fitting the model to the data are listed in Table 4.1, and the predicted m-H curves are displayed on top of the data in Figure 4-10. The results indicate a weakening of the uniaxial contribution to the anisotropy as the temperature increases, and that the cubic anisotropy falls off much faster than the uniaxial anisotropy.

Upon first analysis, the weakening of the uniaxial anisotropy appears much too drastic to be consistent with a magnetostatic origin. Magnetostatic anisotropy fields ($H_i = 2K_i/M_s$) are expected to decrease by approximately 12% in these films between 47°C and 127°C, given

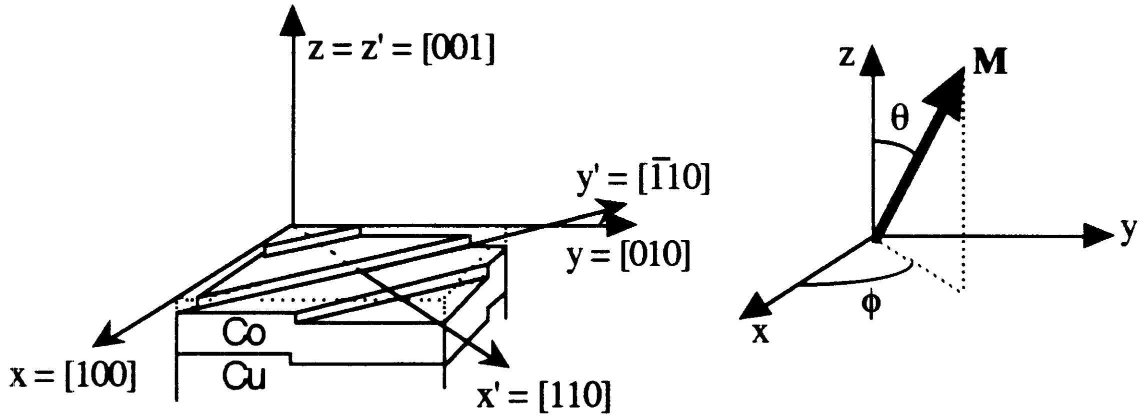

Figure 4-11: Schematic of a vicinal (11n) surface on which the *crystal* coordinate system (**x**=[100], **y**=[010], and **z**=[001]), and the *step* coordinate system (**x'**=[110], **y'**=[$\bar{1}$10], and **z'**=[001]) are indicated.

Temperature (°C)	*Observations*	*Anisotropy Fields*	
		H_u (Oe)	H_1 (Oe)
127	nearly square loop	-6	≈0
112	m linear in H	-50	≈0
47	positive curvature	-132	-33

Table 4.1: Model parameters used to fit MOKE data

the observed decrease in the magnetization. The uniaxial anisotropy field, as determined by our fit to the data, decreases by 95% over this temperature range.

The temperature dependence of the uniaxial anisotropy indicates that something in addition to thermal magnetic disordering is occurring in the vicinal Co film. Recall from Sec. 2.1 on page 19 that anisotropies should decrease as the material loses some of its magnetic order due to thermal effects, and that cubic anisotropy should fall off faster with temperature than uniaxial anisotropy, as is observed. However, the anisotropy should not go to zero until the film reaches the Curie temperature (T_C) and the film's long-range magnetic order is destroyed. In the 3 ML Co/Cu(1 1 13) film, the uniaxial anisotropy is near zero at approximately 130°C, yet the film is clearly magnetic and is still well below its Curie temperature (M_s has decreased only 12%).

The most likely explanation for this disappearance of anisotropy before T_C is structural disordering at the surface. In Cu(11n) films, thermal roughening of the surface steps is significant at temperatures just above room temperature [69, 67]. As discussed in Sec. 2.5, we would expect that the roughening temperature is slightly higher in Co/Cu(1 1 13) due to the higher T_M of cobalt. When the steps become rough, characterized by a high density of kinks along the step-edge, any uniaxial anisotropy due to well ordered steps will diminish. The fact that the steps thermally disorder then prevents us from excluding a magnetostatic contribution to the anisotropy based purely on the results of our temperature-dependent data. The disappearance of the uniaxial anisotropy well below the Curie temperature in Co/Cu(11n) is consistent with the conclusion that this anisotropy is due to the symmetry at the step-edges *and* the conclusion that it is of magnetostatic origin.

In summary, from our temperature-dependent study of the anisotropy we see that the uniaxial anisotropy in the vicinal film vanishes when the temperature is increased to approximately 130^oC. From our model of the temperature-dependent behavior, we make the following conclusions: 1) the anisotropy in Co/Cu(11n) films can be modeled as a combination of cubic and uniaxial anisotropies, 2) the uniaxial anisotropy constant goes to zero upon an increase in temperature well before the Curie temperature, and 3) the anisotropy most likely disappears around 130°C due to thermal roughening of the steps.

4.1.5 Magnetostatic (Shape) Anisotropy of a Vicinal Film

We had hoped that through the temperature-dependent study of the anisotropy, we might determine the importance of magnetostatic effects in vicinal films. Unfortunately, because of the presumed step roughening, we were not able to make such a determination. In an alternate approach, we have calculated the magnetostatic energy of a vicinal film by treating it as a collection of discrete magnetic dipoles. This calculation follows the treatment by Draaisma and de Jonge [31], mentioned in Sec. 2.2 on page 22.

The magnetostatic anisotropy due to a collection of dipoles is calculated using the following steps: 1) The dipole energy (ϵ_i) of each magnetic dipole i in the film must be calculated. ϵ_i is the energy of the dipole in the field of all the other dipoles in the film, and it will depend on the orientation of the magnetic moments. 2) The anisotropy energy ($\Delta\epsilon_{MS,i}$) per dipole is then calculated by taking the difference between the dipole energy with the moments all pointed in one direction (e.g. parallel to the steps) and with $\mathbf{m}$ pointed in another direction (e.g. perpendicular to the steps). 3) The final step in calculating the anisotropy energy ($\Delta\epsilon_{MS}$) for the entire film is to sum the individual anisotropies for all the dipoles ($\Delta\epsilon_{MS,i}$).

The energy of a magnetic dipole i in the field of other parallel dipoles in the film is

$$\epsilon_i = -\frac{\mu_o}{8\pi a^3}\sum_{j\neq i}\left(-\frac{m^2}{r_{ij}^3}+\frac{3(\mathbf{m}\cdot\mathbf{r}_{ij})^2}{r_{ij}^5}\right) \tag{4.5}$$

$\mathbf{m}$ is the magnetic moment of a dipole, $\mathbf{r}_{ij}$ is the relative position of dipoles i and j ($\mathbf{r}_{ij}$=$\mathbf{r}_i$-$\mathbf{r}_j$), and a is the lattice constant. The anisotropy energy of a given dipole i is

$$\Delta\epsilon_{MS,i} = -\frac{\mu_o m^2}{8\pi a^3}\sum_{j\neq i}\left(\frac{3[(\hat{\mathbf{m}}_1\cdot\mathbf{r}_{ij})^2) - (\hat{\mathbf{m}}_2\cdot\mathbf{r}_{ij})^2]}{r_{ij}^5}\right) \tag{4.6}$$

where $\mathbf{m}_j$ are unit vectors in the direction of the magnetization. For example, to calculate the in-plane anisotropy for dipole i in a vicinal film, $\Delta\epsilon_{MS,i,||-\perp}$, $\mathbf{m}_1$ would be the unit vector parallel to the steps, and $\mathbf{m}_2$ would be the unit vector perpendicular to the steps. In obtaining the results presented here, this sum was performed for all dipoles in a cylinder with an approximate radius of 100 dipoles (or atoms) centered on dipole i.

The magnetostatic anisotropy energy of the entire film ($\Delta\epsilon_{MS}$) is then just the summation of $\Delta\epsilon_{MS,i}$ over all the dipoles in the film. To make sure we account for all of them, we have a numbering scheme for the dipoles as depicted in Fig. 4-12. The figure is a schematic

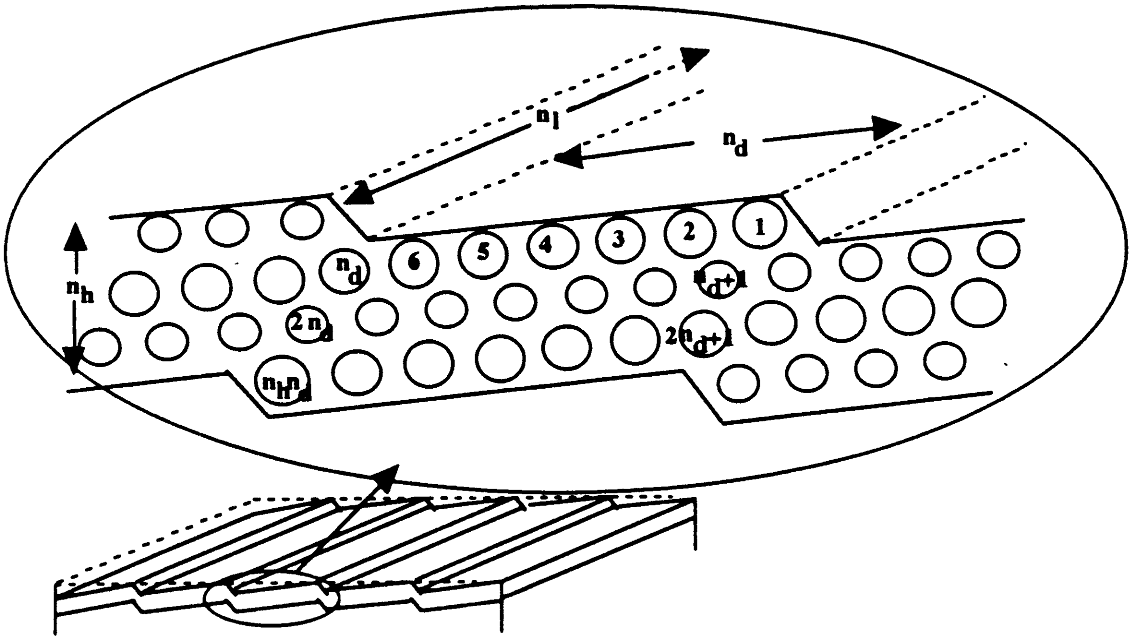

Figure 4-12: Schematic cross-section of a vicinal film indicating the dimensions and dipole numbering scheme used in the calculation of the magnetostatic energy of the film. Some atoms are represented by smaller circles to indicate that they are a distance of one interatomic spacing into the film.

cross-section of the film and the dimensions indicated are consistent with the dimensions used in deriving the Néel anisotropy in vicinal films in Appendix A. n_h is the number of monolayers in the film, n_l is the length of the film in atoms measured parallel to the steps, and n_d is the width of a terrace in atoms measured perpendicular to the steps. The number of dipoles (or atoms) in one step is the product $n_l n_d n_h$. If n_{steps} is the number of steps in the film, the magnetostatic anisotropy energy is

$$\Delta\epsilon_{MS} = n_{steps} n_l \sum_{i=1}^{n_h n_d} \Delta\epsilon_{MS,i} \tag{4.7}$$

To determine the anisotropic magnetostatic energy density (ΔE_{MS}) we then divide $\Delta\epsilon_{MS}$ by the volume of the sample.

$$V_{sample} = V_{dipole} n_h n_d n_l n_{steps} \tag{4.8}$$

The volume of a dipole (or atom), expressed in terms of the lattice constant, will depend on the crystal structure:

$$V_{dipole,fcc} = \frac{a^3}{4} \tag{4.9}$$

$$V_{dipole,bcc} = \frac{a^3}{2} \tag{4.10}$$

For a fcc vicinal film such as Co(11n), the anisotropic magnetostatic energy density is

$$\Delta E_{MS} = -\frac{\mu_o M_s^2}{32\pi} \left(\frac{1}{n_d n_h} \sum_{i=1}^{n_d n_h} \sum_{j=1} \left(\frac{3[(\hat{\mathbf{m}}_1 \cdot \mathbf{r}_{ij})^2 - (\hat{\mathbf{m}}_2 \cdot \mathbf{r}_{ij})^2]}{r_{ij}^5} \right) \right) \tag{4.11}$$

Note that $M_s = m/V_{dipole}$.

The results for a (1 1 13) film are plotted in Fig. 4-13 as a function of film thickness. The curve shown with the data is a fit given by

$$\Delta E_{MS,\parallel-\perp} = \left(-0.4 - \frac{2.7}{t} \right) \mathrm{x}10^5 \quad \mathrm{erg/cm^3}. \tag{4.12}$$

These results show that in a vicinal film, the shape alone leads to an in-plane anisotropy, and that it favors **M** parallel to the steps. For t greater than approximately 4 ML, this shape anisotropy is inversely proportional to the thickness. The magnitude of the magnetostatic anisotropy is relatively small; the surface term is an order of magnitude less than

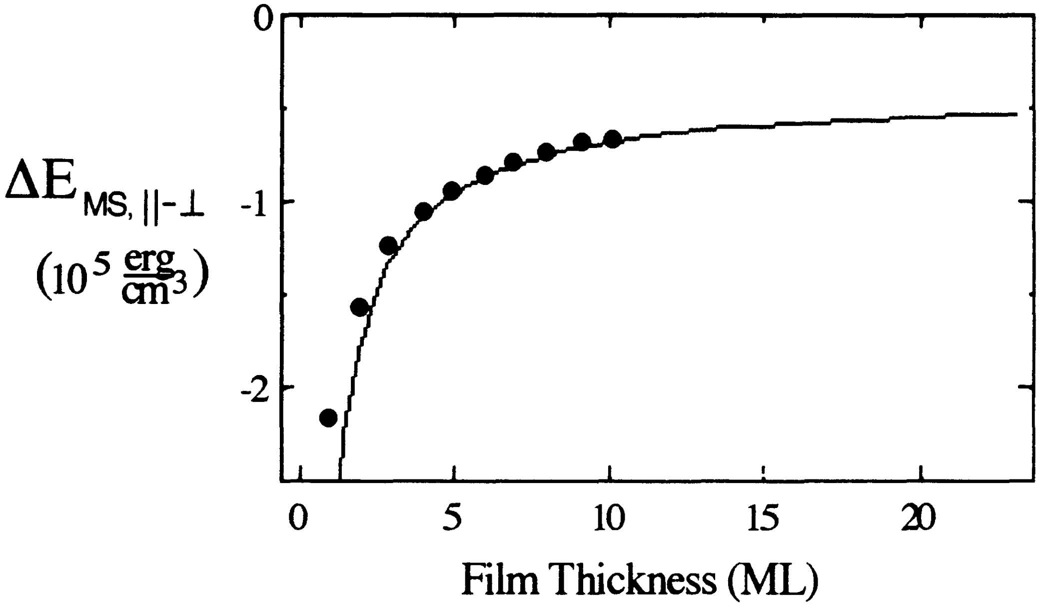

Figure 4-13: Results from discrete dipole calculation of the uniaxial in-plane magnetostatic anisotropy in a Co/Cu(1 1 13) film.

the anisotropy observed in Co/Cu(1 1 13) films. Thus, these calculations indicate that magnetostatic anisotropy is not a significant factor in the Co/Cu(11n) films.

4.1.6 Magnetoelastic Considerations

The final possible explanation of the uniaxial anisotropy which we consider is magnetoelasticity in vicinal films. Any step-induced anisotropic strain in the films will result in a magnetic anisotropy. Here we present a model of such effects in Co/Cu(11n). In the next section, we further examine the importance of magnetoelastic anisotropy by investigating the in-plane anisotropy of $Ni_{79}Fe_{21}/Cu(117)$.

The presence of terraces only three to seven atoms wide could allow vicinal films to relieve some of their misfit strain; and it is likely that this relaxation will not be isotropic. The step-edges most likely allow for a greater relaxation of the misfit strain perpendicular to the steps rather than parallel to them. The atoms at the step-edges are missing nearest neighbors perpendicular to the steps, and thus experience a deficiency in charge density that causes them to relax in towards the film [34, 33]. This relaxation relieves the tensile misfit strain.

Magnetoelastic Model

We now consider the magnetoelastic effects of an anisotropic strain in vicinal Co(11n) films. The strain tensor

$$e' = e_o \begin{pmatrix} 1-\delta & 0 & 0 \\ 0 & 1 & 0 \\ 0 & 0 & \frac{-\nu}{1-\nu}(2-\delta) \end{pmatrix} \tag{4.13}$$

describes the strain in an epitaxial film experiencing an in-plane biaxial misfit strain, e_o, which is relieved by a fraction δ along the **x'** direction; ν is Poisson's ratio. There is a corresponding contraction in the film along the **z'** axis. The **x'**, **y'**, and **z'** axes for the strain tensor are the crystal directions [110], [$\bar{1}$10], and [001], respectively; this is the step-coordinate system depicted in Fig. 4-11. The strain relief along the **x'** axis occurs perpendicular to the steps.

In order to use Eq. 2.4 to determine the magnetoelastic energy density of the film, we must rotate the strain tensor into the crystal coordinate system (**x**=[100], **y**=[010], and **z**=[001]). The rotated tensor is

$$e = \frac{e_o}{2} \begin{pmatrix} 2-\delta & -\delta & 0 \\ -\delta & 2-\delta & 0 \\ 0 & 0 & \frac{-2\nu}{1-\nu}(2-\delta) \end{pmatrix}, \tag{4.14}$$

and the corresponding magnetoelastic energy density (c.f. Eq. 2.4) is

$$E_{Magnetoelastic} = \frac{1}{2}(2-\delta)B_1 e_o - (2-\delta)B_1 e_o \cos^2\theta - \delta B_2 e_o \cos\phi \sin\phi \sin^2\theta \tag{4.15}$$

where θ and ϕ describe the orientation of **M** as shown in Fig. 4-11. The uniaxial magnetoelastic anisotropy in the (001) plane, $\Delta E_{||-\perp}$, is the difference in energy between magnetization parallel to the steps ($\theta = \pi/2, \phi = -\pi/4$), and magnetization perpendicular to the steps ($\theta = \pi/2, \phi = \pi/4$):

$$\Delta E_{||-\perp} = B_2 \delta e_o. \tag{4.16}$$

This anisotropy equation indicates that having the magnetization parallel to the steps is the low-energy configuration only if the product on the right side of the equation is negative. The misfit e_o in fcc Co/Cu(001) and (11n) films is positive; the Co lattice is stretched 1.9% by epitaxial growth on copper. The accepted *bulk* magnetoelastic parameter B_2 for fcc Co is also positive, 2.6×10^8 erg/cm^3. This value is extrapolated from data taken in fcc Co-Pd alloys [77]. Finally, as discussed above, we expect δ to be positive, it seems plausible that if there is any step-induced strain relief in the films, it will be perpendicular to the steps. Our analysis then indicates that if anisotropic strain is present in vicinal Co/Cu(11n) films, it should create an easy axis *perpendicular* to the steps; the value of $\Delta E_{||-\perp}$ is positive. This is not consistent with the experimental anisotropies presented here. There is a possibility that bulk B_2 does not apply in the ultrathin films, as discussed in Sec. 5.6 on page 87, but we have no other basis for the selection of B_2.

4.2 $Ni_{79}Fe_{21}$/Cu(117)

We studied the anisotropy in $Ni_{79}Fe_{21}$/Cu(117) films in order to further determine the importance of magnetoelastic anisotropy in vicinal films. The anisotropy constants K_1 and the magnetoelastic coupling coefficients B_1 and B_2 are very small in $Ni_{79}Fe_{21}$, as shown in Fig. 2-5. We therefore expect any magnetoelastic anisotropy to be much smaller in

Ni-Fe than in cobalt. However, anisotropy due to broken symmetry at the step-edges is also expected to be much smaller than in cobalt because of their different materials parameters K_1, B_1, and B_2. In chapter 5 we will demonstrate that the strength of this step-edge anisotropy depends on B_1 and B_2.

In Fig. 4-14 are the hysteresis loops taken for a 14 ML film of $Ni_{79}Fe_{21}/Cu(117)$ with the field applied a) parallel to the steps, and b) perpendicular to the steps. The easy axis coercivity of the film is approximately 20 Oe. This is consistent with coercivities measured in single-crystal $Ni_{80}Fe_{20}/Cu(001)$ by Hashim and Atwater [59]. There is a small step-induced anisotropy present in the Ni-Fe film which favors magnetization parallel to the steps. The strength of the anisotropy is approximately $\Delta E_{\|-\perp} = -1.5\text{x}10^4$ erg/cm^3, more than an order of magnitude smaller than that observed in the cobalt films on the same substrate. This anisotropy is consistent with anisotropy due to broken symmetry around the step-edges described in chapter 5, but we cannot rule out a magnetoelastic contribution to the anisotropy of the Ni-Fe vicinal film. We will further discuss the Ni-Fe in chapter 6.

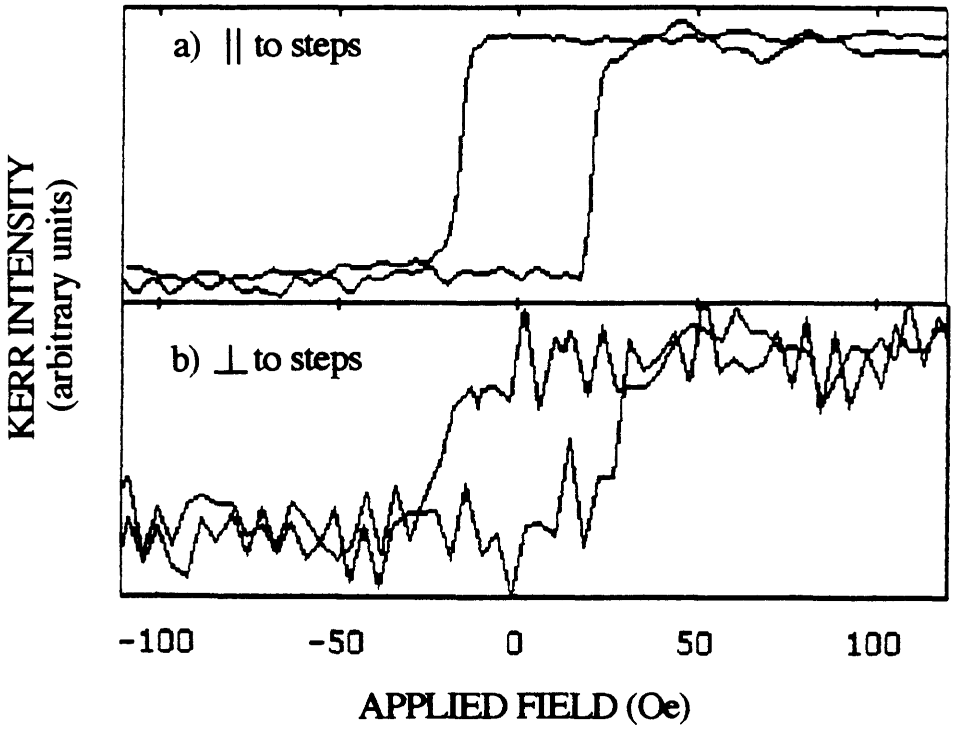

Figure 4-14: Hysteresis loops for a 14 ML $Ni_{79}Fe_{21}/Cu(117)$ film taken with the applied field a) parallel to the steps, and b) perpendicular to the steps.

Chapter 5

Pair-Interaction Model of Step-Induced Anisotropy

In chapter 4, experimental evidence was presented which indicates that the uniaxial anisotropy in the vicinal films is a surface step effect. As the thickness decreases, the surface and step-edge atoms occupy a larger fraction of the total film volume, and the anisotropy strengthens. Similarly, as the terrace width decreases, the step-edge atoms occupy a larger fraction of the total volume, and the anisotropy strengthens. As the temperature increases, thermally disordering the steps, the uniaxial anisotropy vanishes well below the Curie temperature. All of this evidence shows that step-edges are the source of the uniaxial anisotropy.

In this chapter, we model the anisotropy due to reduced local symmetry around the step-edge atoms. In section 5.1, a pair-interaction model previously used by Néel [1] to predict surface anisotropies is introduced, and modified to include the effects of strain in the film. Albrecht *et al.* have shown that the main aspects of the step-induced anisotropy in Fe/W stepped (110) can be explained by Néel's model [5]. Section 5.2 describes how we adapted the model to treat vicinal films, details the assumptions in our model, and gives the results for cubic materials. Sections 5.3 and 5.4 detail how the model applies to the vicinal systems Co(11n), Fe(01n), and Co/Cu(11n). Our model predicts the experimentally observed orientation of the easy axes in these systems, and gives reasonable agreement with the magnitude of the measured anisotropies. The chapter concludes with a discussion of some of the insights extracted from the model regarding the magnetic behavior of thin films, in general.

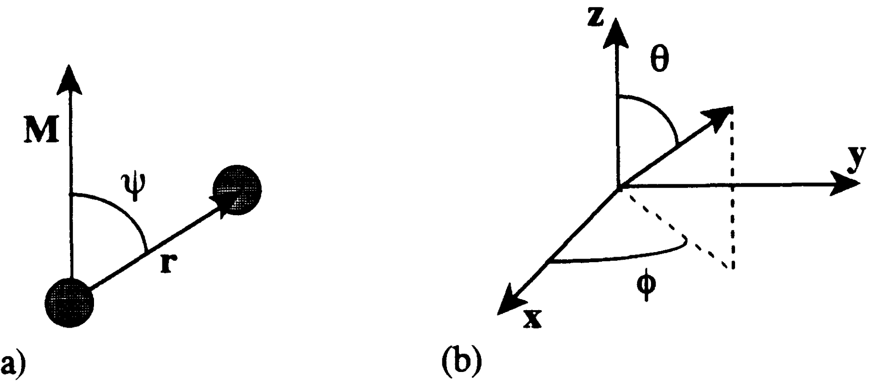

Figure 5-1: a) The angle ψ between $\mathbf{M}_s$ and the bond axis, $\mathbf{r}$. b) θ and ϕ, the angles used to define the direction of a vector (e.g. $\mathbf{M}_s$) with respect to the coordinate axes.

5.1 Néel's Surface Anisotropy Model

Néel proposed that atoms in an environment of reduced symmetry, such as those at a surface, will give rise to anisotropies that are different from the bulk anisotropy in the material . Néel applied the pair-interaction model developed by Van Vleck [14] to surfaces in order to model these anisotropies. The magnetic pair interaction energy between atoms is expanded in Legendre polynomials [1]:

$$w(r,\psi) = G(r) + L(r)(cos^2\psi - \frac{1}{3}) + Q(r)(cos^4\psi - \frac{6}{7}cos^2\psi - \frac{3}{35}) + \cdots \qquad (5.1)$$

This interaction depends on ψ, the angle between the bond axis and $\mathbf{M}_s$, and on the distance between the pair of atoms, r. (See Fig. 5-1a) The first term, which is independent of ψ, includes the spatially isotropic effects such as magnetic exchange ($E_{ex} = -J_{ij}\vec{S}_i \cdot \vec{S}_j$). It does not contribute to magnetic anisotropy. The second, dipolar term describes anisotropies which have a two-fold axis. The third, quadrupolar term describes anisotropy of cubic symmetry. We calculate the magnetic anisotropy energy of a film by summing this interaction energy w(r,ψ) for all pairs of atoms in the film.

Strain is present in ultrathin films for various reasons, such as surface relaxation [34] and film/substrate misfit [35]. Anisotropy due to strain is described via the Néel model by taking into account the strain-induced changes in r and ψ [10]. The coefficients of 5.1 are

Structure	K_1	B_1	B_2
simple cubic	$-2Q(r_o)$	$(\frac{dL}{dr})r_o$	$2L(r_o)$
bcc	$\frac{16}{9}Q(r_o)$	$\frac{8}{3}L(r_o)$	$\frac{8}{9}(L(r_o)+(\frac{dL}{dr})r_o)$
fcc	$Q(r_o)$	$3L(r_o)+\frac{1}{2}(\frac{dL}{dr})r_o$	$2L(r_o)+(\frac{dL}{dr})r_o$

Table 5.1: Relationships between bulk anisotropy constant K_1, bulk magnetoelastic constants B_1 and B_2, and pair-interaction coefficients $Q(r_o)$, $L(r_o)$, and $(dL/dr)r_o$.

functions of the distance r between the pairs of magnetic atoms, and can be expanded in terms of the bond strain

$$L_i(r) = L_i(r_o) + \frac{dL}{dr} \cdot \mathbf{e} \cdot r_o + \cdots \qquad (5.2)$$

where r_o is the bulk unstrained bond length. The subscript indicates the type of interaction being considered, (e.g. i = 1 denotes an interaction between first nearest neighbors, i = 2 denotes a second nearest neighbor interaction). For a given material, the values of $L_i(r_o)$ and $Q_i(r_o)$, as well as their variation with the bond length (e.g. $(dL_i/dr)\ r_o$) are related to the anisotropy constant K_1, and the magnetoelastic coefficients B_1 and B_2 of the bulk material, as shown in Table 5.1 [10]. Because we cannot separate first- and second-nearest neighbor effects in the definition of B_1 and B_2, and because the interaction strength should decrease with bond length, we assume that second-nearest neighbor interactions are relatively insignificant. The first term, G(r), also depends on **r**, and will no longer be spatially isotropic in the presence of an anisotropic strain; however, because it is independent of the orientation of **M** (i.e. it does not depend on ψ), it will not contribute to magnetic anisotropy.

We have calculated the Néel coefficients for fcc Co-Co interactions using K_1, B_1 and B_2 values extrapolated from the data of Fujiwara *et al.* taken at 4 K [77]. These coefficients are listed in Table 5.2 along with the coefficients for bcc Fe and fcc $Ni_{79}Fe_{21}$, as dictated by bulk magnetic parameters [78]. Recently, Suzuki *et al.* reported a room temperature

	K_1 10^6 erg/cm^3	$Q(r_o)$ 10^6 erg/cm^3	B_1 10^8 erg/cm^3	B_2 10^8 erg/cm^3	$L(r_o)$ 10^8 erg/cm^3	$(dL/dr)\ r_o$ 10^8 erg/cm^3
fcc Co	-1.2	-1.2	-1.6	2.6	-1.5	5.5
bcc Fe	0.47	0.26	-0.29	0.71	-0.11	0.91
fcc $Ni_{79}Fe_{21}$	-0.003	-0.003	-0.14	-0.018	-0.064	0.11

Table 5.2: Anisotropy constant K_1 and magnetoelastic coupling coefficients B_1 and B_2 for fcc Co (at 4 K), bcc Fe (at 298 K), and fcc $Ni_{79}Fe_{21}$ (at 298 K), and the Néel model parameters derived from them.

anisotropy constant, K_1 = -6.2x10^5 erg/cm^3, for ≈1000 Åfcc Co/Cu(001) films which is smaller than that given in Table 5.2. As seen in Table 5.2, the magnitude of $L(r_o)$ is two orders of magnitude larger than $Q(r_o)$; therefore, we neglect the quadrupole, and higher order terms of Eq. 5.1 in all cases where the dipole term contributes to the anisotropy. We have dropped the subscript i=1 on the Néel coefficients for convenience.

The Néel coefficients can alternatively be determined using first-principle calculations, as done by Victora and MacLaren [18]. The values of $L(r_o)$ and $(dL/dr)\ r_o$ given in Table 5.2 predict an $L(r)$ for Co-Co interactions at a bond separation r as found in Co/Pd multilayers [18] that is within 6% of the value obtained from the electronic structure calculations of Victora and MacLaren for that system.

We express the strain in the bonds around a given atom by a strain tensor given in the film coordinate system as described in Tables 5.3 - 5.5:

$$e = \begin{pmatrix} e_{xx} & e_{xy} & e_{xz} \\ e_{xy} & e_{yy} & e_{yz} \\ e_{xz} & e_{yz} & e_{zz} \end{pmatrix} \tag{5.3}$$

For the calculations presented here, we consider a biaxial strain that is uniform throughout the thickness of the film, such as that due to unrelieved misfit between the film and substrate. The misfit strain in the film has the form:

$$e = e_o \begin{pmatrix} 1 & 0 & 0 \\ 0 & 1 & 0 \\ 0 & 0 & \frac{-2\nu}{1-\nu} \end{pmatrix} \tag{5.4}$$

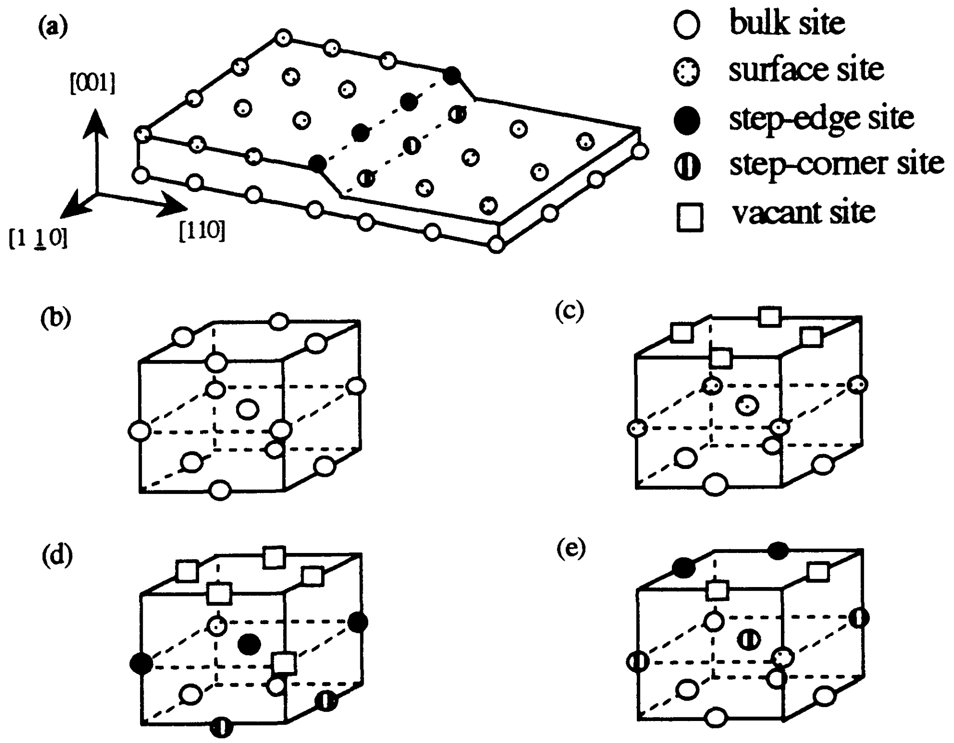

Figure 5-2: a) Region around a surface step in fcc (11n) films, sites of different symmetry are indicated. Nearest neighbor clusters are shown for b) bulk sites, c) surface sites, d) step-edge sites, and e) step-corner sites.

e_o is the misfit as defined in section 2.1, and ν is Poisson's ratio.

5.2 Néel's Model Applied to (11n) Vicinal Films

For (11n) vicinal films we identify four distinct types of atomic sites in the film, which are indicated in Figure 5-2a: bulk, surface, step-edge, and step-corner sites. Atoms at each type of site are in environments of different symmetry, and contribute in different ways to the total magnetic anisotropy. Bulk fcc atoms have twelve nearest neighbors, as shown in Figure 5-2b. The symmetry of a surface site is reduced compared to that of the bulk because four nearest neighbor bonds are broken in the creation of the surface. These bonds are along $[011]$, $[0\bar{1}1]$, $[101]$, and $[\bar{1}01]$ directions. The resulting nearest-neighbor cluster around a surface atom contains only eight atoms (Fig. 5-2c).

In creating the surface steps parallel to $[1\bar{1}0]$ in (11n), three additional bonds are broken. One of these is between the atom at the upper edge of the step and its nearest neighbor in the [110] direction; leaving the edge-site atom with only seven nearest neighbors (Fig. 5-2d). The other two broken bonds are associated with atoms formerly in bulk sites, but now at the corner of the step. These bonds are along [101] and [001] directions. The corner-site atom is left with ten nearest neighbors (Fig. 5-2e).

The anisotropy contributions of each of the reduced symmetry sites (e.g. surface, and step sites) can be determined in either of two ways. We can sum the energies of the bonds present in the nearest-neighbor clusters, or alternatively, we can sum the energies of the broken bonds and subtract this sum from the anisotropy of a bulk cluster. Both methods lead to the same result for the magnetic anisotropy of the entire film. We use the latter. The anisotropy energy density for the film is then given by

$$E_{film} = E_{bulk} - 2\frac{E_{surface}}{t} - 2\frac{(E_{step-edge} + E_{step-corner})}{t\,d} \tag{5.5}$$

where E_{bulk}, $E_{surface}$, $E_{step-edge}$, and $E_{step-corner}$ are in units of energy/volume, energy/area, energy/length, and energy/length, respectively. t and d are the film thickness and the terrace width, respectively. (See Appendix A for a derivation of Eq. 5.5) Eq. 5.5 indicates, as expected, that as the film thickness increases, anisotropy effect from the surface and steps will become less important. Similarly, in systems with wider terraces, step effects will not be as significant.

Assumptions in the Model

To clearly judge where this pair-interaction model can reasonably predict magnetic anisotropy behavior, we point out the assumptions inherent to the model as presented here and discuss how these assumptions affect our results regarding Co/Cu(11n). The model assumes structurally perfect films: only sharp interfaces and straight steps are considered. This assumption will cause predicted anisotropies to be too large if the surface steps are thermally roughened. There will also be discrepancies if there is interdiffusion between the film and substrate. In the Co/Cu vicinal to (001) system, below temperatures of 460 K interdiffusion is insignificant [54]. However, thermal roughening of the steps does occur at temperatures only slightly above room temperature [63]. Recently, significant changes in the anisotropy as a function of temperature [71] in Co/Cu(1 1 17) have been attributed to thermal roughening of the steps. Because such roughening is neglected, the results of the model are more appropriate for low-temperature anisotropies.

The model also assumes that the strain in the film can be described by Eq. 5.4. Any surface relaxations strains, or thickness dependent strains are neglected. In thin transition-metal films it is known that surface atoms, and step-edge atoms relax slightly in toward the bulk of the film [34, 33]. This relaxation arises because atoms at a free surface have lost nearest neighbors and experience a deficiency in electron density. The bulk atomic positions do not necessarily minimize the free energy at the surface, resulting in expansion [34], or more typically for transition metals, contraction of the first interplanar spacing [34, 79, 80]. Experimentally, the lattice strain due to mismatch is found to be homogeneous and constant in Co/Cu(001) films 5 to 10 ML thick [56]; therefore, assuming an average strain given by Eq. 5.4 is reasonable for the Co/Cu system.

As mentioned in Sec. 5.1, the model assumes only nearest-neighbor interactions. This assumption was made because we have no way of separating nearest and next-nearest effects in the definition of the magnetoelastic coupling coefficients, and thus in the Néel model's interaction parameters. In fcc Co/Pd multilayers, results considering only nearest neighbors agree well with first-principle calculations [18]. We therefore feel justified in making this assumption for the Co/Cu(11n) films.

Two final considerations involve magnetic interactions between atoms. First, the model only predicts what are basically magnetocrystalline and magnetoelastic energies; it does not account for other magnetic energies such as isotropic exchange. The exchange force is responsible for parallel alignment of neighboring spins in a ferromagnet. A strong surface anisotropy will cause spins of surface atoms to orient in a given direction (the surface easy axis), and through exchange forces these surface spins can pin, or influence the orientation of spins well into the material if the bulk anisotropy is relatively weak. The distances over which this pinning occurs is approximately the width of a domain wall, a few hundred angstroms (Å), if the surface and bulk anisotropies both favor **M** in the plane of the film, as in fcc Co. If the surface favors out-of-plane magnetization, the pinning is important over a much smaller thickness (30-40 Å) [81]. The results of the model must be considered in context with magnetic exchange between the bulk and surface atoms. Neglecting this consideration may lead to an underestimation of the thicknesses for which surface effects dominate the behavior of the film.

Secondly, applying the pair-interaction model to vicinal films using Eq. 5.5 assumes that the two interfaces of the vicinal film are magnetically identical, as mentioned in Appendix A. By using Eq. 5.5, we neglect the fact that although the Co does not polarize the Cu at the interface, the Cu may reduce the moment of the Co. If such a proximity effect occurs, the interaction parameters $L(r_o)$ and $(dL/dr)r_o$ used for atoms at the film/substrate interface must be modified. For systems such as Co/Pd [18], in which the film does polarize substrate atoms, this magnetic interaction results in a film/substrate interface anisotropy quite different from the vacuum/film interface anisotropy, and cannot be neglected. To demonstrate the effect of this assumption, we will first treat an isolated Co(11n) film (Sec. 5.3), and then model a Co/Cu(11n) film by including the appropriate Co-Cu interaction parameter for the film/substrate interface (Sec. 5.5).

Calculated Energies for Cubic Materials

We have used the Néel model to calculate the anisotropy energies E_{bulk} and $E_{surface}$ for simple (i.e. primitive) (sc), body-centered (bcc), and face-centered (fcc) cubic structures with low-index surfaces, as well as $E_{step-edge}$, and $E_{step-corner}$ for fcc(001) and bcc(001) vicinal surfaces. In order to obtain these results, we incorporated the model described in Sections 5.1 and 5.2 in a Mathematica^{TM} program (see Appendix B) with which we can calculate and plot $E(\theta, \phi)$ for any cluster of atoms in the presence of any strain described by Eq. 5.3. The expressions for anisotropy energies in (001), (110) and (111) systems are given in Tables 5.3, 5.4, and 5.5, respectively, using a biaxial strain (Eq. 5.4) with $\nu=1/3$. Upon summation of the interaction energy over nearest neighbors, the angle ψ has been written in terms of θ and ϕ (Fig. 5-1). The surface and bulk anisotropy energies in the tables correspond to those calculated by Victora and MacLaren [18] for the *unstrained* case ($e_o=0$) upon an appropriate rotation of the coordinate system. We present each energy in a coordinate system in which $\mathbf{z}$ is along the surface normal, as described in the tables.

5.3 Anisotropy in *fcc* Co(11n)

This section illustrates the calculated results for the strained Néel anisotropy in a fcc Co(11n) film strained by the 1.9% misfit between Co and Cu (Eqn. 5.4). For each type of atomic site described in Section 5.2, we show the anisotropy energy surface, and a representation of the cross-sections of this surface for the (001) and (1 1 13) planes. These

(001) System	Anisotropy Energy $\mathbf{x} = [100], \mathbf{y} = [010], \mathbf{z} = [001]$
Bulk, unstrained	$\mathrm{E}_{bulk}^{unstrained} = \mathrm{E}_{MC} \quad (erg/cm^3)$
Simple cubic (sc)	$\frac{-Q(r_o)}{2}(\sin^2 2\theta + \sin^2 2\phi \sin^4 \theta)$
Body-centered cubic (bcc)	$\frac{4Q(r_o)}{9}(\sin^2 2\theta + \sin^2 2\phi \sin^4 \theta)$
Face-centered cubic (fcc)	$\frac{Q(r_o)}{4}(\sin^2 2\theta + \sin^2 2\phi \sin^4 \theta)$
Bulk, strained	$\mathrm{E}_{bulk}^{strained} = -2B_1 e_o \cos^2 \theta \quad (erg/cm^3)$
sc	$-2e_o \frac{dL}{dr} r_o \cos^2 \theta$
bcc	$-\frac{16}{3} e_o L(r_o) \cos^2 \theta$
fcc	$-(6e_o L(r_o) + e_o \frac{dL}{dr} r_o) \cos^2 \theta$
Surface	$\frac{1}{h}\mathrm{E}_{surface} \quad (erg/cm^3)$
sc(001)	$\frac{1}{2}(e_o \frac{dL}{dr} r_o + L(r_o)) \cos^2 \theta$
bcc(001)	$-\frac{8}{3} L(r_o) e_o \cos^2 \theta$
fcc(001)	$(\frac{1}{2} L(r_o) - 3e_o L(r_o)) \cos^2 \theta$
Step	$\frac{1}{wh}\mathrm{E}_{step} \quad (erg/cm^3)$
bcc(001) with steps ∥ [100]	
$\mathrm{E}_{step-edge}$	0
$\mathrm{E}_{step-corner}$	$-\frac{4}{3} L(r_o) e_o \cos^2 \theta + (\frac{2}{3} L(r_o) - \frac{4}{9} e_o L(r_o) + \frac{2}{9} e_o \frac{dL}{dr} r_o) \sin \phi \cos \theta \sin \theta$
fcc(001) with steps ∥ $[1\bar{1}0]$	
$\mathrm{E}_{step-edge}$	$-\frac{1}{4}(L(r_o) + e_o \frac{dL}{dr} r_o) \cos^2 \theta + \frac{1}{2}(L(r_o) + e_o \frac{dL}{dr} r_o) \sin \phi \cos \phi \sin^2 \theta$
$\mathrm{E}_{step-corner}$	$(\frac{1}{4} L(r_o) - \frac{3}{2} e_o L(r_o)) \cos^2 \theta + \frac{1}{2} L(r_o) \cos \theta \sin \theta (\sin \phi + \cos \phi)$

Table 5.3: Bulk, (001) surface, and step anisotropy energies for cubic structures in the (001) surface coordinate system: x=[100], y=[010], z=[001]. As in Appendix A, h and w are the height of a monolayer and the distance between terrace atoms, respectively.

(110) System	**Anisotropy Energy** $\mathbf{x} = [1\bar{1}0], \mathbf{y} = [00\bar{1}], \mathbf{z} = [110]$
Bulk, strained	$\mathrm{E}_{bulk}^{strained} = -(B_1 + B_2)e_o \cos^2\theta + (B_2 - B_1)e_o \cos^2\phi \sin^2\theta \quad (erg/cm^3)$
sc	$-(2L(r_o) + \frac{dL}{dr} r_o)e_o \cos^2\theta + (2L(r_o) - \frac{dL}{dr} r_o)e_o \cos^2\phi \sin^2\theta$
bcc	$-(\frac{32}{9} L(r_o) + \frac{8}{9}\frac{dL}{dr} r_o)e_o \cos^2\theta + (-\frac{16}{9} L(r_o) + \frac{8}{9}\frac{dL}{dr} r_o)e_o \cos^2\phi \sin^2\theta$
fcc	$-(5L(r_o) + \frac{3}{2}\frac{dL}{dr} r_o)e_o \cos^2\theta + (-L(r_o) + \frac{1}{2}\frac{dL}{dr} r_o)e_o \cos^2\phi \sin^2\theta$
Surface	$\frac{1}{h}\mathrm{E}_{surface} \quad (erg/cm^3)$
sc(110)	$(\frac{1}{2} L(r_o) - e_o L(r_o)) \cos^2\theta + (\frac{1}{2} L(r_o) + e_o L(r_o)) \cos^2\phi \sin^2\theta$
bcc(110)	$(\frac{1}{3} L(r_o) - \frac{16}{9} e_o L(r_o) - \frac{1}{9} e_o \frac{dL}{dr} r_o) \cos^2\theta - (\frac{1}{3} L(r_o) + \frac{8}{9} e_o L(r_o) - \frac{1}{9}\frac{dL}{dr} r_o) \cos^2\phi \sin^2\theta$
fcc(110)	$(\frac{1}{2} L(r_o) - \frac{5}{2} e_o L(r_o) - \frac{5}{4} e_o \frac{dL}{dr} r_o) \cos^2\theta - (\frac{1}{2} L(r_o) + \frac{1}{2} e_o L(r_o) + \frac{1}{4}\frac{dL}{dr} r_o) \cos^2\phi \sin^2\theta$

Table 5.4: **Bulk**, (110) surface, and step anisotropy energies for cubic structures in the (110) surface coordinate system: x=$[1\bar{1}0]$, y=$[00\bar{1}]$, z=$[110]$. h is the height of a monolayer in cm.

(111) System	Anisotropy Energy $\mathbf{x} = [11\bar{2}], \mathbf{y} = [\bar{1}10], \mathbf{z} = [111]$
Bulk, strained	$\mathrm{E}_{bulk}^{strained} = -2B_2 e_o cos^2\theta \quad (erg/cm^3)$
sc	$-4e_o L(r_o) \cos^2\theta$
bcc	$-\frac{16}{9}(L(r_o) + \frac{dL}{dr} r_o) e_o \cos^2\theta$
fcc	$-(4L(r_o) + 2\frac{dL}{dr} r_o) e_o \cos^2\theta$
Surface	$\frac{1}{h}\mathrm{E}_{surface} \quad (erg/cm^3)$
sc(111)	$-2e_o L(r_o) \cos^2\theta$
bcc(111)	$(\frac{1}{2}L(r_o) - \frac{8}{9}e_o L(r_o) - \frac{25}{18}e_o \frac{dL}{dr} r_o) \cos^2\theta$
fcc(111)	$(\frac{3}{4}L(r_o) - 2e_o L(r_o) - \frac{1}{4}e_o \frac{dL}{dr} r_o) \cos^2\theta$

Table 5.5: **Bulk, (111) surface, and step anisotropy energies for cubic structures in the (111) surface coordinate system: x=[11$\bar{2}$], y=[$\bar{1}$10], z=[111]. h is the height of a monolayer in cm.**

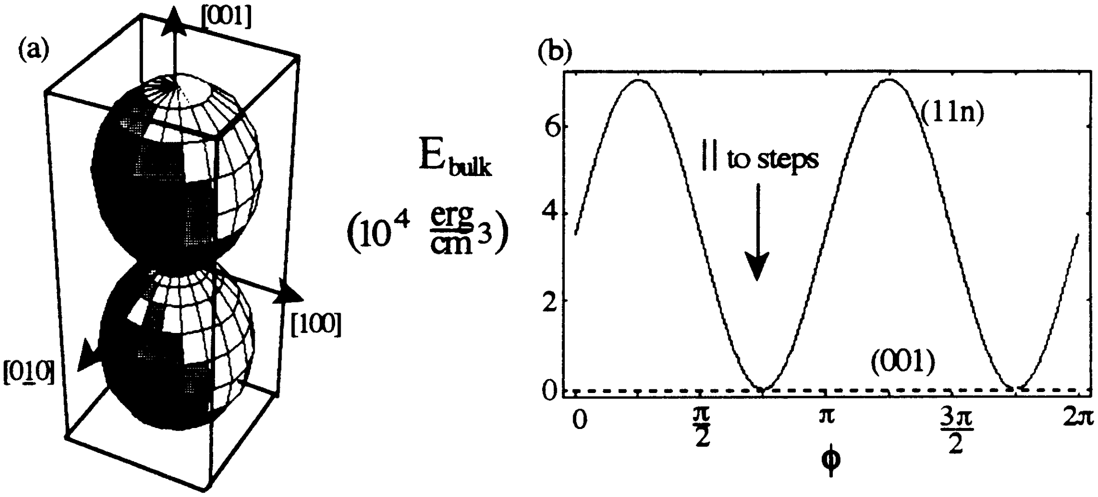

Figure 5-3: a) Anisotropy energy surface for a bulk site in a fcc Co(11n) film. b) In-plane anisotropy for (001) and (1 1 13) planes through this energy surface. (001) anisotropy is shown as a dotted line, (1 1 13) anisotropy as a solid line. The surface steps are along $[1\bar{1}0]$, defined by $\phi = 3\pi/4, 7\pi/4$.

cross-sections depict the in-plane anisotropy due to each particular site. Because of magnetostatic considerations in ultrathin vicinal films, **M** is expected to be in the (001) plane; experimentally only in-plane magnetization has been observed in Co/Cu(11n) films. A measure of the in-plane uniaxial anisotropy, $\Delta E_{\|-\perp}$, is defined as the energy difference between **M** parallel to the steps ($\phi = -\pi/4$) and **M** perpendicular to the steps ($\phi = \pi/4$). The negative of the surface and step-site contributions to the anisotropy is displayed so that a minimum in the site energy surfaces corresponds to a minimum for that site's contribution to the total film anisotropy energy as described by Eq. 5.5. Note that only the dipole effects are shown below, but the bulk quadrupole, or magnetocrystalline anisotropy effects are included when considering the total anisotropy of the film.

The anisotropy contribution due to the strained bulk is shown in Fig. 5-3a, with the anisotropy in (001) and (1 1 13) plane cross-sections of this surface in Fig. 5-3b. In the (001) surface, as shown with the dotted lines, the energy is constant and there is no in-plane anisotropy. Upon rotation into the (1 1 13) plane, the surface is no longer perpendicular to a high symmetry axis of the energy surface. This reduction in symmetry results in uniaxial in-plane anisotropy with the $[1\bar{1}0]$ direction parallel to the steps ($\phi = 3\pi/4$) being easier than the step normal ($\Delta E_{\|-\perp,bulk}$=-7x10^4 erg/cm^3$\approx$-5x10^{-7} eV/atom).

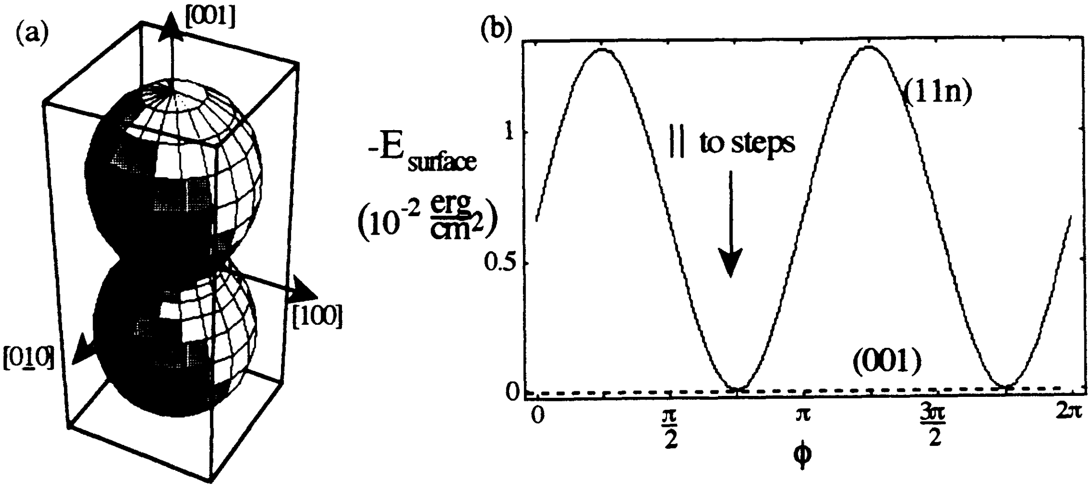

Figure 5-4: a) Anisotropy energy surface for a surface site in a fcc Co(11n) film. b) In-plane anisotropy for (001) and (1 1 13) planes through this energy surface. (001) anisotropy is shown as a dotted line, (1 1 13) anisotropy as a solid line. The surface steps are along $[1\bar{1}0]$, defined by $\phi = 3\pi/4, 7\pi/4$.

The anisotropy energy corresponding to bonds broken to create the surface is shown in Fig. 5-4. This contribution also favors **M** in the plane of the film, reinforcing the effects of magnetostatic energy and the bulk anisotropy contribution in the strained film. The (001) cross-section of this energy surface reveals that there is no (001) in-plane anisotropy associated with surface sites. For **M** confined to the (1 1 13) plane, however, the surface anisotropy contribution favors magnetization parallel to the steps ($\Delta E_{\|-\perp,surface}$= -0.013 erg/cm^2$\approx$-5x10^{-6} eV/atom).

The contribution from the step-edge site is shown in Fig. 5-5. The anisotropy due to this site favors **M** in the $(1\bar{1}0)$ plane, which is parallel to the steps. The reduced symmetry at this site contributes a strong uniaxial in-plane anisotropy when **M** is confined in either the (001) or (1 1 13) plane. This energy difference $\Delta E_{\|-\perp,step-edge}$ in both of these planes is quite large, approximately -2.9x10^{-8} erg/cm (-7x10^{-5} eV/atom) favoring magnetization parallel to the steps.

The step-corner site contributes the anisotropy energy illustrated in Fig. 5-6. The (001) cross-section of this surface reveals that there is no in-plane magnetic anisotropy due to this site. In the (1 1 13) plane, however, **M** perpendicular to the steps is favored by $\Delta E_{\|-\perp,step-corner}$ = 0.47x10^{-8} erg/cm = 1x10^{-5} eV/atom. As seen by comparing Fig. 5-5

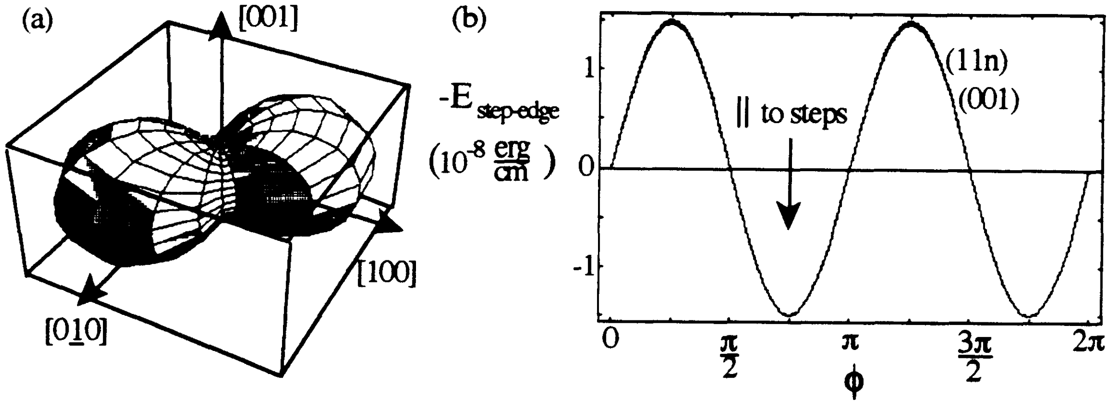

Figure 5-5: a) Anisotropy energy surface for a step-edge site in a fcc Co(11n) film. b) In-plane anisotropy for (001) and (1 1 13) planes through this energy surface. (001) anisotropy is shown as a dotted line, (1 1 13) anisotropy as a solid line. The surface steps are along $[1\bar{1}0]$, defined by $\phi = 3\pi/4, 7\pi/4$.

and Fig. 5-6, the two step-site contributions counteract one another in the (1 1 13) plane, but the much stronger step-edge effect dominates giving a combined step effect which always favors **M** parallel to the steps for Co(11n) with $\Delta E_{\|-\perp,step}$ = -2.4x10^{-8} erg/cm = -6x10^{-5} eV/atom.

The Néel anisotropy of the film is obtained by substituting the four contributions described above into Eq. 5.5. In Co(1 1 13) films, the energy difference is given by

$$\Delta E_{\|-\perp,film} = \left(-0.7 - \frac{190}{t_{ML}}\right) \mathrm{x}\, 10^5 \qquad \mathrm{erg/cm^3} \qquad (5.6)$$

where t_{ML} is the thickness of the film in monolayers. Magnetization parallel to the steps is always favored ($E_{\|-\perp,film} < 0$), but the magnitude of $E_{\|-\perp,film}$ decreases with increasing film thickness, as shown in Fig. 5-7. Even for $t_{ML} \to \infty$ there is a weak uniaxial anisotropy parallel to the steps in an fcc film on a (11n) vicinal surface if **M** lies in the (11n) plane.

Our model predicts that while very thin films should show strong uniaxial anisotropy, the anisotropy of thicker Co/Cu(11n) films will approach the biaxial in-plane anisotropy found in Co/Cu(001). This transition from uniaxial to biaxial behavior occurs because the effects of the steps weaken as film thickness increases, as described in Eq. 5.5. We use $d^2E/d\phi^2$, the curvature of the in-plane anisotropy energy, evaluated at $\phi = \pi/4$ (perpendicular to the steps), to characterize this transition. As shown in Fig. 5-8, for Co/Cu(1 1 13) films thinner

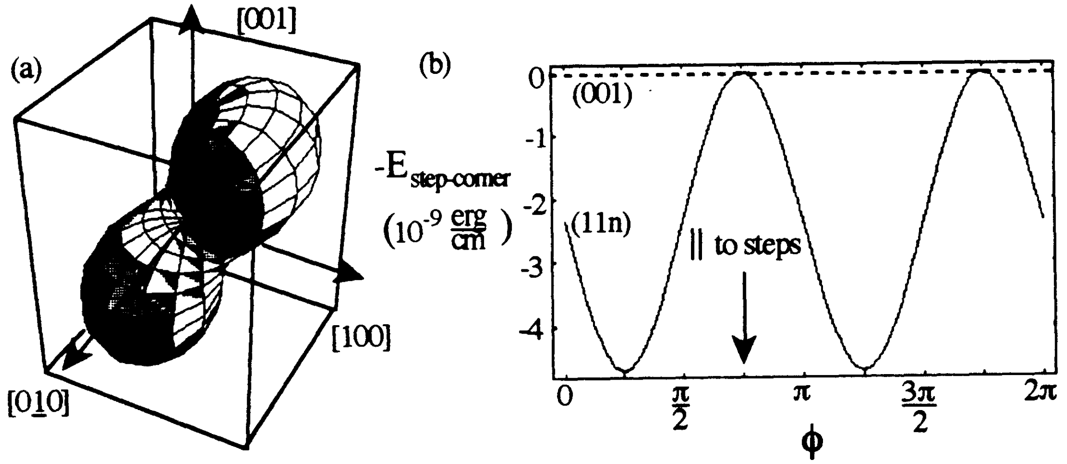

Figure 5-6: a) Anisotropy energy surface for a step-corner site in a fcc Co(11n) film. b) In-plane anisotropy for (001) and (1 1 13) planes through this energy surface. (001) anisotropy is shown as a dotted line, (1 1 13) anisotropy as a solid line. The surface steps are along $[1\bar{1}0]$, defined by $\phi = 3\pi/4, 7\pi/4$.

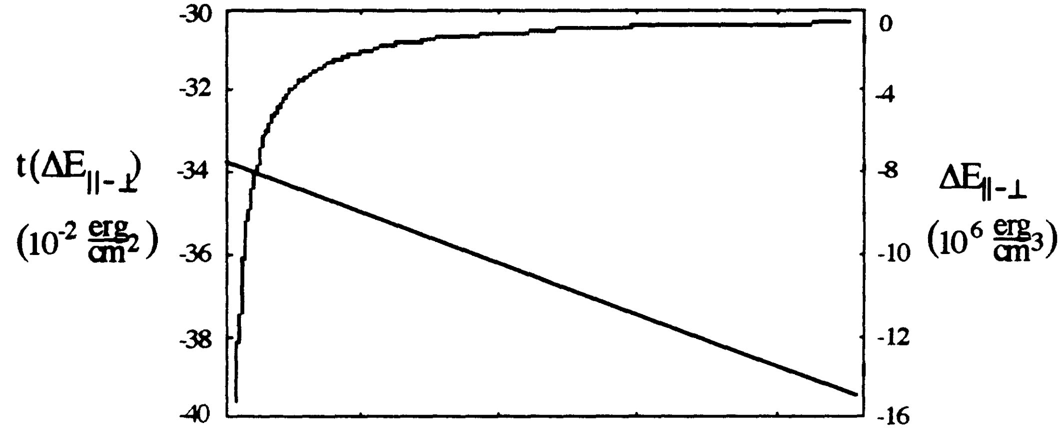

Figure 5-7: Calculated strength of the uniaxial anisotropy in Co(1 1 13) films as a function of film thickness. The straight line is the anisotropy energy times the film thickness (left scale), while the curve is the anisotropy energy (right scale).

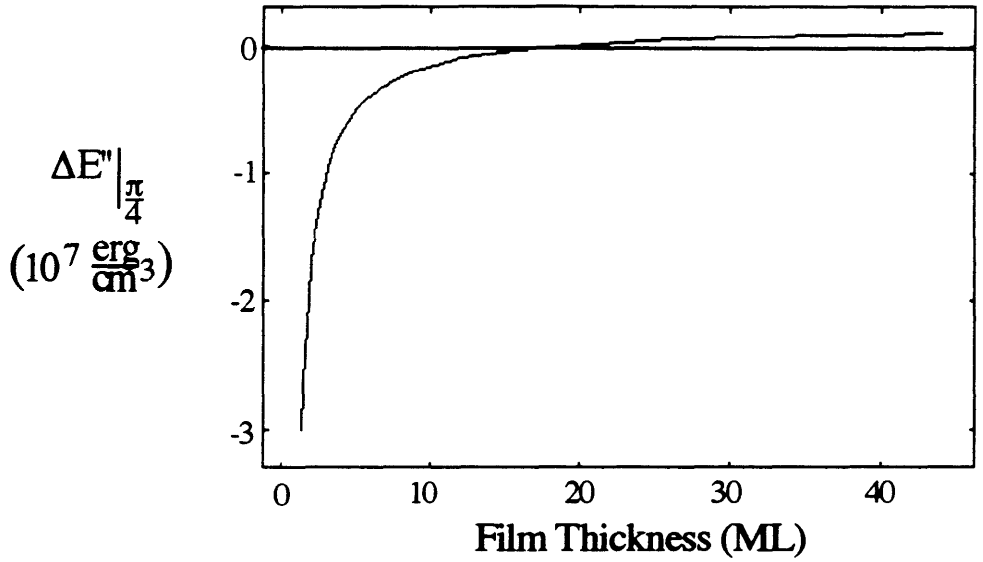

Figure 5-8: The calculated transition from uniaxial to biaxial anisotropy with increasing film thickness in Co/Cu(1 1 13) films. Δ E" is $d^2E/d\phi^2$ and has been evaluated at $\phi = \pi/4$, the direction perpendicular to the steps.

than 17 monolayers, this curvature is negative indicating that the direction perpendicular to the steps is a hard axis. For thicknesses greater than 17 ML, the curvature is positive, and the direction perpendicular to the steps is a local minimum for the in-plane anisotropy energy. We note, however, that for **M** in the (1 1 13) plane, parallel to the steps remains the global minimum, as previously indicated in Fig. 5-7.

5.4 Anisotropy in *bcc* Fe(01n)

We have also applied our model to bcc Fe/W vicinal to (001) which was studied experimentally by Chen and Erskine [4]. The normal to their vicinal surface is 4° from the [001] direction toward [010] making the Miller indices of the surface (01n) where n is 1/tan(4°), or approximately (0 1 14). This vicinal W surface is characterized by 2.5 nm wide (001) terraces separated by atomic steps parallel to [100], and the lattice mismatch between bcc Fe (a_{Fe} = 0.2866 nm) and W (a_W = 0.3165 nm) is 9.4%. Fe films grown on such a surface are magnetized in-plane with an easy axis *perpendicular* to the steps for thicknesses between 1 and 2.5 ML [4].

As in Co(11n) films, the Fe vicinal to (001) films contain four types of atomic sites: bulk, surface, step-edge, and step-corner. In this system, however, if only nearest neighbors are

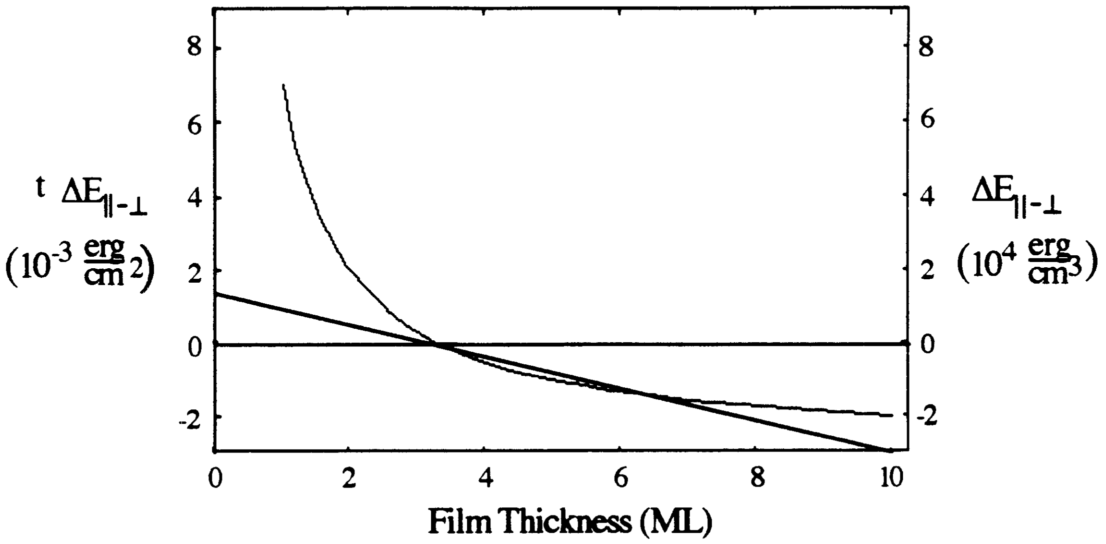

Figure 5-9: Calculated strength of the uniaxial anisotropy in Fe(0 1 14) films as a function of film thickness. The straight line is the anisotropy energy times the film thickness (left scale), while the curve is the anisotropy energy (right scale). At 3.5 ML of Fe, the easy axis changes from perpendicular to the steps to parallel to the steps.

considered, the surface and step-edge atoms have the same nearest-neighbor coordination, the number of bonds in these two sites is the same. Therefore, the step-edge atoms do not contribute to the anisotropy, as indicated in Table 5.3. A thorough examination of each site's contribution to the anisotropy can be found in Ref. [82].

The in-plane uniaxial anisotropy predicted by the Néel model for Fe(0 1 14) is

$$\Delta E_{\|-\perp,film} = \left(-0.3 + \frac{1.0}{t_{ML}}\right) \mathrm{x}\, 10^5 \qquad \mathrm{erg/cm^3}. \tag{5.7}$$

The bulk contribution to this anisotropy is negative, as indicated in the first term of equation 5.7, while the surface and step contributions are positive. Because these contributions are of opposite sign, there is a thickness at which the easy axis is predicted to switch from perpendicular to the steps, to parallel to the steps. This thickness, as can be seen from the plot of Eq. 5.7 in Fig. 5-9, is approximately 3.5 monolayers of Fe. As mentioned above, experimentally the anisotropy is observed to be positive below a thickness of 2.5 ML. The Néel model is successful in predicting the observed easy axis in this thickness range. No experimental results are available for thicker epitaxial films of Fe/W(01n).

Comparison of *fcc* Co(11n) and *bcc* Fe(01n)

By comparing the results for Co(11n) and Fe(01n) vicinal systems, we can investigate what differences between the systems give rise to an easy axis *parallel* to the steps in the former case, and an easy axis *perpendicular* to the steps in the latter. The features that might give rise to such a difference include crystal structure, magnitude and sign of the misfit strain, and magnitudes and signs of the Néel model coefficients. We considered both materials to have positive misfit strains, putting them in biaxial tension in the plane. The misfit in the Fe was larger than that in the Co (9.4% vs 1.9%), but this difference does not significantly affect the in-plane anisotropy. The Néel coefficients in fcc Co and bcc Fe have the same signs: $L(r_o)$ is negative, and $(dL/dr)r_o$ is positive. The reason for the different easy axes is not to be found in these materials parameters. The most significant difference between the two films is merely the crystal structure. The Co is fcc, while the Fe is bcc. The different symmetry around the surface and step sites in fcc Co(11n) and bcc Fe(01n) is the reason that in the Fe the easy axis is perpendicular to the steps and in Co it is parallel.

A further difference between Co(11n) and Fe(01n) films indicated from the results of the model is the plane in which the magnetization must lie in order to produce the observed uniaxial anisotropies. As seen in Sec. 5.3, uniaxial anisotropy is predicted for Co(11n) regardless of whether the magnetization is confined to the (001) terrace plane, or the (11n) film plane. The step-edge anisotropy is equally strong in either case (Fig. 5-5). In the Fe/W(01n) films, however, the magnetization must lie in the (01n) plane for there to be any uniaxial anisotropy in the films, according to the model [82]. If **M** is in the (001) plane in Fe/W(01n) vicinal films, the anisotropy remains four-fold, as observed in flat Fe/W(001) films.

5.5 Anisotropy in *fcc* Co/Cu(11n)

By referring to work in the literature regarding Cu/Co/Cu(1 1 13) films [70], and the strain in Co/Cu(001) films [56], we are able to more appropriately model the anisotropy in our Co/Cu(11n) films than we did in Sec. 5.3. These results allow us to separate the effects of a Co/vacuum interface from those of a Co/Cu interface. Krams *et al.* have determined the in-plane and out-of-plane anisotropies for Cu/Co/Cu(1 1 13) films [70]. The overall anisotropy of the films studied (4-14 ML thick) is uniaxial in-plane, with an easy axis parallel to the steps. However, the uniaxial anisotropy weakens as the film thickness decreases indicating that the interface anisotropy favors magnetization perpendicular to the steps. Their Co films have two identical interfaces, and their thickness-dependent, interface anisotropy is clearly representative of the Co-Cu interaction. We compare our modified pair-interaction model calculation with their data in order to deduce $L(r_o)$ and $(dL/dr)r_o$ for Co-Cu interactions.

In order to include interfacial anisotropies in the model, and thus be able to treat Cu/Co/Cu films, we must use Eq. 5.8 instead of Eq. 5.5, which was appropriate for isolated films (i.e. vacuum/Co/vacuum).

$$\begin{aligned} E_{film} &= E_{bulk} - 2\frac{E_{surface} - E^{interface}_{surface}}{t} \\ &\quad -2\frac{(E_{step-edge} - E^{interface}_{step-edge}) + (E_{step-corner} - E^{interface}_{step-corner})}{t\,d} \end{aligned} \qquad (5.8)$$

E_{bulk}, $E_{surface}$, $E_{step-edge}$, and $E_{step-corner}$ are, as before, the expressions in Table 5.3 with the $L(r_o)$ and $(dL/dr)r_o$ values for Co-Co interactions (Table 5.2). $E^{interface}_{surface}$, $E^{interface}_{step-edge}$, and $E^{interface}_{step-corner}$ are the expressions in Table 5.3 using $L(r_o)$ and $(dL/dr)r_o$ for Co-Cu interactions at an interface. Comparing the in-plane and out-of-plane anisotropies predicted by Eq. 5.8 with the anisotropies measured in Cu/Co/Cu(1 1 13) by Krams *et al.*, we obtain $L(r_o)$ and $(dL/dr)r_o$ values for Co-Cu of -1.5×10^8 erg/cm^3 and 2.3×10^8 erg/cm^3, respectively.

Using the Co-Cu interaction parameters obtained from the results of Krams *et al.*, we can now treat our Co/Cu(11n) films as having one Co/vacuum interface (or surface) in which we assume $L(r_o)$ is zero between an Co atom and a vacant site, and a Co/Cu interface characterized by the appropriate Co-Cu interaction parameters. For the Co-Co interactions in the film, we continue to assume the interaction parameters derived from bulk properties listed in Table 5.2. In addition to improving our model of the anisotropy by treating the interfaces individually, we also now use the experimentally determined average strain tensor for Co/Cu(001) films thicker than 5 ML [56]. This strain tensor is Eq. 5.4 with a value of $\nu = 0.37$. Including the Co/Cu interface anisotropy, the appropriate strain tensor, and the magnetostatic anisotropy for a vicinal Co film, the uniaxial anisotropy calculated for Co/Cu(1 1 13) films for **M** in the (001) plane is

$$\Delta E_{\|-\perp,film} = \left(-0.4 - \frac{103}{t_{ML}}\right) \times 10^5 \qquad \mathrm{erg/cm^3}. \qquad (5.9)$$

The effect of the Co/Cu interface is to reduce the size of the thickness dependent anisotropy by about 45%, as seen by comparing the second terms in Eq. 5.6 and Eq. 5.9. The change in the first term, the bulk anisotropy, is due to the fact that here we are considering a slightly different strain tensor and have included the magnetostatic energy, as mentioned above.

In chapter 4, we showed how an equation of the form $\Delta E_{\|-\perp} = A + B/t$ fit the experimental data for Co/Cu(1 1 13) films (Eq. 4.1). The fit gave A $= -0.9\text{x}10^5\text{erg/cm}^3$ and B $= -24\text{x}10^5\text{erg/cm}^3$ ML. We can now compare our model to this fit. The model gives the same sign for both the bulk and thickness dependent anisotropies, predicting an easy axis parallel to the steps, as observed experimentally in Co/Cu(11n). It predicts that the uniaxial anisotropy strengthens as the thickness decreases and/or as the terraces widen. We showed in chapter 4 that this behavior is observed experimentally. It is important to note that the strengthening of the uniaxial anisotropy in our uncapped vacuum/Co/Cu(1 1 13) films is consistent with the weakening of the uniaxial anisotropy with decreasing thickness in capped Cu/Co/Cu(1 1 13) films [70]. The Co/Cu interface anisotropy favors **M** perpendicular to the steps, but in uncapped films the Co/vacuum surface anisotropy dominates, giving an easy axis parallel to the steps in vacuum/Co/Cu(1 1 13) films.

While the Néel model clearly predicts the correct orientation of the easy axis, parallel to the steps, the measured strength of the in-plane anisotropy is smaller than that predicted. For example, in the 14 ML film, the measured value $\Delta E_{\|-\perp}^{experimental}$=-3x$10^5$ erg/cm^3, is approximately one third the anisotropy calculated using the model, $\Delta E_{\|-\perp,film}$=-8x10^5 erg/cm^3. The steps definitely contribute to the uniaxial anisotropy, but their effect is not as strong as it would be for perfectly aligned steps. In order to determine the reason for the discrepancy between modeled and measured anisotropies, we can examine the assumptions that went into the model, as discussed in Sec. 5.2. The most relevant is the assumption that the steps are prefectly ordered and straight. Figure 2-7 clearly shows that the steps are not ideal; the terraces are not of uniform width, and the step-edges are not straight. Thermal disordering of the steps weakens the step-induced anisotropy, causing the observed uniaxial anisotropies to be smaller than predicted. We have also not taken into account the surface relaxation, discussed on in Sec. 5.2 on page 73, which most likely occurs at the step-edges. This relaxation of atoms at step-edges will also lessen the step-edge anisotropy.

5.6 Implications of the Model

The pair-interaction model, modified to include effects of strain in a film, is not only useful in analyzing the anisotropy in vicinal films, but it also reveals important trends in thin film magnetism in general.

Relative Importance of Broken Symmetry and Strain

The results from our modified Néel anisotropy model, as listed in Tables 5.3, 5.4, and 5.5 demonstrate that the anisotropy effects due to broken symmetry at surfaces or steps (surface and step-edge magnetocrystalline anisotropies) are always much stronger than anisotropy effects due to typical biaxial misfit strains, as considered here. This is true even for Ni and permalloy, $Ni_{81}Fe_{19}$ which are both of relatively weak anisotropy and notoriously strong strain sensitivity. The strengths of the magnetocrystalline anisotropies are proportional to the interaction parameter $L(r_o)$, while strain effects are proportional to $e_oL(r_o)$ or $e_o(dL/dr)r_o$. For typical values of the misfit strain e_o, broken symmetry effects are at least one order of magnitude stronger than strain induced anisotropies. Strain effects become important in determining anisotropies only when the symmetry breaking effects balance each other, leaving only strain dependent terms in the anisotropy energies.

Thickness Dependent Magnetoelasticity

The Néel model also indicates that the bulk and surface of a material do not necessarily respond to strain in the same way. For example, in fcc(001) films strained biaxially in the plane of the film, the strain dependent bulk anisotropy is $-(6e_oL(r_o) + e_o(dL/dr)r_o)$ while the strain dependent surface anisotropy is $6e_oL(r_o)/\mathrm{t}$. For very thin films, the first term in the bulk anisotropy is partially balanced by the surface anisotropy. The magnetic response of the film to strain will then be dominated by the $e_o(dL/dr)r_o$ term in the bulk anisotropy. In thicker films, the surface effects become less important and the full bulk response, proportional to $-(6e_oL(r_o) + e_o(dL/dr)r_o)$ will govern the behavior of the film. Such thickness dependent magnetoelastic behavior can be represented by writing the magnetoelastic coupling coefficients for a film as

$$B_{film} = B_{bulk} + \frac{B_{surface}}{t_{ML}}. \tag{5.10}$$

In thick films, the magnetoelastic behavior is dominated by the bulk term; in thin films, it is governed by the surface term. The film thickness range for which the surface response dominates the behavior may be different than that predicted by our model due to exchange coupling of the surface and bulk atoms, as mentioned in Sec. 5.2. Experimental evidence for such thickness dependent magnetoelastic behavior has been found in Ni/Ag, NiFe/Ag, and Cu/Ni/Cu [40].

In certain cases, the strain dependent coefficient in the anisotropy energy, or the effective coupling coefficient for the film B_{film}, may even change sign as the film thickness is increased. For example, in Co/Cu(001) films the values of L(r_o) and (dL/dr)r_o are of opposite sign, with the magnitude of (dL/dr)r_o being larger by a factor of nearly four (See Table 5.2). While the surface effects are significant, and balancing the first term of the bulk anisotropy ($-6e_oL(r_o)$), the overall strain dependent anisotropy will have a negative coefficient (i.e. $B_{surface} < 0$). However, as the thickness increases, the sign of the strain dependent anisotropy becomes positive (i.e. $B_{bulk} > 0$). The film's magnetic response to strain can change character with film thickness.

Chapter 6

Discussion

This thesis developed from the observation that well-ordered atomic steps in the surface of an ultrathin film induce uniaxial magnetic anisotropy in the film. We hypothesized that this anisotropy arose because of one or more of the following: 1) step-edge anisotropy of a magnetocrystalline nature, 2) magnetoelastic anisotropy due to anisotropic strain in the film, and 3) magnetostatic (shape) anisotropy of the vicinal film. To determine the importance of these factors we investigated the anisotropy in vicinal films as a function of film thickness, step-density, temperature, and magnetoelastic coupling coefficient. In the previous two chapters we have presented experimental and theoretical evidence indicating that the major source of anisotropy in ultrathin vicinal films is broken symmetry around the step-edges. Here we discuss our results and their significance relative to other work in the area of thin-film magnetism.

6.1 Magnetic Anisotropies

There are several sources of magnetic anisotropy to be considered in vicinal films. To aid in our discussion of these, in Fig. 6-1 we summarize the anisotropy densities found in Co/Cu(11n). A positive anisotropy contribution favors **M** *perpendicular* to the steps; a negative contribution favors **M** *parallel* to the steps. Note that the vertical scale is logarithmic, and the surface anisotropy densities are given as $\Delta E_{\|-\perp}^{surface}/t$ so that they can be compared to bulk anisotropy densities. Magnitudes of the surface anisotropies for thicknesses t = 3, 14, and 20 ML are indicated. In thicker films, the surface contributions will of course be weaker since they are divided by the film thickness. The possible sources

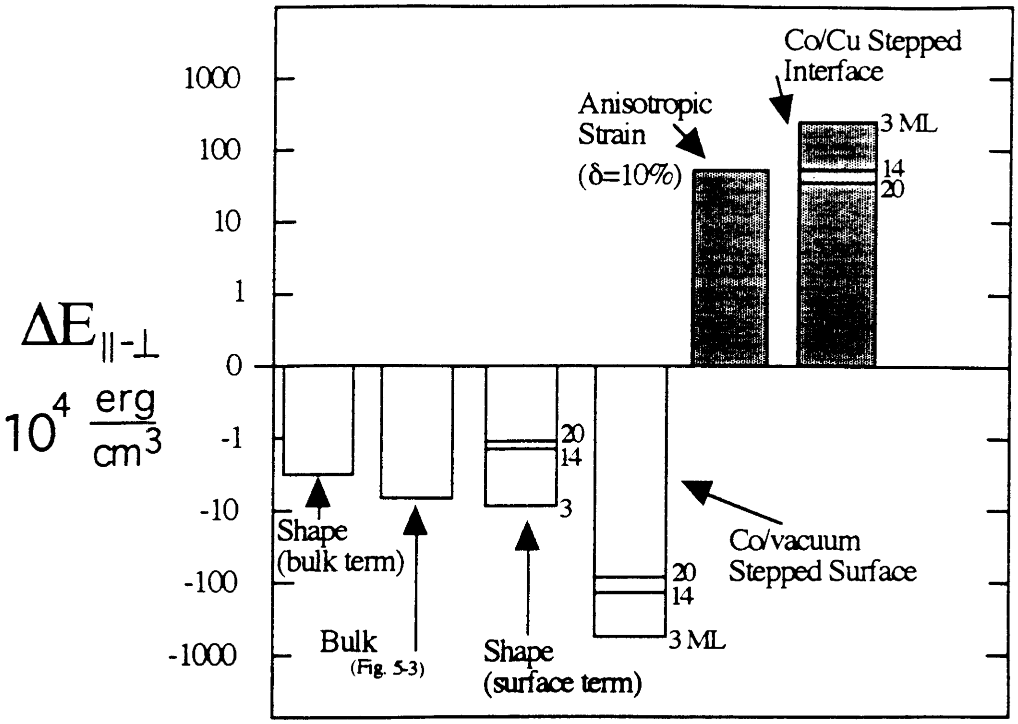

Figure 6-1: Summary of anisotropy contributions in Co/Cu(11n) films. The surface contributions are given as $\Delta E_{\|-\perp}=\Delta E^{surface}_{\|-\perp}/t$ so that they can be compared to bulk anisotropy densities ($\Delta E_{\|-\perp}=\Delta E^{bulk}_{\|-\perp}$). The strength of the surface anisotropy is indicated for film thicknesses t = 3, 14, and 20 ML. In thicker films, the surface contribution will be less significant to the overall anisotropy. Positive anisotropies favor **M** perpendicular to the steps; negative anisotropies favor **M** parallel to the steps.

of **positive** anisotropy in vicinal Co fims are anisotropic strain (Eq. 4.16), and the Co/Cu interface anisotropy (Sec. 5.5). The sources of **negative** uniaxial anisotropy are the shape of the film (Eq. 4.12) which we have separated into the bulk and surface contributions, the bulk anisotropy present when **M** is in the (11n) plane (Fig. 5-3), and the Co/vacuum surface anisotropy (Sec. 5.3, Eq. 5.6). The total anisotropy of the film is the net of these coexisting contributions.

Step-Edge Magnetocrystalline Anisotropy

The anisotropy due to reduced coordination symmetry around atoms at the step-edges, a magnetocrystalline anisotropy, appears to be the most important factor in determining the in-plane anisotropy in vicinal films. The dependence of the anisotropy in Co/Cu(11n) on film thickness (t) and terrace width (d) is consistent with that of a step-edge effect. Such an anisotropy should vary as 1/t and 1/d. We were able to fit the thickness-dependent anisotropy data of the Co/Cu(1 1 13) film quite well with an equation of the form A + B/t. We were not able to fit the terrace-width dependent anisotropy in a similar fashion with an equation of the form A + B/d because the anisotropy in the Co/Cu(117) film was too strong. With the magnetic fields available *in situ* we could not bring the (117) films close enough to saturation to reasonably estimate the anisotropy in Co/Cu(117) films up to 14 ML thick. However, the experimental data clearly show that as the terrace width decreases, the strength of the uniaxial anisotropy increases in Co/Cu(11n) films.

We have considered those factors besides the step-edges that will yield a 1/t dependence in the anisotropy. One such factor may be a thickness-dependent strain in the Co/Cu(11n) films, although for Co/Cu(001) films of the thicknesses we consider here, the strain is found to be quite constant with thickness [56]. The surface anisotropy model presented in chapter 5 indicates that in-plane anisotropy due to reduced symmetry is much stronger than strain-induced anisotropy. Therefore, even if the strain is thickness dependent in the vicinal film, its anisotropy effects should be relatively insignificant.

Applying the pair-interaction model applied to vicinal films, we were able to model the thickness and terrace-width dependence of the anisotropy. Our model was successful in reproducing the observed easy axis *parallel* to the steps in Co/Cu(11n) films, as well as the easy axis *perpendicular* to the steps in Fe/W(01n). The size of the anisotropy predicted by the model is approximately three times larger than that observed in Co/Cu(11n). As discussed in chapter 5, this discrepancy is most likely due to surface relaxation and thermal roughening of the steps. Atoms at the surface of a metal generally relax inward toward the bulk in an attempt to restore the electron density deficit that is associated with a surface [34]; there will be a similar relaxation of atoms at step-edges [33]. The anisotropies induced by surfaces and step-edges will not be as severe as those we predict without considerations of surface relaxation. Thermal roughening will cause kinks or jogs in the step-edges. Local anisotropy effects of atoms at the kinks will balance the effects due to step-edge atoms, washing out the step-induced uniaxial anisotropy. Because our pair-interaction model of vicinal films accounts for neither surface relaxation nor thermal roughening, it is reasonable that our predicted anisotropies are larger than those we observe experimentally.

A significant result of our investigation of anisotropy in vicinal films using the pair-interaction model is that in Co/Cu(11n) films, the surface (Co/vacuum) anisotropy and the interface (Co/Cu) anisotropy are of opposite sign, as indicated in Fig. 6-1. The former favors **M** *parallel* to the steps, the latter favors **M** *perpendicular* to the steps. Because the magnitude of the Co/vacuum anisotropy is larger than that of the Co/Cu anisotropy, in Co/Cu(11n) films the combined effect of the surface and interface is to favor **M** parallel to the steps: the thickness dependent term in Eq. 4.1 is negative.

This result is shown graphically in Fig. 6-2. The fit to our Co/Cu(1 1 13) in-plane anisotropy data (Fig. 4-3, pg. 46) is plotted as the anisotropy multiplied by the film thickness ($(\Delta E_{||-\perp})t$) in a solid line.

$$(\Delta E_{||-\perp})t = (\Delta E^{bulk}_{||-\perp})t + \Delta E^{surface}_{||-\perp} \tag{6.1}$$

As indicated in the figure, the slope of the line is the bulk contribution to the anisotropy, and the intercept when the line is extrapolated to zero thickness indicates the thickness-dependent contribution to the anisotropy. This thickness-dependent contribution, although labeled only *surface* in the figure, is a combination of the stepped surface and interface effects. From Fig. 6-2, it is clear that both the bulk and combined surface/interface anisotropies are negative in Co/Cu(1 1 13) films, favoring **M** parallel to the steps.

The significance of the Co/Cu interface anisotropy is revealed when we compare our Co/Cu(1 1 13) anisotropy data to the anisotropy data taken by Krams *et al.* [70] from Cu/Co/Cu(1 1 13) films. The difference between these two types of films being that the latter are capped with a 20 ML layer of Cu. A fit to their data, taken from Fig. 3 of Ref. [70] is shown in Fig. 6-2 as the dashed line. There are two primary differences between the anisotropy we measure from Co/Cu(1 1 13) films and the anisotropy of Cu/Co/Cu(1 1 13): 1) the intercept of $(\Delta E_{||-\perp})t$, representing the surface/interface anisotropy, is positive for the capped films, but negative for our uncapped films, and 2) the slope of $(\Delta E_{||-\perp})t$ is more negative for the capped films, meaning the vicinal films' bulk contribution to the anisotropy is more negative.

The change in sign of the intercept is expected given our knowledge of Co/vacuum and Co/Cu anisotropies. In Cu/Co/Cu(1 1 13) films, there are only Co/Cu interfaces, both contributing interface anisotropies favoring **M** perpendicular to the steps (Fig. 6-1).

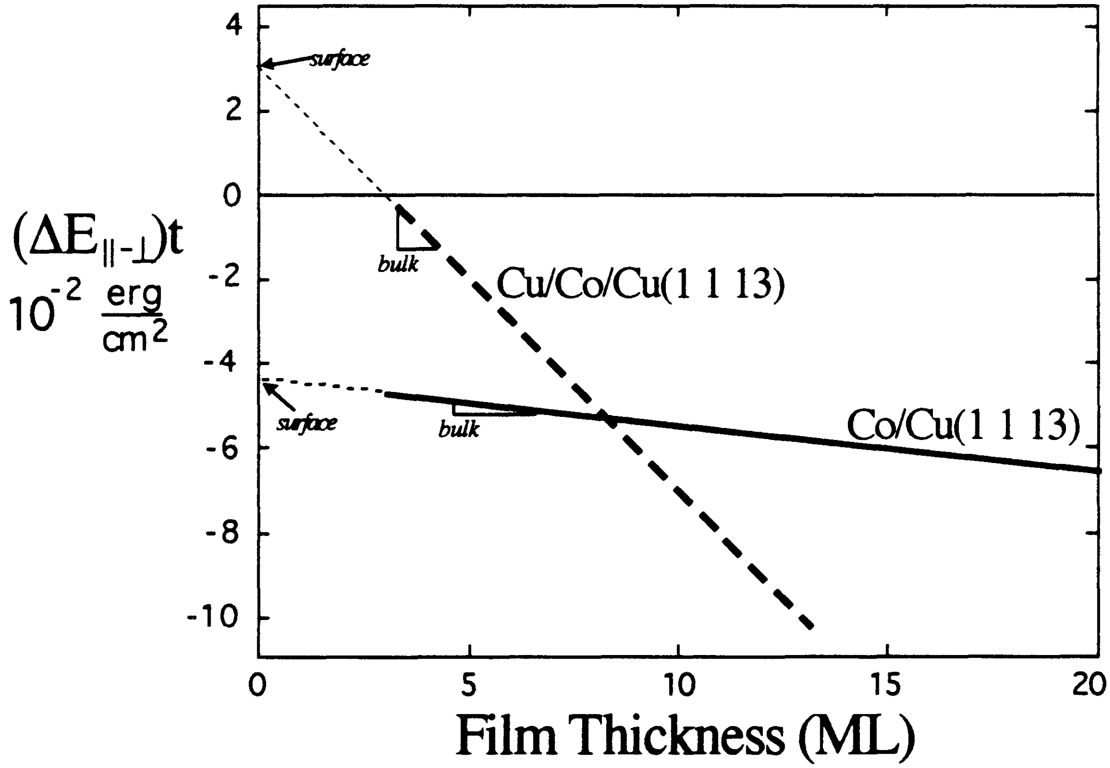

Figure 6-2: Linear fits to uniaxial in-plane anisotropy *vs*. thickness data from Co/Cu(1 1 13) in the solid line, and Cu/Co/Cu(1 1 13) in the dashed line. The slope of a line represents the bulk anisotropy, the intercept represents the combined surface and interface anisotropy.

There is no Co/vacuum anisotropy present in these films. Thus, we expect the intercept of $(\Delta E_{\|-\perp})t$ to be positive. It may be somewhat surprising that just capping a magnetic film with copper creates such a change in the magnetic anisotropy of the film. Our analysis of anisotropy in Co vicinal films using the pair-interaction model has demonstrated that this is in fact the case: the anisotropy results from the capped and uncapped films are consistent with one another.

The change in slope of $(\Delta E_{\|-\perp})t$ vs t indicates that covering the cobalt vicinal films with Cu somehow adds (or removes) a bulk contribution to the anisotropy. We suggest that upon capping the film, the positive magnetoelastic anisotropy caused by anisotropic strain (Fig. 6-1) in the vicinal cobalt film is removed, making the total bulk anisotropy more negative relative to that in uncapped Co/Cu(1 1 13). In our discussion of the magnetoelastic anisotropy in Sec. 4.1.6 on page 63, we suggested that because of the presence of surface steps, the biaxial in-plane misfit strain observed in Co/Cu(001) films may relax perpendicular to the steps in Co/Cu(11n) films. Surface relaxation at the step-edges would also reduce the misfit strain perpendicular to the steps. These two effects would produce an anisotropic strain in vicinal Co films, and thus create a magnetoelastic anisotropy. If the ultrathin Co film is capped with copper, surface relaxation will not be present to such a large degree in the cobalt. The cobalt atoms will no longer experience the large electron density deficit that they do at a Co/vacuum interface. Also, the capping layer will presumably further constrain the Co film to the lattice constant of copper, preventing much relaxation of the misfit strain. We would then expect that if anisotropic strain contributes a positive bulk anisotropy in uncapped Co/Cu(11n) films (Fig. 6-1), this magnetoelastic anisotropy would not be present in capped Cu/Co/Cu(1 1 13) films resulting in a change in slope of $(\Delta E_{\|-\perp})t$ vs t. A strain relief of $\delta \approx 9\%$ (Eq. 4.16) in Co/Cu(1 1 13) would produce the observed discrepancy in the bulk anisotropy of capped and uncapped Co/Cu(1 1 13) films.

The realization that the Co/vacuum surface and the Co/Cu interface anisotropies are of opposite sign also sheds light on some of the observed temperature effects in Co/Cu(1 1 17) films [71] described in the literature review in chapter 2. In a 2.4 ML film of Co/Cu(1 1 17), Oepen and co-workers observed the hysteresis loops shown in Fig. 6-3. At temperatures between 25^oC and 100^oC, the in-plane anisotropy is uniaxial, favoring **M** parallel to the steps (Fig. 6-3a,b), as expected for a Co/Cu(11n) film dominated by the Co/vacuum anisotropy. At 100^oC, the anisotropy changes to weakly favor **M** perpendicular to the steps

(Fig. 6-3c,d). At 115^oC, the film again shows uniaxial anisotropy favoring M parallel to the steps (Fig. 6-3e,f); however, the magnitude of the anisotropy is smaller than it was at temperatures below 100^oC. Oepen and co-workers' qualitative explanation for these transitions is that perhaps at 100^oC thermal roughening of the Co/vacuum surface steps occurs and changes the anisotropy, and then at 115^oC the Co/Cu interface steps roughen, changing the anisotropy yet again.

Our understanding of the anisotropy contributions in Co/Cu(11n) films (Fig. 6-1) lends further evidence that their explanation is correct. Figure 6-4 indicates that there are three types of magnetic anisotropy present in Co/Cu(11n) films: 1) Co/vacuum surface anisotropy, 2) Co/Cu interface anisotropy, and 3) bulk anisotropy. These are represented by a shaded arrow, a white arrow, and a black arrow, respectively, on the schematic vicinal surface in Fig. 6-4a. The size and direction of the arrows represents the magnitude and sign of the anisotropy contributions in a 3 ML film. At low temperature, when surface and interface steps are still reasonably straight, all three anisotropy contributions will be present. The combination of these effects, indicated in Fig. 6-4b, will result in a net anisotropy which gives a magnetic easy axis parallel to the steps. If the surface steps roughen at $= 100^oC$ washing out the Co/vacuum surface anisotropy, the remaining interface and bulk contributions result in a weak anisotropy favoring M perpendicular to the steps (Fig. 6-4c). This corresponds reasonably well with the observation of Oepen and co-workers for temperatures between $= 100^oC$ and 115^oC. If at 115^oC the interface steps roughen washing out the Co/Cu interface anisotropy, the film is left with only the bulk contribution to the in-plane uniaxial anisotropy (Fig. 6-4d). The bulk anisotropy again yields an easy axis parallel to the steps, but the anisotropy is much weaker than the Co/vacuum surface anisotropy present at lower temperatures. Again, this behavior is consistent with the experimental results shown in Fig. 6-3.

Shape Anisotropy of Vicinal Films

Our own temperature-dependent study of the anisotropy in Co/Cu(11n) was intended to reveal the importance of magnetostatic or shape anisotropy in vicinal films. While it was unsuccessful in this area because of thermal roughening of the steps, it did reveal interesting results as discussed in chapter 4. We showed that the anisotropy in fcc vicinal films is a combination of cubic and uniaxial anisotropies. The cubic anisotropy is present because

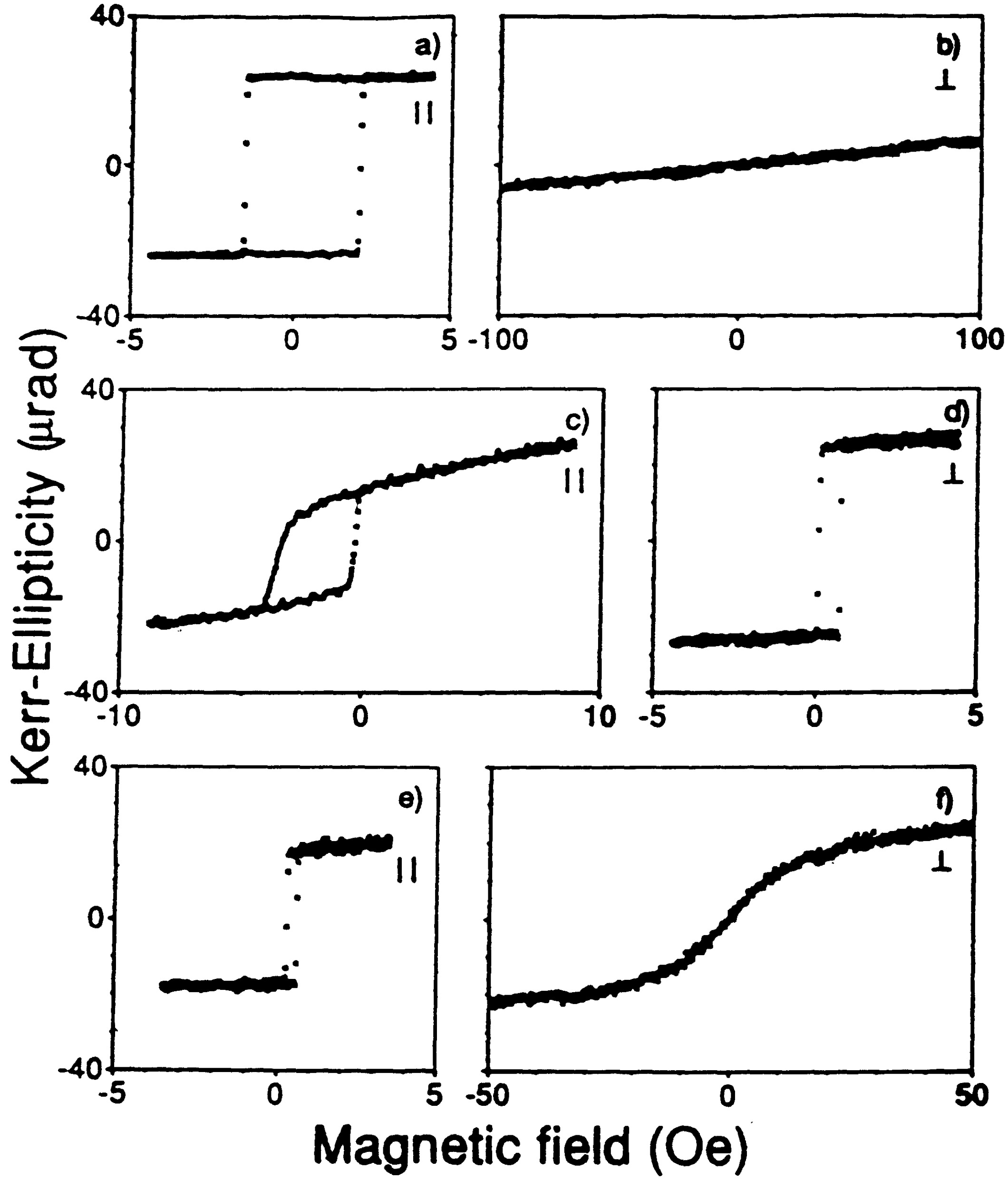

Figure 6-3: Hysteresis loops, from top to bottom, taken at temperatures (a,b) $T < 100°C$, (c,d) $100°C < T < 115°C$, and (e,f) $T > 115°C$ for a 2.4 ML Co/Cu(1 1 17) film with the applied field (a,c,e) parallel to the steps, and (b,d,f) perpendicular to the steps.

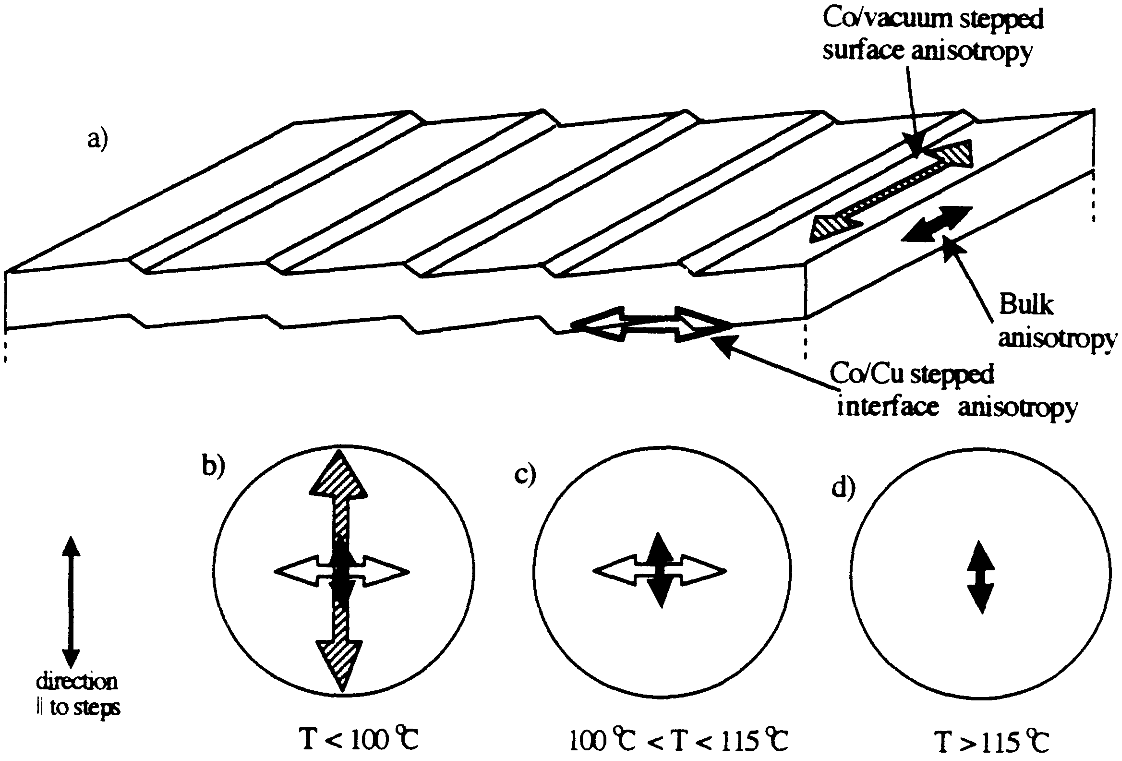

Figure 6-4: **a**) Schematic of a Co/Cu(1 1 17) film, and anisotropy contributions present at b) $T < 100^{\circ}C$, c) $100^{\circ}C < T < 115^{\circ}C$, and d) $T > 115^{\circ}C$.

the cobalt's bulk fcc crystal structure produces a cubic magnetocyrstalline anisotropy. The uniaxial anisotropy is a combination of the step-induced anisotropies summarized in Fig. 6-1. We observed that the strength of the uniaxial anisotropy decreases as temperature increases, going to zero at approximately 130^oC, well below the Curie temperature of the film. This thermal effect further supports the conclusion that the dominant uniaxial anisotropy is a step-edge effect and washes out at higher temperatures due to disordering, or roughening, of the steps.

In an alternate approach to investigating the importance of shape anisotropy in a vicinal film, we calculated its magnetostatic energy by treating the film as a collection of discrete magnetic dipoles (Sec. 4.1.5). This calculation reveals that indeed there is a uniaxial in-plane shape anisotropy in vicinal films which favors **M** parallel to the steps. However, this anisotropy is relatively small, as indicated in Fig. 6-1.

Magnetoelastic Anisotropy

In order to determine the importance of magnetoelastic effects in vicinal films, we investigated the in-plane anisotropy in $Ni_{79}Fe_{21}$/Cu(117). The magnetoelastic effects modeled in chapter 4 (Eqn. 4.16) are insignificant in $Ni_{79}Fe_{21}$ relative to Co because the magnetoelastic coupling coefficient B_2 is two orders of magnitude smaller in $Ni_{79}Fe_{21}$. We expected that we would therefore be able to clearly see any other type of anisotropy. However, the step-edge anisotropy modeled in chapter 5, is also small in $Ni_{79}Fe_{21}$ relative to Co because the strength of this anisotropy also depends on the magnetoelastic coupling coefficients; the magnetoelastic coupling coefficients determine the values of the interaction coefficients (e.g. $L(r_o)$) in the pair-interaction model.

We have applied the pair model of step anisotropy to $Ni_{79}Fe_{21}$ in order to estimate the size of the uniaxial anisotropy in $Ni_{79}Fe_{21}$/Cu(117). Note that the pair model presented in chapter 5 considers only elemental materials. It is not strictly applicable to alloys in which some of the nearest neighbors of an atom will be the same element, and others will not. In $Ni_{79}Fe_{21}$, the Néel interaction parameters $L(r_o)$ and $(dL/dr)r_o$ would be different for Ni-Ni, Fe-Fe, and Ni-Fe interactions. By applying the model here to $Ni_{79}Fe_{21}$ we are actually determining the expected anisotropy for an elemental material with the same materials parameters as $Ni_{79}Fe_{21}$ and are thus using an average $L(r_o)$ and $(dL/dr)r_o$ which will represent the alloy.

The model again predicts a reasonable in-plane anisotropy: $\Delta E_{\|-\perp} = -1.3\text{x}10^5$ erg/cm^3 for a 14 ML $Ni_{79}Fe_{21}$/Cu(117) film. Comparing the calculated Ni-Fe anisotropy to the experimentally measured $\Delta E^{exp}_{\|-\perp} = -1.5\text{x}10^4$ erg/cm^3, presented at the end of chapter 4, we see that the sign is correct; the easy axis is parallel to the steps. The predicted size of the anisotropy is again larger than that observed. As discussed regarding Co/Cu(11n), this discrepancy is most likely due to surface relaxation and roughening of the steps. However, we are also not able to account fo the Ni-Fe/Cu interface anisotropy (as opposed to the Ni-Fe/vacuum surface anisotropy).

It is possible that anisotropic strain in the film is partially responsible for the uniaxial anisotropy in $Ni_{79}Fe_{21}$. Using the B_2 value for $Ni_{79}Fe_{21}$ of -1.8x10^6 erg/cm^3 [58] and e_o= 0.03 [59], the magnetoelastic anisotropy predicted by Eq. 4.16 is $\Delta E_{\|-\perp}$=-5.4x10$^4\delta$ erg/cm^3. If 30% of the misfit strain were relieved perpendicular to the steps, this would give rise to the measured uniaxial anisotropy in the 14 ML film. Because the value of B_2 is negative for the Ni-Fe film, this magnetoelastic anisotropy does give the observed easy axis, parallel to the steps. In the Co films, the magnetoelastic anisotropy predicted an easy axis in the direction perpendicular to the steps, contrary to what was experimentally observed. It is possible that a small amount of this magnetoelastic anisotropy is present in the Co films, but that the anisotropy caused by broken symmetry at the step-edges is so strong that the magnetoelastic anisotropy is insignificant. In the Ni-Fe films, where the anisotropy due to broken symmetry at the step-edges is at least two orders of magnitude weaker than in cobalt, the magnetoelastic anisotropy is more significant.

Magnetoelastic Coupling in Thin Films

Our goal in this study of magnetic anisotropy in vicinal films was not to just learn about the specific vicinal films, but to also gain insight into magnetic behavior of thin films in general. We have realized this goal through the development and application of the pair-interaction model in chapter 5. This type of model was previously used by others including Néel [1], Gradmann [83], and Victora and MacLaren [18] to examine anisotropy in thin films. Our contribution has been not only to apply the model to vicinal films, but also to include strain effects in the model and examine the common cubic, low-index film orientations. Some of the broader implications of this modified pair-interaction model have already been discussed in Sec. 5.6, but one of the implications, surface magnetoelasticity, deserves further discussion.

From the pair-interaction model's results, we know that the magnetic energy of a film has the form:

$$E_{film} = E_{bulk} + \frac{E_{surface/interface}}{t}, \tag{6.2}$$

where $E_{surface/interface}$ is due to surface effects, interface effects, or a combination of the two, as we have discussed previously. We have left out the step-edge term for now, considering only flat films (e.g. Co/Cu(001)). Néel showed that this thickness dependence of the energy is reflected in a thickness dependence of the anisotropy constants K_i [1], typically written as

$$K_i^{eff} = K_i + \frac{K_{surface}}{t}. \tag{6.3}$$

Thickness dependent magnetic anisotropies are well accepted and experimentalists always consider them in analysis of thin-film results. From the results of the pair-interaction model modified to include strain, we can also conclude that the magnetoelastic coupling coefficients depend on thickness:

$$B_i^{eff} = B_i + \frac{B_{surface}}{t}. \tag{6.4}$$

This result indicates that just as bulk anisotropy constants of a material do not apply for that material in thin-film form, bulk magnetoelastic coupling coefficients are not necessarily valid in thin films either. More effort should be made to properly characterize surface magnetoelastic coupling coefficients, and to consider this thickness dependence in B_i^{eff} when analyzing the magnetic behavior of films. Bochi, Song, and O'Handley have recently demonstrated the types of errors possible in the determination of anisotropy constants if surface magnetoelastic coupling coefficients are neglected [84]. Experimental observation of surface magnetoelastic coupling coefficients has been reported in polycrystalline NiFe/Ag/Si, NiFe/Cu/Si, and Ni/SiO_2 [40], in amorphous CoCrB [38] and in polycrystalline Ni/Ag multilayers [39].

$B_{surface}$ can be derived, using the pair-interaction model, from the strain-dependent terms in the surface energy, $E_{surface}$ (Tables 5.3, 5.4, and 5.5). The forms of $E_{surface}$ for a given crystal structure are clearly different for differently oriented films (e.g. (001), (110), or (111)). Therefore, the value of $B_{surface}$ will depend on the orientation of the film. $B_{surface}$ is also sensitive to first order to the symmetry of the strain in the film. Recall that the energy expressions given in Tables 5.3, 5.4, and 5.5 are based on the assumption that the film is biaxially strained in the plane of the film. If we consider instead a uniaxial strain in the film plane, the strain-dependent terms in the magnetic energies will be different. This reflects the fact that the coordination symmetry is different around surface atoms in these two cases. For proper calculation of $B_{surface}$, knowledge of the film's orientation and state of strain is necessary.

6.2 Summary

In summary, the purpose of this thesis was to improve the level of understanding of magnetic anisotropy in thin films by focusing on how the presence of surface steps induces uniaxial anisotropy in vicinal films. We have attempted to consider all probable sources of the uniaxial anisotropy and investigate them both experimentally and through theoretical models. The small amount of previous work on vicinal films has focussed primarily on experimental observation of the step-induced anisotropy and has lacked in explanations as to why the anisotropy is present. The explanations that have been given have considered only the bulk anisotropy contribution in vicinal films. Our investigation has demonstrated that the most important source of the step-induced anisotropy is reduced coordination symmetry around atoms at the step-edge. The sign, size, and dependence on film thickness and terrace width of this anisotropy are all predicted by a pair-interaction model. In addition to increasing our understanding of anisotropy in vicinal films, our results have also demonstrated the importance of interface anisotropy, and surface magnetoelastic effects. Understanding of these factors is crucial now that many applications of magnetic materials require the material in thin-film form where interface and surface effects begin to dominate the behavior of the film.

Chapter 7

Suggestions for Future Work

While this thesis has made significant progress in the understanding of magnetic anisotropy in vicinal films, it has also pointed to areas in which better understanding is needed. Here we offer suggestions for further work to deal with three of the remaining issues: 1) step-roughening in magnetic vicinal films, 2) anisotropic in-plane strains, and 3) in-plane magnetic anisotropy in $Ni_{60}Fe_{40}/Cu(11n)$, which we predict to have practically no step-edge magnetocrystalline anisotropy. Following the suggestions regarding these issues, we present some ideas for additional studies considered as long-term extensions of this thesis.

Step-Roughening

The anisotropy in vicinal films is sensitive to temperature. The changes in anisotropy that occur as temperature increases are presumably due to thermal roughening of the steps on the surface of the vicinal film and at the film/substrate interface. A concurrent investigation of step-roughening in a vicinal magnetic film and its magnetic anisotropy would be very useful. Previous roughening studies have only involved bare Cu(11n) substrates, not the ultrathin magnetic film. Such a study could be done in an UHV STM outfitted with the equipment described in chapter 3 for deposition and magnetic characterization, or it could be done using He^{+}-scattering to characterize the step roughening.

Anisotropic Strain

A measurement of the in-plane strain parallel and perpendicular to the steps would allow for a more conclusive determination of the magnetoelastic anisotropy present in vicinal films.

This measurement would have to be done using *in-situ*, non-destructive techniques, such as electron diffraction or He^+-scattering, as any processing or contamination would alter the state of strain in the film.

Anisotropy in $Ni_{60}Fe_{40}/Cu(11n)$

A further test of the pair-interaction model could be made by examining Ni-Fe alloy films of compositions surrounding the point at which, because of the bulk magnetoelastic coupling coefficients, the model predicts a change in sign of $\Delta E_{\|-\perp}$. This composition is around 60% Ni. As mentioned in the discussion of our anisotropy results, we had initially expected that the magnetoelastic anisotropy would be small in $Ni_{79}Fe_{21}$, leaving the remaining anisotropy, due to sources other than anisotropic strain, clearly visible. However, as it turned out, the other anisotropies were also quite small in $Ni_{79}Fe_{21}$. The opposite approach to this investigation of magnetoelastic effects may be more fruitful. If we were to investigate the anisotropy in $Ni_{60}Fe_{40}$, the step-edge magnetocrystalline anisotropy should be zero, presumably leaving only the small shape anisotropy of a vicinal film and the magnetoelastic anisotropy induced by any anisotropic strain present.

Long-Term Future Work

We suggest the following topic for investigations branching out from this thesis:

1. Use the pair-interaction model to identify candidates for perpendicular recording media, investigating variations in materials, strains, film orientations, and interface interactions (possible only if pair-interaction coefficients are known for the interfaces).

2. Deposit sub-monolayer magnetic films on the vicinal surfaces. Presumably the result would be strips of magnetic material at the step-edges. Use these structures to investigate 1-dimensional magnetism, and to investigate magnetic exchange, or coupling between the strips. It is speculated that such structures may show giant magnetoresistance.

3. Investigate the practical application of vicinal surfaces to induce uniaxial anisotropies in magnetic devices such as spin-valves. Presently, exchange between a magnetically soft film and an antiferromagnet is used to induce an anisotropy in the soft film necessary for optimum performance of spin-valve structures in future magnetic recording

heads. Thermal stability of the anisotropy will be an important issue in this investigation.

Chapter 8

Conclusions

In this thesis we have investigated a new phenomenon in magnetic surface anisotropy: the inducement of uniaxial anisotropy in thin films by steps on a vicinal substrate. Our main experimental findings were the following:

- We can repeatedly deposit clean, epitaxial fcc Co films on Cu(11n) substrates and measure in-plane magnetic anisotropies for films down to a thickness of 3 ML.
- Co/Cu(117) and Co/Cu(1 1 13) films exhibit uniaxial in-plane anisotropy which favors magnetization parallel to the steps for thicknesses up to at least 20 ML.
- The uniaxial in-plane anisotropy in Co/Cu(1 1 13) becomes stronger as the Co thickness decreases, consistent with a 1/t dependence.
- The uniaxial in-plane anisotropy in Co/Cu(11n) becomes stronger as n (i.e. the terrace width) decreases.
- The uniaxial in-plane anisotropy in Co/Cu(1 1 13) weakens as the temperature increases from 25°C to 127°C, vanishing well below T_c.
- $Ni_{79}Fe_{21}$/Cu(117) films exhibit uniaxial in-plane anisotropy which favors magnetization parallel to the steps for thicknesses up to at least 14 ML.
- The uniaxial anisotropy in $Ni_{79}Fe_{21}$ is approximately two orders of magnitude smaller than the anisotropy in Co/Cu(117).

The major results of our theoretical models are the following:

- A Néel pair-interaction model of vicinal films predicts an anisotropy energy density of the form:

$$E_{film} = E_{bulk} - \frac{2E_{surface}}{t} - \frac{2E_{step}}{t\,d}. \tag{8.1}$$

- Step-edge magnetocrystalline anisotropy in Co/Cu(11n) favors **M** parallel to the steps for all thicknesses.

- The Co/vacuum stepped interface favors **M** parallel to the steps, but the Co/Cu stepped interface favors **M** perpendicular to the steps in a (11n) film. The former is stronger.

- Step-edge magnetocrystalline anisotropy in Fe(01n) vicinal films favors **M** perpendicular to the steps.

- The Fe/vacuum stepped interface favors **M** perpendicular to the steps in a (01n) film.

- Anisotropy due to reduced symmetry at surfaces or step-edges is at least an order of magnitude larger than strain-induced anisotropy when considering biaxial misfit strains.

- Magnetoelastic coupling coefficients in thin films exhibit a thickness dependence:

$$B_{film} = B_{bulk} + \frac{B_{surface}}{t}. \tag{8.2}$$

- A discrete dipole calculation of the magnetostatic anisotropy in vicinal films reveals a small in-plane uniaxial anisotropy favoring **M** parallel to the steps.

- For thicknesses above approximately 4 ML, this shape anisotropy also decreases with increasing thickness, consistent with a 1/t dependence.

- Magnetoelastic anisotropy due to anisotropic strain in Co/Cu(11n) vicinal films is favors **M** perpendicular to the steps, assuming a *bulk* B_2.

Our experimental evidence and the results of our anisotropy models lead us to the following conclusions regarding anisotropy in vicinal films. The major source of the step-induced uniaxial anisotropy is a stepped-surface magnetocrystalline anisotropy due to the reduced local symmetry around atoms at the step-edges. Depending on the materials parameters, mainly magnetoelastic coupling coefficients B_1 and B_2, and the structure of the material, this anisotropy can favor **M** parallel or perpendicular to the steps. The shape anisotropy of vicinal films contributes some in-plane anisotropy as well, but the strength of this anisotropy is typically an order of magnitude less than the step-edge magnetocrystalline anisotropy. Magnetoelastic effects due to anisotropic strain in vicinal films also only become important if the step-edge anisotropy is very weak. Magnetoelastic effects are insignificant in Co/Cu(11n) films. Because the uniaxial anisotropy is due to step-edge effects, it is weakened considerably by thermal roughening of the steps, and vanishes well below the Curie temperature.

Appendix A

Derivation of Anisotropy Energy

This derivation involves summing the anisotropy for a bulk site over all the atoms in the film. The anisotropy energy created when bonds are broken to create the surfaces of the film and the steps in the film are then subtracted from the bulk anisotropy. The parameters used in the derivation are defined in Table A.1.

The volume of the film is

$$V_{film} = HLW \qquad cm^3 \tag{A.1}$$

and the number of atoms in the film is given by

$$N_{film} = (\rho \ \ atoms/cm^3)(V_{film} \ \ cm^3) = \rho HLW \qquad atoms \tag{A.2}$$

where ρ is the atomic density. The bulk anisotropy energy for all atoms in the film is

$$\epsilon_{film} = E^{atom}_{bulk} \rho HLW \qquad erg \tag{A.3}$$

where E^{atom}_{bulk} is in units of erg/atom. We must now subtract the anisotropy energy due to broken bonds at the surface ($E^{atom}_{surface}$ erg/atom) and at the steps ($E^{atom}_{step-edge}$, $E^{atom}_{step-corner}$ both in erg/atom). The total number of surface atoms in the film is

$$N_{surf} = 2(\rho \ \ atoms/cm^3)(W \ \ cm)(1 \ ML)(h \ \ cm/ML)(L \ \ cm) = 2\rho WhL \qquad atoms \tag{A.4}$$

The factor of two is present in the above equation because the film has 2 surfaces: film/vacuum and film/substrate. We assume that the anisotropy is the same for both

Parameter	Definition	Units
$H = n_h\, h$	Film thickness	cm
n_h	Number of monolayers in the film	ML
h	Thickness of one monolayer	cm/ML
L	Length of the film (measured parallel to the steps)	cm
$W = n_w\, w$	Width of the film (measured perpendicular to the steps)	cm
n_w	Number of atoms in the width of the film	atoms
w	Distance between atoms (measured perpendicular to the steps)	cm/atom

Table A.1: Parameters used in counting the atoms in the film.

surfaces and neglect any magnetic interaction between the film and substrate, as discussed in Sec. 5.2, on page 73.

The number of step atoms is just the fraction of surface atoms which occurs at the edges of the terraces. This number is obtained by dividing N_{surf} by d_A, the number of atoms in one terrace width.

$$N_{step} = \frac{N_{surf}}{d_A} = \frac{2\rho WhL}{d_A} \qquad atoms \tag{A.5}$$

The anisotropy energy of the film is then

$$\epsilon_{film} = \rho WHLE^{atom}_{bulk} - 2\rho WhLE^{atom}_{surface} - 2\rho WhL\frac{(E^{atom}_{step-edge} + E^{atom}_{step-corner})}{d_A} \quad erg \tag{A.6}$$

The energy per volume is

$$E_{film} = \frac{\epsilon_{film}}{WHL} = E^{atom}_{bulk}\rho - 2\rho\frac{E^{atom}_{surface}}{n_h} - 2\rho\frac{(E^{atom}_{step-edge} + E^{atom}_{step-corner})}{n_h d_A} \quad erg/cm^3 \tag{A.7}$$

If we write this in terms of E_{bulk} energy/volume, $E_{surface}$ energy/area, $E_{step-edge}$ energy/length, $E_{step-corner}$ energy/length, t the film thickness, and d the terrace width, we obtain Eq. 5.5.

$$E_{film} = E_{bulk} - 2\frac{E_{surface}}{t} - 2\frac{(E_{step-edge} + E_{step-corner})}{t\ d} \qquad erg/cm^3 \tag{A.8}$$

Appendix B

Mathematica Program for Pair-Interaction Model

The following program written for Mathematica^{TM} was used to calculate the surface, and step anisotropies given in chapter 5. Comment lines in the program are in italics.

```
Off[General::spell1];
Off[General::spell];
```

Rules used to simplify the form of the results, and constants used to simplify the program.

```
rule1 = bb_ a1^2 + bb_ a2^2 + bb_ a3^2 -> bb;

rule2 = cc_ a1^4 + cc_ a2^4 + cc_ a3^4 -> cc - 2 cc a1^2 a2^2 -
2 cc a2^2 a3^2 - 2 cc a1^2 a3^2;

rule3 = dd_ a1^2 a2^2 + dd_ a2^2 a3^2 + dd_ a1^2 a3^2 -> dd x;

rep[a_] := a //. {exx^2 -> 0, exy^2 -> 0, exz^2 -> 0, eyy^2 -> 0,
    ezz^2 -> 0, eyz^2 -> 0, exy eyy -> 0, exy exx -> 0,
    exy exz -> 0, exy eyz -> 0, exy ezz -> 0, exz eyz -> 0,
    exz exx -> 0, exz eyy -> 0, exz ezz -> 0, eyz exx -> 0,
    eyz eyy -> 0, eyz ezz -> 0, exx eyy -> 0, exx eyy -> 0,
    eyy ezz -> 0, exx^3 -> 0, exy^3 -> 0, exz^3 -> 0,
    eyy^3 -> 0, ezz^3 -> 0, eyz^3 -> 0};

a = 0.57735;
b = 0.288675;
c = 0.866025;
d = 0.353553;
```

```
e = 0.408248;
f = 0.204124;
g = 0.612372;
h = 0.816497;
sq2 = 0.707107;
```

The following are atomic positions for nearest-neighbors around the atom indicated, given in the coordinate systems indicated. For **surface** *atoms, the positions of atoms that must be removed from the cluster around a bulk atom in order to obtain a surface atom's nearest-neighbor cluster are given. These are used to calculate* $E_{surface}$. *For* **step-edge** *atoms, the position of the atoms that must be removed from a surface atom's nearest-neighbor cluster in order to obtain the nearest-neighbor cluster around a step-edge atom are given. These are used to calculate* $E_{step-edge}$. *For* **step-corner** *atoms, the positions of atoms that must be removed from a bulk atom's nearest-neighbor cluster in order to obtain a step-corner atom's nearest-neighbor cluster are given. These are used to calculate* $E_{step-corner}$.

Bulk sites (sc = simple cubic, fcc = face-centered cubic, bcc = body-centered cubic). Coordinate System: x=[100], y=[010], z=[001]

```
sc = {{1,0,0},{-1,0,0},{0,1,0},{0,-1,0},{0,0,1},{0,0,-1}};
scnn = 6;

fcc = {{0.5,0,-0.5},{0,0.5,-0.5},{-0.5,0,-0.5},
    {0,-0.5,-0.5},{-0.5,-0.5,0},{0,-0.5,0.5},
    {-0.5,0.5,0},{0.5,-0.5,0},{0.5,0.5,0},
    {0.5,0,0.5},{0,0.5,0.5},{-0.5,0,0.5}};
fccnn = 12;

bcc = {{0.5,0.5,0.5},{0.5,-0.5,0.5},{-0.5,0.5,0.5},
    {-0.5,-0.5,0.5},{0.5,0.5,-0.5},{0.5,-0.5,-0.5},
    {-0.5,0.5,-0.5},{-0.5,-0.5,-0.5}};
bccnn = 8;
```

Simple Cubic (001) Surface, Coordinate System: x=[100], y=[010], z=[001]

```
sc001 = {{0,0,1}};
sc001nn = 1;
```

Simple Cubic (110) Surface, Coordinate System: x=[001], y=[1 -1 0], z=[110]

```
sc110 = {{0,-sq2,sq2},{0,sq2,sq2}};
sc110nn = 2;
```

Simple Cubic (111) Surface, Coordinate System: x=[1 1 -2], y=[-1 1 0], z=[111]

```
sc111 = {{-h,0,a},{e,sq2,a},{e,-sq2,a}};
sc111nn = 3;
```

FCC (001) Surface, Coordinate System: x=[100], y=[010], z=[001]

```
ff001 = {{0.5,0,0.5},{-0.5,0,0.5},{0,-0.5,0.5},{0,0.5,0.5}};
ff001nn = 4;
```

FCC (11n) Step-Edge, Coordinate System: x=[100], y=[010], z=[001]

```
fst001t = {{0.5,0.5,0}};
fst001tnn = 1;
```

FCC (11n) Step-Corner, Coordinate System: x=[100], y=[010], z=[001]

```
fst001b = {{0.5,0,0.5},{0,0.5,0.5}};
fst001bnn = 2;
```

FCC (110) Surface, Coordinate System: x=[001], y=[1 -1 0], z=[110]

```
ff110 = {{0.5,d,d},{0.5,-d,d},{-0.5,d,d},{-0.5,-d,d},{0,0,sq2}};
ff110nn = 5;
```

FCC (110) Sub-surface, Coordinate System: x=[001], y=[1 -1 0], z=[110]
In an fcc(110) film, atoms in the 2nd layer will also be missing nearest neighbors.

```
fsb110 = {{0,0,sq2}};
fsb110nn = 1;
```

FCC (111) Surface, Coordinate System: x=[1 1 -2], y=[-1 1 0], z=[111]

```
ff111 = {{-f,-d,a},{-f,d,a},{e,0,a}};
ff111nn = 3;
```

BCC (001) Surface, Coordinate System: x=[100], y=[010], z=[001]

```
bf001 = {{0.5,-0.5,0.5},{0.5,0.5,0.5},{-0.5,0.5,0.5},{-0.5,-0.5,0.5}};
bf001nn = 4;
```

BCC (01n) Step-Corner, Coordinate System: x=[100], y=[010], z=[001]

```
bst001b = {{0.5,0.5,0.5},{0.5,-0.5,0.5}};
bst001bnn = 2;
```

BCC (110) Surface, Coordinate System: x=[001], y=[1 -1 0], z=[110]

```
bf110 = {{0.5,0,sq2},{-0.5,0,sq2}};
bf110nn = 2;
```

BCC (111) Surface, Coordinate System: x=[1 1 -2], y=[-1 1 0], z=[111]

```
bf111 = {{-e,-sq2,b},{h,0,b},{-e,sq2,b},{0,0,c}};
bf111nn = 4;
```

BCC (111) Sub-surface, Coordinate System: x=[1 1 -2], y=[-1 1 0], z=[111]
In an bcc(111) film, atoms in the 2nd layer will also be missing nearest neighbors.

```
bsb111 = {{0,0,c}};
bsb111nn = 1;
```

Type in the appropriate labels for ts and tsnn. For example, to calculate $E_{surface}$ for an fcc(001) film, ts = ff001 and tsnn = ff001nn, as shown below.

```
ts = ff001;
tsnn = ff001nn;
```

rt is an array of the nearest-neighbor bond lengths.

```
rt = Table[Sqrt[ts[[i,1]]^2 + ts[[i,2]]^2 + ts[[i,3]]^2], {i, tsnn}];

strains = {{exx,exy,exz},{exy,eyy,eyz},{exz,eyz,ezz}};

dt = Table[strains . ts[[i]], {i,tsnn}];

drt = Table[dt[[i]] . ts[[i]]/rt[[i]], {i,tsnn}];
```

newbonds is an array of the nearest-neighbor bonds after the material is strained by the strain tensor **strains**, *given above.*

```
newbonds = Table[ts[[i]] + dt[[i]], {i,tsnn}];

newrt = Table[Simplify[(rep[newbonds[[i,1]]^2] + rep[newbonds[[i,2]]^2] +
        rep[newbonds[[i,3]]^2])^(1/2)], {i,tsnn}];
```

The gammas below are the angle cosines describing the orientation of the strained bonds with respect to the coordinate axes which were specified above with the nearest-neighbor positions.

```
gamma1 = Table[rep[ExpandDenominator[PowerExpand[newbonds[[i,1]]/
         newr[[i]]]]], {i,tsnn}];
gamma2 = Table[rep[ExpandDenominator[PowerExpand[newbonds[[i,2]]/
         newr[[i]]]]], {i,tsnn}];
gamma3 = Table[rep[ExpandDenominator[PowerExpand[newbonds[[i,3]]/
         newr[[i]]]]], {i,tsnn}];
```

The lines below give the first term in a Taylor series expansion.

```
gamma1 = rep[Chop[Expand[Simplify[Numerator[gamma1]/rt ((-1/2)
         PowerExpand[Denominator[gamma1]^2]/rt^2 + 3/2)]]]];
gamma2 = rep[Chop[Expand[Simplify[Numerator[gamma2]/rt ((-1/2)
         PowerExpand[Denominator[gamma2]^2]/rt^2 + 3/2)]]]];
gamma2 = rep[Chop[Expand[Simplify[Numerator[gamma3]/rt ((-1/2)
         PowerExpand[Denominator[gamma3]^2]/rt^2 + 3/2)]]]];
```

The betas are the cosine of the angles between the magnetization vector and the bonds. a1, a2, and a3 are the angle cosines describing the orientation of the magnetization vector with respect to the coordinate axes x,y,z as specified above.

```
beta = Table[rep[a1 gamma1[[i]] + a2 gamma2[[i]] + a3 gamma3[[i]],
       {i,tsnn}]];
```

The w's are the pair interaction energies between atoms. Note we only calculate the dipole term here.

```
w = Table[rep[(1 + dldr*drt[[i]])(beta[[i]]^2 - 1/3)], {i,tsnn}];
```

The total energy density is a sum of the pair-interactions over all nearest-neighbors. The final result is given in terms of theta and phi (θ and ϕ) as defined in chapter 5.

```
energy = 0.5 Sum[w[[i]], {i,1,tsnn}]//N;

enrgy2 = Simplify[energy] //. rule1;
enrgy3 = Simplify[enrgy2] //. rule2;

total = Chop[rep[Expand[enrgy3]]];

total //. a1 -> Cos[phi]Sin[theta];
% //. a2 -> Sin[phi] Sin[theta];
total = % //. a3 -> Cos[theta]
```

Bibliography

[1] L. Néel. *J. Phys. Rad.*, 15:225, 1954.

[2] U. Gradmann and J. Muller. *Phys. Stat. Sol.*, 27:313, 1968.

[3] A. Berger, U. Linke, and H. P. Oepen. *Phys. Rev. Lett.*, 68:839, 1992.

[4] J. Chen and J. Erskine. *Phys. Rev. Lett.*, 68:1212, 1992.

[5] M. Albrecht, T. Furubayashi, M. Przybyliski, J. Korecki, and U. Gradmann. *J. Magn. Magn. Mater.*, 113:207, 1992.

[6] H. P. Oepen, C. M. Schneider, D. S. Chuang, C. A. Ballentine, and R. C. O'Handley. *J. Appl. Phys.*, 73:6186, 1993.

[7] L. J. Schowalter, E. L. Hall, N. Lewis, and Shin Hashimoto. In J. C. Bravman, W. D. Nix, D. M. Barnett, and D. A. Smith, editors, *Thin Films: Stresses and Mechanical Properties*, volume 130, page 171, Pittsburgh, 1989. Materials Research Society, Materials Research Society.

[8] R. M Bozorth. *Ferromagnetism.* Van Nostrand, Princeton, NJ, 1951.

[9] R. F. Soohoo. *Magnetic Thin Films.* Harper and Row, New York, 1965.

[10] S. Chikazumi. *Physics of Magnetism.* Robert E. Krieger Publishing Co., Inc, Florida, 1986.

[11] J. Goddard and J. G. Wright. *Brit. J. Appl. Phys.*, 16:1251, 1965.

[12] H. B. Callen and E. Callen. *J. Phys. Chem. Sol.*, 27:1271, 1966.

[13] C. Zener. *Phys. Rev.*, 96:1335, 1954.

[14] J. H. Van Vleck. *Phys. Rev.*, 52:1178, 1937.

[15] F. Keffer. *Phys. Rev.*, 100:1692, 1955.

[16] W. J. Carr. *J. Appl. Phys.*, 29:436, 1958.

[17] E. C. Stoner and E. P. Wohlfarth. *Phil. Trans. Roy. Soc. A*, 240:599, 1948.

[18] R. H. Victora and J. M. MacLaren. *Phys. Rev. B*, 47:11583, 1993.

[19] G. B. Bochi, C. A. Ballentine, H. E. Inglefield, S. S. Bogomolov, C. V. Thompson, and R. C. O'Handley. In B. T. Jonker, S. A. Chambers, R. F. C. Farrow, C. Chappert, R. Clarke, W. J. M. de Jonge, T. Egami, P. Grunberg, K. M. Drishnan, E. E. Marinero, C. Rau, and S Tsunashima, editors, *Magnetic Ultrathin Films: Multilayers and Surfaces/Interfaces and Characterization*, volume 313, page 309, Pittsburgh, 1993. Materials Research Society, Materials Research Society.

[20] C. Chappert and P. Bruno. *J. Appl. Phys.*, 64:5736, 1988.

[21] R. C. O'Handley and S. W. Sun. In S. S. P. Parkin, editor, *Magnetic Thin Films, Multilayers and Surfaces*, volume 231, page 485, Pittsburgh, 1991. Materials Research Society, Materials Research Society.

[22] P. Krams, F. Lauks, R. L. Stamps, B. Hillebrands, G. Gunterodt, and H. P. Oepen. *J. Magn. Magn. Mater.*, 121:483, 1993.

[23] C. A. Ballentine, R. L. Fink, J. Araya-Pochet, and J. L. Erskine. *Appl. Phys. A*, 49:459, 1989.

[24] B. Heinrich, K. B. Urguhart, A. S. Arrott, J. F. Cochran, K. Myrtle, and S. T. Purcell. *Phys. Rev. Lett.*, 59:1756, 1987.

[25] N. C. Koon, B. T. Jonker, F. A. Volkening, J. J. Krebs, and G. A. Prinz. *Phys. Rev. Lett.*, 59:2463, 1987.

[26] D. P. Pappas, K.-P. Kamper, B. P. Miller, H. Hopster, D. E. Fowler, A. C. Luntz, C. R. Brundle, and Z.-X. Shen. *J. Appl. Phys.*, 69:5209, 1991.

[27] R. Allenspach and A. Bischof. *Phys. Rev. Lett.*, 69:3385, 1992.

[28] C. Liu, E. R. Moog, and S. D. Bader. *Phys. Rev. Lett.*, 60:2422, 1988.

[29] D. P. Pappas, K.-P. Kamper, and H. Hopster. *Phys. Rev. Lett.*, 64:3179, 1990.

[30] D. S. Wang and A. J. Freeman. *Phys. Rev. B*, 48:15886, 1993.

[31] H. J. G. Draaisma and J. M. de Jonge. *J. Appl. Phys.*, 64:3610, 1988.

[32] Patrick Bruno. *J. Appl. Phys.*, 64:3153, 1988.

[33] D. J. Srolovitz and J. P. Hirth. *Surf. Sci.*, 255:111, 1991.

[34] H. L. Davis, J. B. Hannon, K. B. Ray, and E. W. Plummer. *Phys. Rev. Lett.*, 68:2632, 1992.

[35] F. C. Franck and J. H. vander Merwe. *Proc. R. Soc. London Ser. A*, 198:216, 1949.

[36] J. W. Matthews and J. L. Crawford. *Thin Solid Films*, 5:187, 1970.

[37] J. Chen, M. Drakaki, C. A. Ballentine, and J. L. Erskine. *Bull. Am. Phys. Soc.*, 35:199,

1990.

[38] S.W. Sun and R.C. O'Handley. *Phys. Rev. Lett.*, 66:2798, 1991.

[39] R. Zuberek, H. Szymczak, R. Krishnan, and M. Tessier. *J. de Phys. C*, 49:1761, 1988.

[40] O. S. Song, C. A. Ballentine, and R. C. O'Handley. *Appl. Phys. Lett.*, 64:2593, 1994.

[41] F. J. A. den Broeder, H. C. Donkersloot, H. J. D. Draaisma, and W.J.M de Jonge. *J. Appl. Phys.*, 61:4317, 1987.

[42] S. Hashimoto, Y. Ochiai, and K. Aso. *Appl. Phys. Lett*, 56:1069, 1990.

[43] W. B. Zepper, Gerdanus F. J. A. M., P. F. Carcia, and C. R. Fincher. *J. Appl. Phys.*, 65:4971, 1989.

[44] Z. Q. Qiu, J. Pearson, and S. D. Bader. *Phys. Rev. B*, 45:8195, 1992.

[45] J.J. de Miguel, A. Cebollada, J.M. Gallego, S. Ferrer, R. Miranda, C.M. Schneider, P. Bressler, J. Barbe, K. Bethke, and J. Kirschner. *Surf. Sci.*, 211:732, 1989.

[46] L. Gonzalez, R. Miranda, M. Salmeron, J. A. Verges, and Felix Yndurain. *Pys. Rev. B*, 24:3245, 1981.

[47] A. Clarke, G. Jennings, R. F. Willis, P.J. Rous, and J.B. Pendry. *Surf. Sci.*, 187:327, 1987.

[48] R. Miranda, R. D. Chanders, and J. LeCante. *Surf. Sci.*, 130:269, 1983.

[49] A. K. Schmid and J. Kirschner. *Ultramicroscopy*, 42:483, 1992.

[50] B. Heinrich, J. F. Cochran, M. Kowalewski, and J. Kirschner. *Phys. Rev. B*, 44:9348, 1991.

[51] W. F. Egelhoff. In *Ultrathin Magnetic Structures I*, Berlin, 1994. Springer.

[52] J. A. C. Bland, D. Pescia, and R. F. Willis. *Phys. Rev. Lett.*, 58:1244, 1987.

[53] K. Pescia, M. Stampanoni, G. L. Bona, A. Vaterlaus, R. F. Willis, and F. Meier. *Phys. Rev. Lett.*, 58:933, 1987.

[54] J. J. de Miguel, A. Cebollada, J. M. Gallego, R. Miranda, C. M. Schneider, P. Schuster, and J Kirschner. *J. Magn. Magn. Mater.*, 93:1, 1991.

[55] *Alloy Phase Diagrams*, volume 3 of *ASM Handbook*. ASM International, Ohio, 1992.

[56] E. Navas, P. Schuster, C. M. Schneider, J. Kirschner, A. Cebollada, C. Ocal, R. Miranda, J. Cerda, and P. de Andres. *J. Magn. Magn. Mater.*, 121:65, 1993.

[57] C. M. Schneider, J. J. de Miguel, P. Bressler, P. Schuster, R. Miranda, and J. Kirschner. *J. Electron. Spec.*, 51:263, 1990.

[58] G. Couderchon and J. F. Tiers. *J. Magn. Magn. Mater.*, 26:196, 1982.

[59] I. Hashim and H. A. Atwater, 1994. accepted by J. Appl. Phys.

[60] Chin-An Chang. *Appl. Phys. Lett.*, 58:2444, 1991.

[61] K. Rook, A. M. Zeltser, J. O. Artman, D. E. Laughlin, M. H. Kryder, and R. M. Chrenko. *J. Appl. Phys.*, 69:5670, 1991.

[62] G. A. Somorjai. In *Chemistry in Two Dimesions: Surfaces*, Ithaca, 1981.

[63] J. Frohn, M. Giesen, M. Poensgen, J. F. Wolf, and H. Ibach. *Phys. Rev. Lett.*, 67:3543, 1991.

[64] M. Giesen, J Frohn, M. Poensgen, J. F. Wolf, and H. Ibach. *J. Vac. Sci. Technol. A*, 10:2597, 1992.

[65] M. Giesen-Siebert, R. Jentjens, M. Poensgen, and H. Ibach. *Phys. Rev. Lett.*, 71:3521, 1993.

[66] J. Frohn, M. Giesen, M. Poensgen, J. F. Wolf, and H. Ibach. private communication, 1994.

[67] T. Engel. In *Chemistry and Physics of Solid Surfaces VII*, Berlin-Heidelberg, 1988. Springer.

[68] K.S. Liang, E. B. Sirota, K. L. D'Amico, G. J. Hughes, and S. K. Sinha. *Phys. Rev. Lett.*, 59:2447, 1987.

[69] F. Fabre, D. Gorse, J. Lapujoulade, and B. Salamon. *J. de Phys.*, 48:1017, 1987.

[70] P. Krams, B. Hillebrands, G. Guntherodt, and H. P. Oepen. *Phys. Rev. B*, 49:3633, 1994.

[71] W. Wulfhekel, S. Knappmann, B. Gehring, and H. P. Oepen. accepted by Phys. Rev. Lett., 1994.

[72] C. M. Schneider, P. Bressler, P. Schuster, J. Kirschner, J. J. de Miguel, and R. Miranda. *Phys. Rev. Lett.*, 64:1059, 1990.

[73] P. N. Argyres. *Phys. Rev.*, 97:334, 1955.

[74] H. S. Bennett and E. A. Stern. *Phys. Rev.*, 137:448, 1965.

[75] J. L. Erskine and E. A. Stern. *Phys. Rev. B*, 8:1239, 1973.

[76] P. S. Pershan. *J. Appl. Phys.*, 38:1482, 1967.

[77] H. Fujiwara, H. Kadomatsu, and T. Tokunaga. *J. Magn. Magn. Mater.*, 31:809, 1983.

[78] B. D. Cullity. *Introduction to Magnetic Materials.* Addison-Wesley Publishing Co., Inc., Phillipines, 1972.

[79] W. Oed, H. Lindner, U. Starke, K. Heinz, K. Muller, and J. B. Pendry. *Surf. Sci*,

224:179, 1989.

[80] K. O. Legg, f. Jona, D. W. Jepsen, and P. M. Marcus. *J. Phys. C*, 10:937, 1977.

[81] R. C. O'Handley and J. P. Woods. *Phys. Rev. B*, 42:6568, 1990.

[82] D. S. Chuang, C. A. Ballentine, and R. C. O'Handley. *Phys. Rev. B*, 49:15084, 1994.

[83] U. Gradmann. *J. Magn. Magn. Mater.*, 54:733, 1986.

[84] G. Bochi, O. Song, and R. C. O'Handley. accepted Phys. Rev. B, 1994.

Biographical Note

The author of this thesis, Donna Sue Chuang (née McCoy), was born and raised in Wichita, Kansas. She attended Wichita High School Heights and was graduated first in her class in 1986. She received her Bachelor's of Science in Materials Science and Engineering from the Massachusetts Institute of Technology in February, 1990. Her summer co-op assignments were completed at I.B.M.'s T.J. Watson Research Center. In her junior year, she received the Morris Cohen Award for Outstanding Junior in Materials Science. During her undergraduate years at M.I.T., Donna lived in New House Four. On July 27, 1991, Donna married Thomas Hong Chuang, one of her house-mates from New House.

Donna continued at M.I.T. for her graduate education in the area of Materials Science, supported by a fellowship from the Office of Naval Research. She has been active in the Graduate Materials Committee, serving as Vice-President, M.E.S.S. Chairman, and Representative to the Departmental Committee on Graduate Students. She was a Teaching Assistant for 3.20 Graduate Thermodynamics of Materials and received the Wulff Award for Excellence in Teaching.